

Peripheral Nervous System Alterations in Disease and Injury

A Thesis

Presented to

The Faculty of the Graduate School

At the University of Missouri

In Partial Fulfillment

Of the Requirements for the Degree

Doctor of Philosophy

By

Eric Villalón Landeros

Michael L. Garcia, Thesis Supervisor

DECEMBER 2016

The undersigned, appointed by the dean of the Graduate School,
have examined the thesis entitled

Peripheral Nervous System Alterations in Disease and Injury

Presented by Eric Villalón Landeros,
A candidate for the degree of
Doctor of Philosophy of Biological Sciences,
and hereby certify that, in their opinion, it is worthy of acceptance.

Dr. Michael L. Garcia, Thesis Advisor

Dr. Johannes Schul

Dr. David J. Schulz

Dr. Mark Hannink

Dr. Michael J. Petris

ACKNOWLEDGEMENTS

I would first like to acknowledge and thank my mentor Dr. Michael García. I am grateful for his support and guidance, not only professionally, but also personally. Through his guidance and mentorship I was able to develop into the scientist I am today. I want to thank him for believing in me and for his encouragement throughout my Ph.D. career. I feel privileged to have had the opportunity to work with him and learn from his example. I cannot thank him enough for all the effort he invested into helping me through all my scientific and personal challenges. Thank you very much Dr.G!

I would like to thank my committee members, Dr. David Schulz, Dr. Johannes Schul, Dr. Mark Hannink, and Dr. Mick Petris for their guidance and support. Dr. Hannink for his support through the IMSD and T23 training grants and also for his feedback on my manuscripts. Dr. Schulz for taking the time to discuss and talk about statistics and also for his willingness to read and provide feedback that significantly improved my manuscripts. Dr. Schul for helping me understand the value of animal models for researching human diseases. Dr. Petris for providing me with biochemical perspectives that improved the understanding of my research. Last but not least, I would like to thank Dr. Samuel Waters for allowing me to rotate in his laboratory and work on a project that resulted in a book chapter and also for his words of encouragement during my early Ph.D. career.

I would like to also thank Debbie Allen for her attentive support through the IMSD and T32 training programs and willingness to help me during my impromptu visits to her office. I also want to thank her for being an outstanding event organizer and for the good times and memories during our graduate student recruitment trips to SACNAS

and/or ABRCMS. Life as a graduate student would have been rougher without Debbie's help.

Next, I want to thank the following, current and former, lab members: Maria Jones, Christy Sibigtroth, Patrick Akande, Reginald Edwards, Melanie Vasquez, Paige Pender, and Krista Shucart, Virginia Garcia, Natalie Downer, Jeff Dale, Stephen Shannon, Devin Barry, Victoria Vande Griend, Connie Wong, Amanda Leung, Nathan Byers, Rachel Markey, Dan Landayan, and Hailian Shen. All of you helped me in some way with my research and for that I am grateful. Special thanks to Dr. Dane Lund and Dr. Stephen Shannon, my great friends and colleagues, who provided me with moral support and friendship during our years together as graduate students at Mizzou.

I would like to thank my fiancée and family for the love, support, and patience through these years. To my fiancée Wanda Melissa Figueroa, thank you for your unconditional love and for helping grow and mature personally. I am extremely lucky to have you by my side every step of the way and share our graduate school experiences together. I love you and cannot wait to go on and explore life and science together (with Crispr too), because that is what we do best. To my Mom and Dad for all the support and encouragement and for being my motivation to succeed professionally and personally. To my sisters, future Dr. Norma Villalón, M.D., and future Dr. Rosalina Villalón, Ph.D., for being my role models during all these years in school together and for inspiring me to aim high in my career goals. To my youngest sister, also future Dr. Lupita Villalón, you have given me the motivation to work hard to become a good role model and for being there for me anytime I needed moral support. Without any of you this would not have been possible.

TABLE OF CONTENTS

ACKNOWLEDGEMENTS	ii
LIST OF FIGURES	vi
ABSTRACT	viii
CHAPTER 1 INTRODUCTION AND BACKGROUND	1
1.1 The function of the peripheral nervous system.....	1
1.2 Neurons communicate through electrical signals	2
1.3 Peripheral nervous system myelination	5
1.3.1. Myelin sheath optimization for maximal conduction speed	8
1.3.2. Internodal length is optimized for maximal conduction speed	11
1.4 Efficient nerve conduction velocity depends on axonal diameter	13
1.5 Neurofilament proteins and their role in determining axonal diameter	13
1.6 Neurofilament protein sub-domains	16
1.7 NF-M C-terminus determines axonal diameter	16
1.8 Charcot-Marie-Tooth, a disease of the peripheral nervous system	18
1.9 NF-L mutations cause CMT2E	19
1.10 Cellular neuropathy caused by NF-L mutations in patients1	20
1.11 Human NF-L ^{E396K} neuropathy: A clinically and morphologically heterogeneous disease	22
1.12 CMT2E in mice mimics human disease	23
1.13 CMT neuropathy exacerbation	26
1.14 Peripheral nerve injury: Morphological and functional alterations	27
1.15 Thesis Synopsis	29
CHAPTER 2 MUSCLE SPINDLE ALTERATIONS PRECEDE ONSET OF SENSORIMOTOR DEFICITS IN CHARCOT-MARIE-TOOTH TYPE 2E	32
2.1. Abstract	33
2.2. Introduction	34
2.3. Materials and Methods.....	36
2.4. Results	41
2.5. Discussion	58
CHAPTER 3 EXACERBATION OF CHARCOT-MARIE-TOOTH TYPE 2E NEUROPATHY FOLLOWING TRAUMATIC NERVE INJURY	63
3.1. Abstract	64
3.2. Introduction	65
3.3. Materials and Methods.....	67

3.4. Results	70
3.5. Discussion	87
CHAPTER 4 SCHWANN CELL ELONGATION DURING MYELINATION IS RESTRICTED BY NEUROFILAMENT MEDIUM PHOSPHORYLATION LEADING TO REDUCED INTERNODE LENGTH	90
4.1. Abstract	91
4.2. Introduction	92
4.3. Materials and Methods	95
4.4. Results	105
4.5. Discussion	128
CHAPTER 5 DISCUSSION	131
5.1. Charcot-Marie-Tooth type 2E neuropathy affects proprioceptive sensory systems before affecting sensorimotor systems	133
5.2. Sciatic nerve crush injury results in neuropathy exacerbation in a mouse model of CMT2E	137
5.3. Proposed model of hNF-L ^{E396K} disease pathogenesis	140
5.4. Neurofilament medium C-terminus phosphorylation restricts Schwann cell elongation.	149
5.5. Proposed mechanism of reduced Schwann cell elongation by NF-M phosphorylation	151
5.6. Final conclusions	155
REFERENCES	157
VITA	177

LIST OF FIGURES

Figure 1.1. The make up of a neuron.....	4
Figure 1.2. Peripheral nervous system myelination	7
Figure 1.3. Calculation of g-ratio	10
Figure 1.4. Neurofilament proteins	15
Figure 2.1. Ability to traverse the balance beam was not altered in symptomatic hNF-L ^{E396K} mice	43
Figure 2.2. Motor coordination was reduced in symptomatic hNF-L ^{E396K} mice	46
Figure 2.3. Sensitivity to mechanical stimulation was reduced in hind limbs of symptomatic hNF-L ^{E396K} mice	48
Figure 2.4. Sensitivity to thermal stimulation was not affected in symptomatic hNF-L ^{E396K} mice.....	49
Figure 2.5. Progression from pre-symptomatic to symptomatic resulted in loss of large diameter sensory axons in hNF-L ^{E396K} mice.....	51
Figure 2.6. Muscle spindle number was unaffected in extensor digitorum longus muscles from pre-symptomatic and symptomatic hNF-L ^{E396K} mice.....	53
Figure 2.7. Muscle spindle cross sectional area was reduced in pre-symptomatic and symptomatic hNF-L ^{E396K} mice.....	55
Figure 2.8. Muscle spindle volume was reduced in pre-symptomatic and symptomatic hNF-L ^{E396K} mice	57
Figure 2.9. Auditory Brainstem Responses (ABRs) were unaltered in symptomatic hNF-L ^{E396K} mice	60
Figure 3.1. Functional recovery from sciatic nerve injury was reduced in hNF-L ^{E397K} mice	72
Figure 3.2. Reduced Print Width after nerve crush recovery	75
Figure 3.3. Reduced Print Length on the injured limb after recovery.....	77
Figure 3.4. Max Contact Area is decreased in hind left and diagonal paw after recovery.....	79
Figure 3.5. Reduced Max Intensity in right front and left hind limbs post-injury.....	81

Figure 3.6. Schematic outlining parameters measured by CatWalk	82
Figure 3.7. Reduced Max Contact At (%) in right front and left hind paws following nerve injury recovery	84
Figure 3.8. Limb coordination in hNF-L ^{E397K} mice is altered after recovery from nerve injury.....	86
Figure 4.1. Generation of a constitutively phosphorylated NF-M protein.....	100
Figure 4.2. Ethidium Bromide demyelination results in drastically reduced internode length.....	106
Figure 4.3. Neurofilament phosphorylation levels were maintained during remyelination.....	107
Figure 4.4. Preventing NF-M KSP phosphorylation increased internode length after remyelination	110
Figure 4.5. Expressing NF-M ^{S→E} reduced phosphorylation dependent detection of NF-M in young mice.....	113
Figure 4.6. Motor, but not sensory, nerve conduction velocity was significantly reduced in NF-M ^{S→E} mice	115
Figure 4.7. Expressing NF-M ^{S→E} altered motor axon diameter without affecting survival	117
Figure 4.8. Expressing NF-M ^{S→E} did not affect sensory axons	118
Figure 4.9. Myelin thickness was not affected in NF-M ^{S→E} mice	120
Figure 4.10. Internode length was decreased in L5 motor axons in NF-M ^{S→E/S→E} mice... ..	122
Figure 4.11. Expressing NF-M ^{S→E} altered both phases of Schwann cell elongation... ..	124
Figure 4.12. Motor coordination, but not sensory nerve function was reduced in NF-M ^{S→E/S→E} mice	127
Figure 5.1. Model of hNF-L ^{E396K} disease pathogenesis.....	148
Figure 5.2. Neurofilament medium phosphorylation prevents Schwann cell elongation during myelination.....	153

PERIPHERAL NERVOUS SYSTEM ALTERATIONS IN DISEASE AND INJURY

ERIC VILLALÓN LANDEROS

ABSTRACT

Charcot-Marie-Tooth (CMT) is the most common inherited neuropathy of the PNS affecting approximately 2.8 million people. CMT is generally grouped into demyelinating (type 1), axonal (type2) or intermediate forms (type 3, 4 and X-linked). CMT type 2E, an axonal form of CMT, has been linked to mutations in the neurofilament light gene (*nefl*) and leads to distal neuropathy characterized by reduced nerve conduction velocity, muscle atrophy and sensory loss. However, the mechanisms of disease pathogenesis are not well understood. We generated a mouse model of CMT2E expressing human neurofilament light with the E396K mutation (hNF-L^{E396K}), which develops decreased motor nerve conduction velocity, ataxia, and muscle atrophy by 4 months of age.

My work further characterizes this CMT2E mouse model and shows that symptomatic hNF-L^{E396K} mice developed phenotypes that were consistent with proprioceptive sensory defects as well as reduced sensitivity to mechanical stimulation, while thermal sensitivity and auditory brainstem responses were unaltered. Progression from pre-symptomatic to symptomatic included a 50% loss of large diameter sensory axons within the fifth lumbar dorsal root of hNF-L^{E396K} mice. Due to proprioceptive deficits and loss of large diameter sensory axons, I analyzed muscle spindle morphology

in pre-symptomatic and symptomatic hNF-L^{E396K} and hNF-L control mice. Muscle spindle cross sectional area and volume were reduced in all hNF-L^{E396K} mice analyzed, suggesting that alterations in muscle spindle morphology occurred prior to the onset of typical CMT pathology. These data suggested that CMT2E pathology initiates in the muscle spindles altering the proprioceptive sensory system.

A concern of patients suffering with CMT neuropathy is their increased susceptibility to neuropathy exacerbation after a traumatic event such as undergoing surgery or receiving prescribed drug treatments. Although this problem has been observed with more frequency in recent years, it is not well understood and poorly studied. To investigate if a traumatic event could exacerbate neuropathy in our CMT2E mouse model and possibly establish this as a model to study CMT neuropathy exacerbation, I challenged wild type, hNF-L, and hNF-L^{E396K} mice with crush injury to the sciatic nerve. Then, I analyzed functional recovery by measuring toe spread and analyzed gait using the Catwalk system. hNF-L^{E396K} mice showed reduced recovery from nerve injury consistent with increased susceptibility to neuropathy observed in CMT patients. In addition, hNF-L^{E396K} developed a permanent reduction in their ability to bear weight, increased mechanical allodynia, and premature gait shift in the injured limb, which led to disrupted interlimb coordination in hNF-L^{E396K}. Exacerbation of neuropathy after injury and identification of gait alterations in combination with previously described pathology suggests that hNF-L^{E396K} mice recapitulate many of clinical signs associated with CMT2. The results of my work demonstrate that hNF-L^{E396K} mice provide a model for determining the efficacy of novel therapies.

A complication of peripheral neuropathies or nerve injuries is the loss of myelin. During development, a positive correlation between internodal length and axonal diameter is established so that both are optimized for maximal conduction velocity. However, after recovery from injury this correlation is lost. While axonal diameters recover back normal levels, remyelination results in uniformly short internodes and reduced conduction velocity. Although this phenomenon has been known for over 70 years, the mechanisms leading to abnormally reduced internodal length after remyelination are not well understood. I investigated the potential role of neurofilament phosphorylation in regulating internode length during remyelination and myelination in mice. Following ethidium bromide demyelination in sciatic nerve, the levels of neurofilament medium (NF-M) and heavy (NF-H) phosphorylation were unaffected. Preventing NF-M lysine-serine-proline (KSP) repeat phosphorylation increased internode length by 30% after remyelination. Mimicking constitutive KSP phosphorylation reduced internode length by 16% during myelination and motor nerve conduction velocity by ~27% without altering sensory nerve structure or function. These results suggest that NF-M KSP phosphorylation is a negative regulator of Schwann cell elongation, and suggest that motor and sensory axons utilize different mechanisms to establish internode length. My work on this project provided the first molecular basis for an empirical observation made over 70 years ago, and identified a potential target for therapeutic intervention aimed at enhancing recovery from demyelinating diseases or nerve injuries.

CHAPTER 1

INTRODUCTION AND BACKGROUND

1.1. The function of the peripheral nervous system.

The nervous system is divided into two parts: the central nervous system (CNS) and the peripheral nervous system PNS. The CNS includes the brain and spinal cord while the PNS includes all the nerve projections outside the brain and spinal cord. The PNS is made up sensory and motor neurons, glial cells, and satellite cells. PNS sensory neurons relay information from free nerve endings and receptors located in the skin, muscles, joints and organs to the CNS. In the spinal cord, sensory neuron processes make connections with interneurons that carry the information to the brain, or with motor neuron cell bodies to mediate reflex activity. Motor neurons receive descending input from the brain or directly from PNS sensory neurons and transmit that information to muscles in the periphery (Kandel et al., 2000).

PNS sensory neurons have their cell body located within cell clusters called dorsal root ganglions (DRG), which are located adjacent to the spinal cord. Peripheral sensory neurons are pseudounipolar neurons as their axon splits into two parts; an axonal segment that extends distally to the peripheral organs and another that extends proximally to the spinal cord through the dorsal root. PNS sensory axons are grouped based on size and specific sensory modality. Group I (A-alpha), are large diameter myelinated sensory axons that carry joint position sense information. Group II (A-beta), are intermediate diameter myelinated axons and carry vibration, touch, and joint position sense

information. Group III (A-delta), are small myelinated axons that carry pain and temperature information. Group IV (C-fibers), are small unmyelinated axons ($< 2 \mu\text{m}$) and carry pain, warmth perception, and autonomic sensory information (Casellini and Vinik, 2007).

PNS motor neurons are unipolar type neurons and have their cell body located within the ventral horn of the spinal cord and their axon extends distally through the ventral roots to the peripheral targets. Motor neurons are divided into somatic and autonomic neurons. In this work I will focus on somatic motor neurons, which innervate skeletal muscle and allow for complex movements and behaviors. Motor axons are divided into alpha and gamma motor axons, based on their size. Alpha motor axons are large diameter myelinated axons that innervate force generating extrafusal muscle fibers and control muscle contraction or relaxation (Burke et al., 1977; Kawamura et al., 1977). Gamma motor axons are small diameter myelinated axons that innervate the intrafusal fibers within the muscle spindle and control muscle tone (Hunt and Kuffler, 1951; Kawamura et al., 1977).

1.2. Neurons communicate through electrical signals.

Nerve cells, called neurons, are composed of dendrites, cell body, axon and axon terminal (Fig. 1.1). The dendrites are processes that receive information and bring it to the cell body, where the information is processed and a response is generated. The response to the incoming signals is sent out through the axon, which is a long process some times meters in length, down to the effector cell.

Nerve cells carry information in the form of electrical signals, which are generated by the diffusion of Na^+ and K^+ ions across the axon plasma membrane. Facilitated diffusion of ions across the membrane through ion channels transiently changes the voltage across the membrane and causes a depolarization event (Hodgkin and Huxley, 1945). The depolarization, also called action potential (AP), is propagated along the axon and the rate at which it spreads is called nerve conduction velocity (NCV). Fast NCV is dependent upon the axonal diameter and formation of compact myelin around the axon (Waxman, 1980). Increasing axonal diameter decreases the axial resistance and increases the length that an AP travels before it needs to be propagated (Waxman, 1980). Formation of compact myelin by Schwann cells (in the PNS) creates a layer of insulating membrane around the axon, which dramatically increases the membrane resistance and decreases membrane capacitance preventing the loss of charge across the myelinated area (Huxley and Stampfli, 1949; Koles and Rasminski, 1972; Rasminski and Sears, 1972). Myelination of axons also facilitates the segregation of voltage gated Na^+ channels to discrete areas that become the nodes of Ranvier (Dugandzija-Novakovic et al., 1995; Feinberg et al., 2010; Salzer, 2003; Salzer et al., 2008; Vabnick et al., 1996). The formation of nodes of Ranvier as well as changes to membrane capacitance and resistance, by formation of compact myelin, allows for saltatory conduction, which dramatically increases NCV.

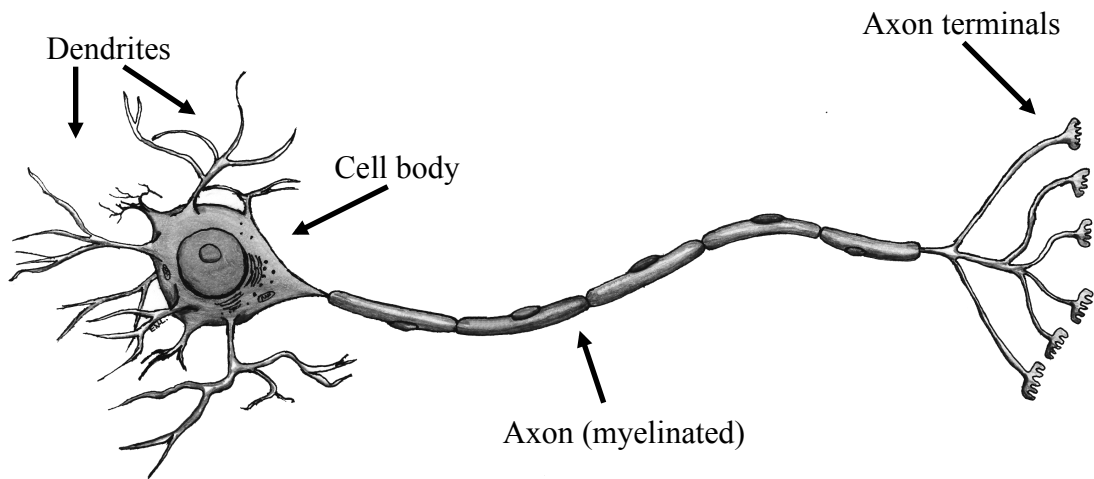


Figure 1.1. The make up of a neuron. A neuron is made up of dendrites, cell body, axon, and axon terminals. The neuron receives input to the cell body through the dendrites. This input is processed at the cell body and a response signal is sent out through the axon. The axon, which can be myelinated (as illustrated above) or unmyelinated, transmits the signals from the cell body to the effector cells through the axon terminals.

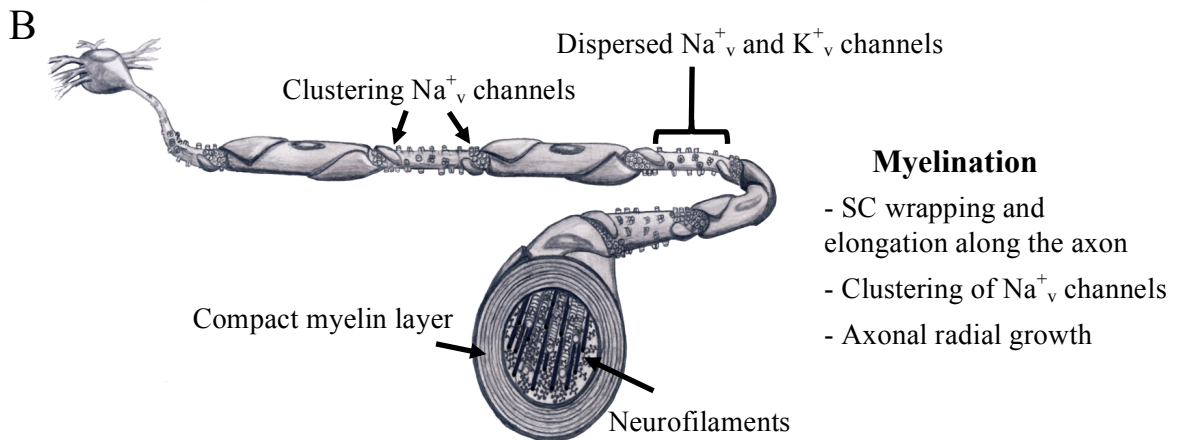
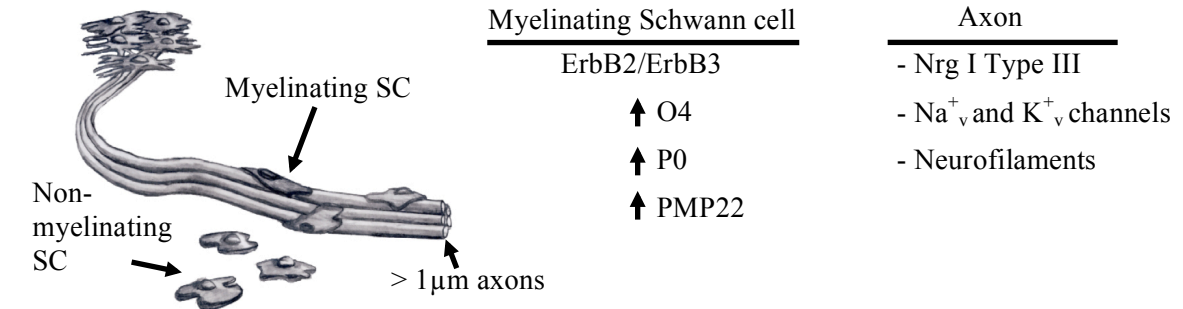
1.3. Peripheral nervous system myelination.

Myelination, by Schwann cells in the PNS, includes both, the formation of compact myelin and the elongation of Schwann cells longitudinally along the axon. During embryonic development, around embryonic day 15/16 in rats (E12/E13 in mice), neural crest cell expression of Sox 10 signals the differentiation of neural crest cells into Schwann cell precursors (Britsch et al., 2001). As development progresses Schwann cell precursors transition into immature Schwann cells and begin to express brain fatty acid-binding protein (BFABP), protein zero (P0), and desert hedgehog (DHH). By embryonic day 18 (16 in mice) Schwann cells associate with motor and sensory axons from spinal nerves in a 1:1 fashion, a process called radial sorting (Dong et al., 1999; Jessen and Mirsky, 2005). Contact with axonal membrane allows interactions between Schwann cell ErbB2/3 receptors and axonal neuregulin 1 type III (Dong et al., 1999; Jessen and Mirsky, 2005) Recent evidence revealed that neuregulin I type III expression on the axon is the signal that induces Schwann cells to myelinate (Taveggia et al., 2005) Preventing neuronal expression of neuregulin 1 type III, prevented myelination in cell culture and in knock out mice (Taveggia et al., 2005). On the other hand, forced expression of neuregulin 1 type III in normally small diameter unmyelinated axons induced them to become myelinated in cell culture and restoring neuregulin 1 type III expression to half the normal levels resulted in an increase in the frequency of myelinated axons in mice (Taveggia et al., 2005). Thus, expression of neuregulin 1 type III above a threshold level induces Schwann cells to acquire a myelinating phenotype and initiate myelination, while expression below threshold levels leads to formation of structures known as Remak bundles (Jessen and Mirsky, 2005; Mirsky et al., 2008; Nave and Salzer, 2006). Schwann

cells in Remak bundles surround the axons with plasma membrane to keep them from touching each other and also provide them with trophic support to prevent axon loss (Chen et al., 2003).

At birth, when the process of myelination begins, Schwann cells begin expressing characteristic proteins like the O4 antigen (a sulfatide), protein zero (P0), and peripheral myelin protein 22 (PMP22) (Dong et al., 1999; Hagedorn et al., 1999; Jessen et al., 1990; Lee et al., 1997; Mirsky et al., 1990) (Fig. 1.2A). As myelination proceeds, Schwann cells distribute themselves along the axons and begin to wrap a layer of plasma membrane around them (Bhat, 2003; Bunge et al., 1989). Repeated spiraling of Schwann cell plasma membrane around the axons leads to the formation of compact myelin. As the Schwann cells spiral around the axon forming the myelin sheath, they also elongate bidirectionally along the axon (Bhat, 2003; Bunge et al., 1989). Elongation of the myelin sheath along the axon induces the clustering of voltage gated sodium channels (Na_v^+ channels), which are initially found dispersed throughout the axon, at the leading edge of the myelin segment into a structure called the heminode (Feinberg et al., 2010; Schafer et al., 2006; Vabnick et al., 1996). Schwann cell elongation continues until adjacent heminodes meet and form the node or Ranvier (Dugandzija-Novakovic et al., 1995; Feinberg et al., 2010; Vabnick et al., 1996) (Fig. 1.2B). By post-natal day 14, the myelinating process is mostly complete and results in mature myelinated axons containing new structural domains like, the myelin sheath, internodes (segments covered by compact myelin), and nodes of Ranvier (segments of Na_v^+ channel clusters devoid of compact myelin) (Fig. 1.2C) (Dugandzija-Novakovic et al., 1995; Feinberg et al., 2010).

A Schwann cell differentiation into myelinating type after axonal contact



C Mature myelinated axon

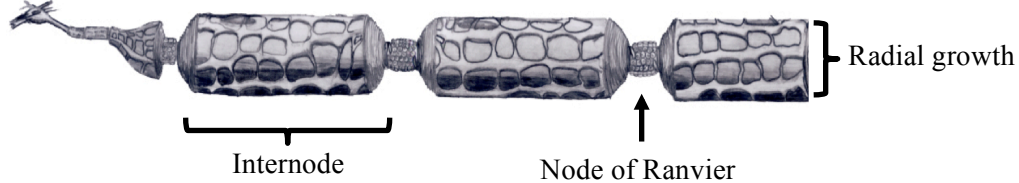


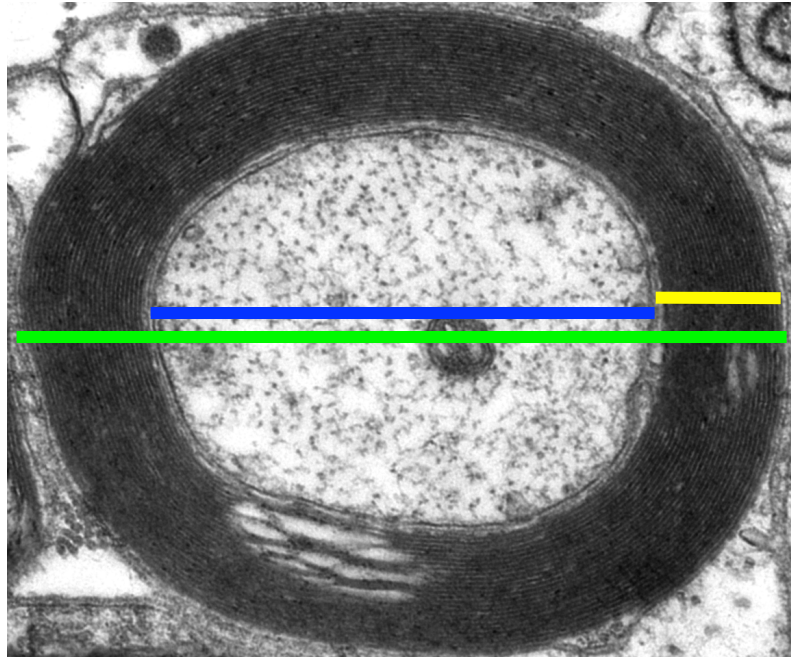
Figure 1.2. Peripheral nervous system myelination. (A) During late embryonic stages Schwann cell (SC) contact with axons greater than 1 μ m in diameter. The interaction of SC ErbB2/3 receptors and axonal neuregulin I type III (Nrg I typeIII) signals SC to differentiate into myelinating type and begin to up regulate expression of O4, P0, and PMP22. In addition, Nrg I type III is expressed on the axonal membrane along with Na⁺_v and K⁺_v ion channels dispersed along the axon. (B) As myelination begins SCs start wrapping and elongating along the axon, which clusters Na⁺_v channels at the front end of the myelin-forming SC and form the node of Ranvier. Formation of compact myelin by SC induces cell biological changes in the axon that cause it to expand in diameter. (C) By postnatal day 14, myelination is complete and the axons acquire nodes of Ranvier, myelin sheath, internodes, and undergo radial growth.

1.3.1. Myelin sheath optimization for maximal conduction speed.

Myelin sheath thickness is a primary determinant of nerve conduction velocity (Waxman, 1980). For over 100 years it has been known that the myelin sheath thickness directly correlates with the axon size (Donaldson and Hoke, 1905). The correlation of myelin sheath thickness and the axonal diameter suggested possible crosstalk between Schwann cells and axons to determine the specific thickness of myelin layer needed for different size axons. Analyses of genetically modified mice that express 50% of neuregulin-1 type III levels revealed that the nerves of these animals developed thinly myelinated axons (Michailov et al., 2004; Taveggia et al., 2005). Moreover, inducing overexpression of neuregulin 1 type III in neuronal tissue resulted in formation of abnormally thicker myelin sheaths. These experiments established that, in addition to inducing Schwann cells to myelinate, axonal neuregulin-1 type III levels determine the thickness of the myelin sheath (Michailov et al., 2004). Thus, myelin sheath thickness depends on the axonal diameter.

One of the main roles of the myelin sheath is to act as an electrical insulator around the axons and allow for faster propagation of action potentials. Compact myelin creates a layer of insulating membrane around the axon, which dramatically increases the membrane resistance thus preventing loss of charges across the axonal membrane in the myelinated region (Huxley and Stampfli, 1949; Koles and Rasminski, 1972; Rasminski and Sears, 1972). Moreover, the compact myelin layer acts as a capacitor decreasing membrane capacitance across the axonal membrane, thus making the myelin layer too thick or too thin affects the electrical conductance of axons (Huxley and Stampfli, 1949;

Koles and Rasminski, 1972; Rasminski and Sears, 1972). Therefore the thickness of the myelin is optimized for optimal electrical conductance (Rushton, 1951; Waxman, 1980). G-ratio is a measure used to analyze the myelination state of an axon (thickness of myelin relative to axon diameter). It is defined by the ratio between the axonal diameter and the fiber diameter (axon + myelin) (Fig. 1.3.) (Rushton, 1951). Making too thin myelin increases g-ratio (closer to 1) and decreases nerve conduction velocity (Barry et al., 2012; Waxman, 1980). On the other hand, increasing myelin thickness decreases g-ratio (closer to 0) and increases conduction velocity (Taveggia et al., 2005; Waxman, 1980). However, increasing myelin thickness past a certain level does not result in further increases in conduction velocity and thus is not energetically favorable to form too thick myelin sheaths (Waxman, 1980). G- ratio, has an optimal range that permits maximal conduction speed and this range is between 0.6 and 0.7 (Waxman, 1980). Therefore, maintaining myelin thickness within the optimal g-ratio range is important for maximizing NCV.



$$g = \frac{\text{Axon diameter}}{\text{Fiber diameter}}$$

Figure 1.3. Calculation of g-ratio. G-ratio is calculated by dividing the axon diameter (blue) by the fiber diameter (green). Fiber diameter (green) is made up of the axon diameter (blue) + 2x myelin thickness (yellow). G-ratio has an optimal range between 0.6 and 0.7 for maximal conduction velocity.

1.3.2. Internodal length is optimized for maximal conduction speed.

As Schwann cells wrap their membrane around the axon, they also elongate bidirectionally along the axon forming compact myelin. Elongating Schwann cells express and secrete gliomedin, which accumulates at the leading edges of the Schwann cell processes (Eshed et al., 2005). Gliomedin binds to the neural cell adhesion molecule (NrCAM) expressed on the microvilli of elongating end of the Schwann cell (Eshed et al., 2007; Eshed et al., 2005). These microvilli expose the NrCAM/gliomedin complex to the axonal membrane, where gliomedin binds to axonal neurofascin 186 (NF186) and clusters it at the leading edge of the SC (Eshed et al., 2007; Eshed et al., 2005; Feinberg et al., 2010). Within the axon, NF186 binds to ankyrin-G, which anchors the Na_v^+ channels and leads to their clustering. Two neighboring Schwann cells continue to elongate until they meet and cluster the Na_v^+ channels in a focal point forming the mature node of Ranvier (Dugandzija-Novakovic et al., 1995; Eshed et al., 2007; Eshed et al., 2005; Feinberg et al., 2010; Vabnick et al., 1996). The segment that each Schwann cell covers is called the internode. During development there are two phases of internode elongation. The first phase occurs during initial myelination from birth until myelination is complete around postnatal day 14 in rodents (Bunge et al., 1989; Jessen and Mirsky, 2005). The second phase occurs during growth of the organism (Jacobs, 1988; Lascelles and Thomas, 1966). Initial observations by Ranvier, almost 145 years ago, suggested that the length of the internode directly correlated with the fiber size as bigger diameter fibers had longer internodes and smaller diameter fibers had shorter internodes (Ranvier, 1872). Moreover, observations that internodal length correlated with the length of the limb in cats, which correlated with conduction speed, led to the hypothesis that internodal length

also correlated with conduction speed (Hursh, 1939). Subsequently, a computational model showed that increasing internodal length increases the speed of conduction and that internode length has an optimal range between 100 and 200 times the diameter of the axon (Brill et al., 1977) That is for a 10 μ m diameter axon the optimal range of internode length is 1000 μ m to 2000 μ m.

In vivo evidence confirming this correlation was provided by the development of a mouse model that develops abnormally short internodes due to the deletion of periaxin. Periaxin is part of the Drp2-dystroglycan complex that is required for the formation of cytoplasmic filled channels, called bands of Cajal, on the abaxonal surface of the myelin sheath (Sherman et al., 2012). Deletion of periaxin leads to disrupted Cajal band formation and reduced ability of Schwann cells to elongate causing formation of abnormally short internodes (Court et al., 2004). The reduction in internodal length significantly reduced nerve conduction velocity with no alterations to myelin thickness or axonal diameter, thus confirming that internodal length is an important determinant of maximal conduction speed (Court et al., 2004). Moreover, it has been further demonstrated *in vivo* that increasing internodal length increases the speed of conduction until a flat maximum is achieved, after which further increases in internodal length do no longer affect the speed of conduction (Simpson et al., 2013; Wu et al., 2012). These experiments taken together provided *in vivo* evidence that internodal length is optimized for maximal speed of conduction. However, the molecular mechanisms that fine tune Schwann cell elongation and lead to the formation of optimal length internodes are not fully understood.

1.4. Efficient nerve conduction velocity depends on axonal diameter.

Axonal diameter is a major determinant of NCV (Rushton, 1951; Waxman, 1980). A method to increase the speed of conduction is to increase the axonal diameter (Waxman, 1980). This is an adaptation that invertebrates, like squid, have taken advantage of. Squid have axons that can be extremely large in diameter, up to 1mm, which can conduct electrical signals up to 50 m/s (Hodes, 1953). For mammals, increasing axonal diameter similar to the squid for increasing the speed of conduction is not an optimal adaptation, as this would make mammalian nervous system excessively large. Therefore, mammals have used a different mechanism to increase the speed of conduction while maintaining axonal diameter relatively small. Myelination in mammalian nerves induces expansion of the axonal diameter, this process is referred to as radial growth (Cleveland, 1996). Expansion of axonal diameter after the formation of compact myelin requires proper expression and localization of neurofilament proteins (Eyer and Peterson, 1994; Sakaguchi et al., 1993; Zhu et al., 1997). Deficits in axonal radial growth can severely compromise nerve function (Kriz et al., 2000; Yamasaki et al., 1991a; Züchner et al., 2004).

1.5. Neurofilament proteins and their role in determining axonal diameter.

Neurofilaments (NFs) are type IV intermediate filament proteins that make up the axonal cytoskeleton (Friede and Samorajski, 1970; Fuchs and Weber, 1994). NFs are composed of three subunits termed neurofilament light (NF-L), neurofilament medium (NF-M), and neurofilament heavy (NF-H) (Lee et al., 1993) (Fig. 1.4). During development expression of NF-L and NF-M was detected as early as embryonic day 9 in

mouse and 12 in rat while expression of NF-H was detected three days later in rats (Carden et al., 1987; Cochard and Paulin, 1984). However, expression of NF-H stayed well below the levels of NF-L and NF-M until about 3 months of age (Pachter and Liem, 1984; Shaw and Weber, 1982). In mature myelinated axons, neurofilaments are obligate heteropolymers made of NF-L and NF-M or NF-H (Lee et al., 1993). Recent data suggest that α -internexin makes up a fourth NF sub-unit in the CNS (Yuan et al., 2006) while peripherin is the fourth NF subunit in the PNS (Yuan et al., 2012). Moreover, the specific neurofilament composition varies according to developmental stages (Shen et al., 2010). Neurofilament abundance within axons has long been correlated with axonal diameter (Friede and Samorajski, 1970). Discovery of the Japanese quail, which lacks axonal neurofilaments due to a nonsense mutation in the NF-L gene, (Ohara et al., 1993; Yamasaki et al., 1991b) and generation of the NF-L knock-out confirmed that neurofilaments are necessary for axonal radial growth as preventing formation of neurofilaments inhibits axonal radial growth (Zhu et al., 1997). Altering the expression of any single neurofilament subunit also reduced radial growth, demonstrating that the specific subunit composition is important for proper axonal radial growth (Xu et al., 1996). Gene replacement experiments revealed that deleting NF-M (Elder et al., 1998a) prevented axonal radial growth similar to deleting NF-L (Zhu et al., 1998). However, deleting NF-H had only minor effects on axonal radial growth (Elder et al., 1998b; Rao et al., 1998; Zhu et al., 1998). These experiments identified NF-M as the critical subunit for axonal radial growth.

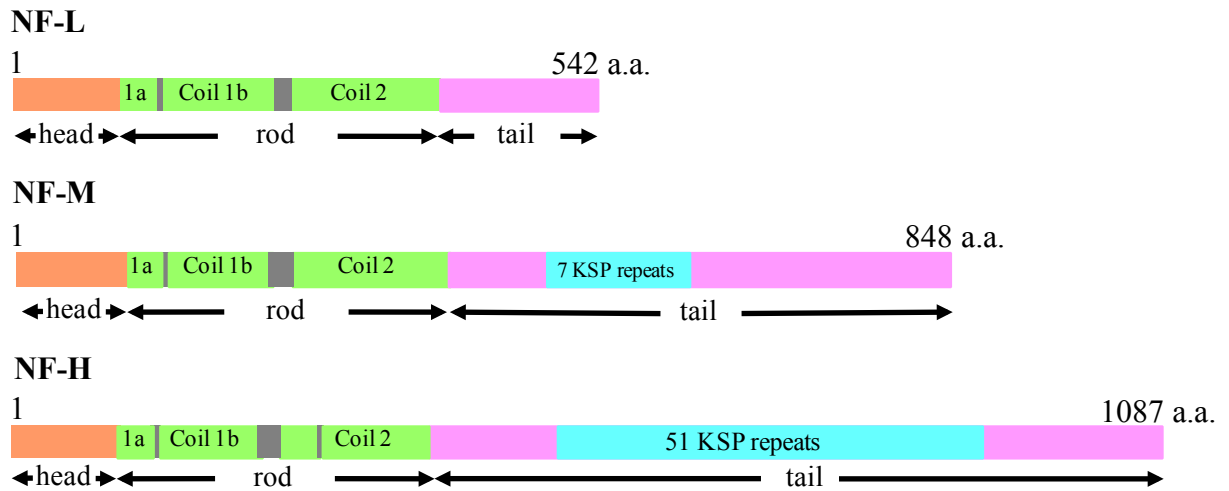


Figure 1.4. Neurofilament proteins. Representation of wild type mouse neurofilament proteins named based on their size; NF-L, NF-M, and NF-H. Domains of each subunit are listed and flanked by arrows under each domain. All three NF subunits contain a head domain (orange), a rod domain (green) and a tail domain (pink). The tail domains of NF-M and NF-H contain regions of lysine-serine-proline (KSP) repeats (cyan).

1.6. Neurofilament protein sub-domains.

All three neurofilament subunits are sub-divided into three domains, each having a different function (Cleveland, 1996; Fuchs and Cleveland, 1998). All NF's have an amino terminus (NH₂-terminus) head domain, a highly conserved ~ 310 α - helical coiled-coil rod domain, and a variable carboxy-terminus (C-terminus) tail domain (Fuchs and Weber, 1994). The head domain is required for neurofilament assembly (Gill et al., 1990) while the rod domain forms for coil-coil interactions between NFs to form the 10nm fiber (Fuchs and Cleveland, 1998; Heins et al., 1993). Moreover, the rod domain contains a hydrophobic heptad sequence (KLLEGEE) that is highly conserved across all IF proteins and it is required for mature filament formation (Gill et al., 1990). The variable tail domains of the three NFs serve have distinct functions. The C-terminus tail domain of NF-L regulates lateral association and ensures proper 10nm fiber formation (Gill et al., 1990). The C-terminus tail domains of NF-M and NF-H are the side arms that protrude perpendicularly from the 10nm filament core (Garcia et al., 2003; Hirokawa et al., 1984; Nakagawa et al., 1995).

1.7. NF-M C-terminus determines axonal diameter.

The C-termini of NF-M and NF-H have a region of lysine-serine-proline (KSP) repeats, which get phosphorylated at the serine residue (Julien and Mushynski, 1982; Julien and Mushynski, 1983) upon formation of compact myelin (de Waegh et al., 1992). Evidence suggested that KSP repeat phosphorylation upon compact myelin formation mediated axonal radial growth (de Waegh et al., 1992; Hsieh et al., 1994; Yin et al., 1998). Gene replacement experiments revealed that removing the NF-M C-terminus tail

domain, along with the seven phosphorylation sites, resulted in reduced axonal radial growth (Garcia et al., 2003; Rao et al., 2003). Surprisingly, deletion of the more heavily phosphorylated NF-H tail domain, containing 51 phosphorylation sites, slowed the axonal radial growth rate, but did not affect overall axonal diameters (Garcia et al., 2003; Rao et al., 2002a). These experiments revealed that the NF-M tail domain is the critical sub-domain for determining axonal diameter and led to the hypothesis that the phosphorylation of NF-M C-terminus KSP served as the signal that determines axonal diameter. However, gene replacement experiments revealed that replacing the NF-M C-terminus KSP serines with alanines to prevent phosphorylation, does not affect axonal radial growth (Garcia et al., 2009).

Sequencing of the *nefm* exon 3, which encodes for the NF-M C-terminus domain, revealed a correlation between the number of KSP repeats and the head-body length in several mammalian species (Barry et al., 2010). Furthermore, axon diameter studies from three species with variable KSP repeat number and head-body length revealed that larger head-body length animals had larger axonal diameters, which also correlated with increased number of KSP repeats (Barry et al., 2010). These results raised the hypothesis that increasing the length of the NF-M C-terminus by increasing the number of KSP repeats could be an evolutionary mechanism to increase conduction velocity by increasing axonal diameter in larger animals. Gene replacement studies in mice confirmed that increasing the length of NF-M C-terminus increased radial growth of large motor axons (Barry et al., 2012). Replacing mouse *nefm* exon 3 (7 KSP repeats) with cow *nefm* exon 3 (22 KSP repeats) increased the length of the NF-M C-terminus (NF-

M^{BovineTail}) and resulted in an increase in axonal diameter of about 1 μm (Barry et al., 2012).

Taken together these results indicate that NF-M C-terminus determines axonal radial growth by varying the number of KSP repeats (and thus its length) and that this happens independently of KSP serine phosphorylation. Thus the role of KSP phosphorylation has become unclear.

1.8. Charcot-Marie-Tooth, a disease of the peripheral nervous system.

Charcot-Marie-Tooth (CMT) is the most commonly inherited disease of the peripheral nervous system (Emery, 1991; Pareyson and Marchesi, 2009; Skre, 1974). According to the CMT association, CMT affects about 2.8 million people worldwide and it is not specific to a certain race or ethnicity. CMT is caused by mutations in genes encoding proteins that form part of the myelin or the axon (Patzko and Shy, 2011; Saporta et al., 2011). Clinical manifestation of CMT is characterized by progressive muscle weakness and atrophy that begins in the distal limbs and slowly progresses proximally (Pareyson and Marchesi, 2009). Patients with CMT typically present with slowed nerve conduction velocities, loss of sensation, foot deformities such as, high arches, outward bending ankles, hammertoes, and clawed digits (Fridman et al., 2015; Pareyson and Marchesi, 2009; Pareyson et al., 2006; Skre, 1974). Along with muscle wasting and muscle weakness in the lower legs, patients also display inability to dorsiflex their feet resulting in foot drop, which causes steppage gait (Pareyson et al., 2006). Although CMT is not typically life threatening, it can be a debilitating disease as it is slowly progressing and last a lifetime. Currently, there is no cure for the disease and the

only treatment available is physical therapy and pain management drugs (Fridman et al., 2015; Patzko and Shy, 2011).

Since its first description by Jean-Martin Charcot, Pierre Marie and Howard Henry Tooth in 1886 (Charcot and Marie, 1886; Tooth, 1886) several different types have been discovered. CMT neuropathies are classified into mainly demyelinating (CMT type 1), axonal (CMT type 2) or mixed intermediate forms (CMT type 3, type 4 and X-linked) (Fridman et al., 2015; Patzko and Shy, 2011). Each type is further sub-divided according to the specific mutated gene. For example, CMT1 is subdivided into CMT1A-F (Bird, 1993a; Bird, 1993b). Despite the specific mutation that causes neuropathy, the clinical manifestations are similar.

1.9. NF-L mutations cause CMT2E.

CMT2 is caused by mutations in genes that encode for proteins essential for the axonal structure and function (Bird, 2016). Currently CMT2 has 22 sub-classifications, CMT2A-V and 2 new sub-types not yet assigned to a classification. CMT type 2 is characterized by uniformly decreased nerve conduction velocities (Bird, 1993b; Bird, 2016). Mutations to the neurofilament light gene (*nefl*) have been linked to MCT type 2E (Barry et al., 2007; Dale and Garcia, 2012). To date, 18 mutations distributed throughout the functional domains NF-L have been linked to CMT 2E (Abe et al., 2009; De Jonghe et al., 2001; Georgiou et al., 2002; Jordanova, 2003; Mersiyanova et al., 2000; Miltenberger-Miltenyi et al., 2007; Yoshihara et al., 2002; Yum et al., 2009). The inheritance pattern of NF-L CMT-linked mutations is usually autosomal dominant with the exception of two recessive mutations (Abe et al., 2009; Yum et al., 2009). To gain

insights into the molecular mechanisms by which NF-L mutations cause CMT, human NF-L E7K, P8R/Q/L, P22S/T, E89K, N97S, and Q333P mutants were expressed in cultured cells (Brownlees et al., 2002; Perez-Olle et al., 2004; Perez-Olle et al., 2002; Perez-Olle et al., 2005). These studies revealed that regardless of the placement of the mutation through the functional domains of NF-L the phenotypic outcome was similar. Mutant human NF-L when co-expressed with normal human NF-L or human NF-M in SW13 Vimentin (+) or SW13 Vimentin (-) failed to assemble into distinct neurofilament networks and rather formed aggregates throughout the cells (Perez-Olle et al., 2004; Perez-Olle et al., 2002; Perez-Olle et al., 2005). Moreover, expression of mutant human NF-L within differentiated catecholaminergic cells that model primary neurons (Qi et al., 1997), or in rat sympathetic or dorsal root ganglion primary cell cultures, recapitulated the formation of NF aggregates and demonstrated altered mitochondria transport and localization (Brownlees et al., 2002; Perez-Olle et al., 2004; Perez-Olle et al., 2005). Formation of neurofilament aggregates is a key hallmark of neurodegenerative diseases and could be the result of altered neurofilament transport or altered neurofilament phosphorylation dynamics. Therefore, these cell culture studies revealed that a common cellular alteration caused by different mutations in the head or rod domain of NF-L was disruption in neurofilament network dynamics.

1.10. Cellular neuropathy caused by NF-L mutations in patients.

Although many mutations in NF-L have been known to cause CMT in humans, the cellular and molecular mechanisms of disease pathogenesis of these mutations is poorly understood. Pathological characterization of patients with NF-L P8L, T21X,

P22R/T, E90K, N98S, E140X, NF-L P22S, E210X, L268P or E396K mutations showed significantly reduced nerve conduction velocity in the median nerve, loss of small and large diameter axons, thinly myelinated axons, and onion bulb formation (Abe et al., 2009; Butinar et al., 2008; Choi et al., 2004; De Jonghe and Jordanova, 1993; Fabrizi et al., 2004; Fabrizi et al., 2007; Georgiou et al., 2002; Jordanova, 2003; Leung et al., 2006; Mersiyanova et al., 2000; Miltenberger-Miltenyi et al., 2007; Shin et al., 2008; Vechio et al., 1996; Yoshihara et al., 2002; Yum et al., 2009; Züchner et al., 2004). Patients with the P22S, L268P showed development of giant axons with NF accumulations and segregated organelles (Fabrizi et al., 2004; Fabrizi et al., 2007; Georgiou et al., 2002) In contrast, patients with the E397K mutation developed thinly myelinated giant axons with absence of NFs in the axoplasm (Fabrizi et al., 2007). The phenotypic manifestations of NF-L mutations included, moderate to severe lower limb muscle weakness, moderate to severe muscle atrophy, foot deformities, gait ataxia, loss of tendon reflexes, decreased sensitivity to touch, and reduced sensitivity to pain (Abe et al., 2009; Butinar et al., 2008; Choi et al., 2004; De Jonghe and Jordanova, 1993; Fabrizi et al., 2004; Fabrizi et al., 2007; Georgiou et al., 2002; Jordanova, 2003; Leung et al., 2006; Mersiyanova et al., 2000; Miltenberger-Miltenyi et al., 2007; Shin et al., 2008; Vechio et al., 1996; Yoshihara et al., 2002; Züchner et al., 2004). Most of these mutations displayed disease onset between the ages of 10 and 20 years (Fabrizi et al., 2007; Georgiou et al., 2002; Shin et al., 2008; Yoshihara et al., 2002), with the exception of the E396K mutation (Berciano et al., 2015; Züchner et al., 2004).

1.11. Human NF-L^{E396K} neuropathy: A clinically and morphologically heterogeneous disease.

Human patients expressing NF-L^{E396K} displayed a variable age of onset ranging from 4 to 46 years of age within one family spanning four generations with the mutation (Berciano et al., 2015; Züchner et al., 2004). In addition to having a variable age of disease onset, patients with the NF-L^{E396K} mutation in multiple members of the same family developed clinical phenotypes that were heterogeneous in severity independent of age (Berciano et al., 2015; Fabrizi et al., 2007; Züchner et al., 2004). In a German family with three generations carrying the NF-L^{E396K} mutation, the earliest reported symptoms were foot deformities (high arches) in an individual at the age of 4 years, which progressed to lower limb muscle weakness and gait ataxia. The sibling of this individual did not develop disease phenotype until the age of 34. Third generation twins, heterozygous for the mutation, had no phenotype at 21 years of age, but their 25-year-old sister presented muscle weakness and gait ataxia. An 82-year-old family member with the mutation did not develop CMT phenotype other than very mild deafness since the age of 46 (Züchner et al., 2004). Morphological analyses from the sural nerves of the more severely affected family members revealed thinly myelinated axons with reduced axonal diameter and onion bulb formation that correlated with reduced nerve conduction velocity (Züchner et al., 2004). Analysis of another unrelated family with the NF-L^{E396K} mutation revealed thinly myelinated axons with significantly enlarged diameters (Fabrizi et al., 2007). The mechanisms by which the NF-L^{E396K} mutation leads to such clinically and morphologically heterogeneous disease phenotype across different families or even between individuals within the same family remain unclear.

1.12. CMT2E in mice mimics human disease.

A limitation of investigating disease mechanisms from human patients, considering that CMT is a motor and sensory neuropathy, is that cellular observations can only be drawn from sensory nerves of living patients. Therefore, the generation of reliable animal models of the disease can help study the disease pathogenesis. To model NF-L head domain mutations a transgenic mouse model expressing the human NF-L P22S (hNF-L^{P22S}) (Dequen et al., 2010) and a knock-in model expressing the P8R mutation in the endogenous NF-L (mNF-L^{P8R}) (Adebola et al., 2015) were generated. Additionally, to model NF-L rod domain mutations a transgenic mouse expressing the human NF-L^{E396K} mutation (hNF-L^{E396K}) (Shen et al., 2011) and a knock-in with the endogenous NF-L harboring the N98S mutation (mNF-L^{N98S}) (Adebola et al., 2015) were generated.

The hNF-L^{P22S} transgene was conditionally expressed using a doxycycline responsive promoter (Dequen et al., 2010). Expression of the transgene in the absence of doxycycline caused mitochondrial transport defects (Dequen et al., 2010) similar to what was observed in cell culture (Perez-Olle et al., 2005) and in human nerve analyses (Fabrizi et al., 2007). However, hNF-L^{P22S} mice failed to recapitulate the NF network alterations (Dequen et al., 2010) seen in cell culture (Perez-Olle et al., 2005) and in human patients (Fabrizi et al., 2007) suggesting that disease pathogenesis in mice might be due to axon transport alterations rather than alterations to the NF network (Dequen et al., 2010). Moreover, hNF-L^{P22S} mice developed muscle hypertrophy accompanied with muscle denervation without axonal loss, which were reversed after suppression of

transgene expression by administration of doxycycline (Dequen et al., 2010). No axon morphological alterations were found in the sciatic nerves hNF-L^{P22S} mice with or without repression of transgene expression (Dequen et al., 2010).

In hNF-L^{E396K} mice constitutive hemizygous expression of the transgene led to disease pathology similar to human patients, which mirrored the autosomal dominance of the mutation as seen in humans. Expressing the hNF-L^{E396K} mice resulted NF network alterations and development of motor axons with reduced axonal diameters and thin myelin (Shen et al., 2011) similarly to alterations observed in human patients (Züchner et al., 2004). Moreover, hNF-L^{E396K} developed muscle atrophy without denervation or axonal loss, instead of muscle hypertrophy and denervation as in the hNF-L^{P22S} model (Dequen et al., 2010).

Expressing the head domain P8R mutation in the endogenous NF-L gene of mice led to a slight reduction of NF-L protein expression in the brain and spinal cord of heterozygous mice (Adebola et al., 2015). Reductions in NF-L protein expression levels were more pronounced and in the homozygote NF-L^{P8R} mice demonstrating to the dominant effect of the mutation (Adebola et al., 2015). Expressing NF-L^{P8R} did not result in any other cellular or molecular phenotype in mice (Adebola et al., 2015).

Introducing the rod domain mutation, N98S, in the mouse NF-L gene resulted in reduced NF-L protein expression levels as well as NF network alterations and NF aggregate inclusions in the neuronal cell bodies (Adebola et al., 2015), similar to results observed in cell culture experiments (Perez-Olle et al., 2004). mNF-L^{N98S} heterozygous mice developed axons with reduced diameter and thin myelin (Adebola et al., 2015), similar to the hNF-L^{E396K} model (Shen et al., 2011) and human patients (Abe et al., 2009;

Jordanova, 2003). However, no muscle morphology or muscle innervation defects have been reported in this mouse model.

These data suggest that mutations located within the NF-L rod domain might lead to disease pathogenesis by a similar mechanism as the hNF-L^{E396K} and mNF-L^{N98S/+} mice developed very similar cellular alterations that include NF network alterations, reduced axonal diameter, and reduced myelin thickness (Adebola et al., 2015; Shen et al., 2011). In contrast, mutations in the head NF-L head domain might use different mechanisms as the hNF-L^{P22S} mice showed no alterations to NF network or axon morphology, but developed axonal transport defects with muscle hypertrophy and denervation (Dequen et al., 2010). Furthermore, mutations in different locations within the head domain might also function through different mechanisms as the mNF-L^{P8R/+} mice only showed slight decreases in NF expression levels with no cellular morphological alterations (Adebola et al., 2015). Therefore, mechanisms of disease pathogenesis might vary according to the location of the mutations along the NF-L functional domains.

Despite the specific mutation, all three phenotypic models displayed similar functional defects. hNF-L^{P22S}, hNF-L^{E396K} and mNF-L^{N98S} all displayed aberrant hind limb postures when lifted by the tail (Adebola et al., 2015; Dequen et al., 2010; Shen et al., 2011). Unfortunately, no further data is available on the functional and behavioral characterization of the mNF-L^{P8R/+} or mNF-L^{N98S/+} mice. However, both hNF-L^{P22S} and hNF-L^{E396K} mice showed signs of hind limb weakness, gait ataxia, and sensorimotor defects (Dale et al., 2012; Filali et al., 2011; Shen et al., 2011). These mouse models ultimately developed behavioral phenotypic alterations similar to human patients

regardless of the mutation modeled, supporting the previous observations that different types or even sub-types of CMT lead to similar functional and behavioral phenotypes.

1.13. CMT neuropathy exacerbation.

Although, the clinical presentation of CMT in patients varies and some patients carrying the mutation might develop very mild to no symptoms, evidence suggests that administration of non-toxic prescribed medications (Chaudhry et al., 2003; Martino et al., 2005; Weimer and Podwall, 2006) or experiencing a traumatic event can lead to neuropathy exacerbation (Gentile et al., 2013). Patients with history of CMT that required treatment for a secondary condition and were administered medications, such as vincristine, cisplatin, and Adriamycin, developed moderate to severe CMT symptoms one to two weeks following treatment (Hildebrand et al., 2000; Weimer and Podwall, 2006). Exacerbation of CMT neuropathy in patients resulted in severely affected ability to walk, write, or sense temperature or touch (Weimer and Podwall, 2006). In the case of neuropathy exacerbation due to administration of prescribed drugs, the typical intervention is to discontinue drug administration, which leads to poor or incomplete recovery (Hildebrand et al., 2000; Weimer and Podwall, 2006). On a separate case, a patient carrying the NF-L^{E396K} mutation presented very mild CMT phenotype since early age experienced severe worsening of neuropathy after her 5th week of pregnancy (Gentile et al., 2013). By the 14th week of pregnancy the patient developed severe lower limb weakness and muscle wasting that caused foot deformities, loss of pinprick sensation, loss of vibration sense, and joint position sense (Gentile et al., 2013). Clinical examination of nerve function revealed that this patient also developed severe reductions

in nerve conduction velocity in lower limb nerves (Gentile et al., 2013). Unfortunately, the mechanisms leading to poor or incomplete recovery after nerve injury in patients suffering with neuropathy are poorly understood and understudied. Thus, no treatments are available to prevent or reverse neuropathy worsening following exacerbation of disease in human patients.

1.14. Peripheral nerve injury: Morphological and functional alterations.

Proper nerve function depends on axonal diameter, optimal myelin thickness, and optimal internodal length (Brill et al., 1977; Waxman and Brill, 1978). Peripheral nerve injury is a common trauma that results in loss of myelin, or loss of axon and myelin. Nerve injuries that result in separation of nerve fibers from the cell body are followed by a process called Wallerian degeneration (Waller, 1850). During Wallerian degeneration the axon that has been separated from its cell body degenerates and is followed by Schwann cell jettison of myelin, which subsequently gets degraded by macrophages and Schwann cells (Fernandez-Valle et al., 1995; Perry et al., 1995; Reichert et al., 1994). The axon stump proximal from the injury site degenerates (“dies back”) typically up to the first node of Ranvier from the site of injury (Cajal, 1928) and then begins to re-sprout and regenerate to re-innervate their targets (Fu and Gordon, 1997). The new Schwann cells, which have dedifferentiated and proliferated, remyelinate the growing nerve (Fu and Gordon, 1997; Sta et al., 2014). Similarly, nerve injuries that cause selective loss of myelin, due to toxicity or disease, lead to nerve demyelination without axon degeneration (Prineas and Connell, 1979; Smith et al., 2013; Woodruff and Franklin, 1999). Eventually, the demyelinated axons become remyelinated (Prineas and Connell, 1979;

Smith et al., 2013; Woodruff and Franklin, 1999). Following remyelination axonal diameters increase back to their pre-injury measurements by about 10 weeks after injury (Devor and Govrin-Lippmann, 1979; Hoffman et al., 1984). Similarly, the thickness of the myelin sheath recovers to its pre-injury values after about 12 weeks post-injury (Fricker et al., 2013). However, internodal lengths remain significantly reduced and lead to compromised nerve function (Sanders and Whitteridge, 1946; Vizoso and Young, 1948).

Damage to the peripheral nervous system, by disease or injury, results in alterations to nerve fiber structures that cause nerve function impairments. Diseases like CMT can cause nerve injury that leads to demyelination and/or axonal alterations resulting in reduced nerve conduction velocity (Brill et al., 1998; Fridman et al., 2015; Pareyson et al., 2006; Yagihashi et al., 2007). Clinically, this dramatic reduction in internodal length has been observed to result in compromised nerve function in patients suffering with CMT (Saporta et al., 2009).

Moreover, reduced internodal length due to demyelination/ remyelination has been observed be part of the pathology in other conditions like, Multiple Sclerosis (Prineas and Connell, 1979), chronic nerve compression (Gupta et al., 2012; Weiss and Hiscoe, 1948), and nerve crush injuries (Hildebrand et al., 1987; Vizoso and Young, 1948; W. and Friede, 1985). Presently, it is not understood how optimal internodal length is established during development or how this program is altered during remyelination after nerve injury. Understanding the mechanisms involved in establishing internodal length will provide with key knowledge that might aid in the development of treatments that restore normal nerve function.

1.15. Thesis synopsis.

Animal survival depends on a fast and efficient functioning nervous system. During development the efficiency of the nervous system is established by the fine-tuning of axonal caliber, myelin thickness, and internodal length to maximize the speed at which nerves communicate. However, during development of diseases, like Charcot-Marie-Tooth or during nerve injury, alterations in nerve structures affect the ability of nerves to communicate fast and efficiently.

Charcot-Marie-Tooth is the most common inherited disease of the peripheral nervous system, which causes alterations to nerve structure that result in nerve dysfunction. Despite being caused by alterations in proteins expressed specifically within in the myelin (CMT1), the axon (CMT2), or a combination of both (CMT3, 4 and x-linked), the resulting phenotypic defects are similar (Fridman et al., 2015). Typical CMT phenotype results in motor and sensory nerve alterations, as well as muscle atrophy and gait defects. We generated a transgenic mouse expressing the human NF-L protein with the E396K mutation, which recapitulate the motor, muscle, and gait alterations observed in the human patients. However, it is unclear if this model also develops sensory alterations similar to human patients. Establishing this mouse model as a true and reliable model of the human disease is necessary for the development of potential therapeutic treatments and development of diagnostic strategies for early disease intervention.

CMT can be a heterogeneous disease with variable age onset and variable symptom severity (Fridman et al., 2015). In some cases, patients with familial history of CMT develop mild to no symptoms of CMT (Züchner et al., 2004). Moreover, clinical

evidence suggests that patients with CMT can develop disease exacerbation after experiencing a traumatic event or after receiving treatment with prescribed drugs. To date, the alterations resulting in neuropathy exacerbation in CMT patients are poorly understood. Understanding mechanisms of disease pathogenesis during exacerbation of neuropathy could also provide new insights into the mechanisms of disease progression during normal development.

Finally, a characteristic hallmark of CMT pathology is the formation of onion bulb structures within a nerve. Onion bulb structures are caused by loss of the myelin sheath, which directly affects nerve function. Although loss of myelin is followed by remyelination recovery, nerve function does not recover back to normal. The lack of normal function recovery is attributed to formation of abnormally short internodes after remyelination. This is phenomenon, is similar across many diseases and nerve injuries that cause nerve demyelination. Although, formation of short internodes after remyelination has been known for almost 70 years, the mechanisms that regulate Schwann cell elongation and establish internodal length are not well understood.

The purpose of my work is to investigate the effects of CMT2E neuropathy on the peripheral sensory nervous system utilizing our hNF-L^{E396K} mouse model. To do this, I performed behavioral analyses focused on testing the function of specific sensory modalities in mice and investigated sensory nerve morphological alterations that could explain the behavioral alterations. Given that patients suffering from CMT can develop exacerbation of neuropathy, I investigated if our CMT2E mouse model also model disease exacerbation by performing a sciatic nerve crush and analyzing functional and gait alterations after recovery. Finally, nerve recovery following a demyelination event,

during disease or injury, leads to the formation of abnormally short internodes that affect nerve function. Given that after nerve recovery internodal length never reaches normal lengths, I investigated possible mechanisms that regulate Schwann cell elongation during myelination by utilizing genetically modified mice.

CHAPTER 2

MUSCLE SPINDLE ALTERATIONS PRECEDE ONSET OF SENSORIMOTOR DEFICITS IN CHARCOT-MARIE-TOOTH TYPE 2E

(This work was submitted for publication to Genes, Brain and Behavior and is under
review)

Eric Villalón^{1,2}, Maria R. Jones^{1,2}, Christine Sibigroth³, Sammy J. Zino^{1,2}, Jeffrey M.
Dale^{1,2}, Dan S. Landayan⁴, Hailian Shen⁵, DDW Cornelison^{1,2}, and Michael L. Garcia^{1,2†}

¹Division of Biological Sciences, ²Bond Life Sciences Center, University of Missouri-
Columbia. Columbia, MO 65211

³Department of Veterinary Medicine and Surgery, College of Veterinary Medicine,
University of Missouri-Columbia, Columbia, MO 65211

⁴Quantitative and Systems Biology, University of California Merced, Merced, CA 95343

⁵Institute of Neuroscience, Shanghai Institutes for Biological Sciences, Chinese Academy
of Sciences, Shanghai 200031 China

Keywords: Proprioception, Muscle Spindle, Sensory, Charcot-Marie-Tooth,
Neurofilament, Peripheral Neuropathy

2.1. Abstract.

Charcot-Marie-Tooth (CMT) is the most common inherited peripheral neuropathy, affecting approximately 2.8 million people. CMT leads to distal neuropathy that is characterized by reduced motor nerve conduction velocity, ataxia, muscle atrophy and sensory loss. We generated a mouse model of CMT2E expressing hNF-L^{E396K}, which develops decreased motor nerve conduction velocity, ataxia, and muscle atrophy by 4 months of age. Symptomatic hNF-L^{E396K} mice developed phenotypes that were consistent with proprioceptive sensory defects as well as reduced sensitivity to mechanical stimulation, while thermal sensitivity and auditory brainstem responses were unaltered. Progression from pre-symptomatic to symptomatic included a 50% loss of large diameter sensory axons within the fifth lumbar dorsal root of hNF-L^{E396K} mice. Due to proprioceptive deficits and loss of large diameter sensory axons, we analyzed muscle spindle morphology in pre-symptomatic and symptomatic hNF-L^{E396K} and hNF-L control mice. Muscle spindle cross sectional area and volume were reduced in all hNF-L^{E396K} mice analyzed, suggesting that alterations in muscle spindle morphology occurred prior to the onset of typical CMT pathology. These data suggested that CMT2E pathology initiated in the muscle spindles altering the proprioceptive sensory system. Early sensory pathology in CMT2E could provide a unifying hypothesis for the convergence of pathology observed in CMT.

2.2. Introduction.

Charcot-Marie-Tooth (CMT) neuropathies are broadly grouped into demyelinating (CMT type 1), axonal (CMT type 2), or intermediate forms (CMT type 3, type 4 and X-linked) (Fridman et al., 2015). While the specific mutations causing CMT vary, the clinical presentation is very similar between the major types. CMT clinical signs include foot deformities accompanied by progressive muscle weakness and muscle atrophy as well as loss of sensation and altered joint positioning sense (Pareyson et al., 2006). With more than 60 different genes associated with the various types of CMT (Bouhy and Timmerman, 2013), it is unclear how the clinical presentation is similar across CMT types.

CMT patients show signs of sensory dysfunction including loss of vibration and joint position sense progressing to decreased pain and temperature sensation (Szigeti and Lupski, 2009). Vibration and joint position sense are transmitted to the central nervous system by large myelinated axons, which are designated group II and group Ia/b sensory fibers, respectively (Gilman, 2002). In the periphery, receptors that detect vibration sense include Merkel disk receptors, Meissner's corpuscles and pacinian corpuscles, which can also mediate tactile sensation (Gilman, 2002). Joint position sense is sensed by muscle spindles and Golgi tendon organs (Gilman, 2002). Thus, sensory dysfunction could result from pathology within large myelinated axons, peripheral end organs or both. Alterations in sensory nerves preceding the manifestation of sensorimotor dysfunction are commonly observed in rodent CMT models (Achilli et al., 2009; d'Ydewalle et al., 2011; Gillespie et al., 2000; Lee et al., 2013; Sereda et al., 1996). Thus, selective loss of large myelinated sensory fibers could be a common site of initial pathogenesis resulting in convergence of

clinical phenotypes observed in CMT patients despite the cellular and genetic variability associated with individual CMT types.

CMT type 2E is an axonal form of CMT that was linked to mutations in the neurofilament light gene (*nefl*) (Mersiyanova et al., 2000). Currently, there are 18 mutations located in all domains of NF-L protein linked to CMT type 2E. Patients expressing the glutamate to lysine at amino acid 396 (E396K) mutation presented with typical CMT signs, such as foot deformities, muscle weakness and atrophy, gait ataxia and altered sensation (Züchner et al., 2004). Moreover, analysis of sural nerve biopsies from patients with the E396K mutation revealed reduced axonal diameters with thinner myelin and loss of sensory axons (Züchner et al., 2004). To study the mechanisms of disease pathogenesis, four CMT2E mouse models were generated, expressing human NF-L^{P22S} (Dequen et al., 2010), mouse NF-L^{N98S}, mouse NF-L^{P8R} (Adebola et al., 2015), and human NF-L^{E397K} (Shen et al., 2011) (referred to hereafter as hNF-L^{E396K}). Transgenic mice expressing hNF-L^{P22S} developed aberrant hind limb posture, gait ataxia and sensorimotor defects (Dequen et al., 2010; Filali et al., 2011). Cellular analyses of hNF-L^{P22S} mice revealed muscle hypertrophy and denervation without motor or sensory axonal loss (Dequen et al., 2010). Mice expressing mNF-L^{N98S} developed aberrant hind limb posture and tremors when lifted by the tail (Adebola et al., 2015). Additionally, mNF-L^{N98S} expression resulted in neurofilament inclusions in motor and sensory cell bodies and reduced axonal diameters (Adebola et al., 2015). mNF-L^{P8R} mice did not develop a phenotype (Adebola et al., 2015). We generated a transgenic mouse model expressing hNF-L^{E396K} (Shen et al., 2011). hNF-L^{E396K} mice developed aberrant hind limb posture, foot deformities (Shen et al., 2011) and altered gait (Dale et al., 2012). Cellular pathology

included distal limb muscle atrophy without denervation and reduced motor axon diameters as well as reduced myelin thickness (Shen et al., 2011).

In this study, we analyzed sensory systems to determine if hNF-L^{E396K} mice developed sensory deficits. Similar to CMT2E patients, symptomatic hNF-L^{E396K} mice developed sensory dysfunction consistent with loss of joint position sense and reduced sensitivity to mechanical stimulation. Sensory axons that relay joint position and vibration sense to the central nervous system are large myelinated group I and group II axons (Casellini and Vinik, 2007; Tourtellotte and Milbrandt, 1998). Therefore, we quantified sensory axons in pre-symptomatic and symptomatic hNF-L^{E396K} mice. Symptomatic hNF-L^{E396K} mice had reduced numbers of large (>5 μ m) sensory axons. Sensory axon loss together with alterations in joint position sense suggested possible alterations to the proprioceptive sensory system. Consistent with this hypothesis, cross sectional area and volume of muscle spindles were reduced in pre-symptomatic and symptomatic hNF-L^{E396K} mice. Our results suggested that hNF-L^{E396K} mice developed early alterations in sensory systems that precede the onset of motor system pathology (Shen et al., 2011).

2.3. Materials and Methods.

Animals. hNF-L and hNF-L^{E396K} transgenic mice were generated as separate lines on a C57BL/6J background as previously described (Shen et al., 2011). All procedures were in compliance with the University of Missouri Animal Care and Use Committee and with all local and federal laws governing the humane treatment of animals. Equal number of male and female mice was used for all experiments. All experiments were performed

during the light phase (7:00 am - 7:00pm) of the light cycle. Previous analyses of hNF-L^{E396K} mice indicated that overt disease phenotype such as, aberrant hind limb posture, foot deformities, and gait alterations initiate at 4-months of age (Dale et al., 2012; Shen et al., 2011). Thus, for this study, 2-month \pm 1 week-old mice were considered pre-symptomatic and 6-month \pm 1 week-old mice were used considered symptomatic. Mice were housed in microisolator cages (up to 5 per cage) on a 12-h light/dark cycle, and were given food and water *ad libitum*.

Tissue Preparation and Axon Morphological Analysis.

2 and 6-month-old mice were perfused intracardially with 4% paraformaldehyde in 0.1 M Sorenson's phosphate buffer, pH 7.2, and postfixed overnight in the same buffer. Fifth lumbar nerve roots were dissected, treated with 2% osmium tetroxide, washed, dehydrated, and embedded in Epon-Araldite resin. Thick sections (0.75 μ m) for light microscopy were stained with ρ -phenylenediamine. Cross sections of 5th lumbar sensory axons were analyzed in at least three mice per group. Axonal diameters were measured using the AxioVision Software (Zeiss International). Entire roots were imaged, imaging thresholds were selected individually, and the cross-sectional area of each axon was calculated and reported as a diameter of a circle of equivalent area. Axons were grouped into $>5\mu$ m or $<5\mu$ m bins, and were analyzed for statistical significance.

Balance beam.

Previous analyses of hNF-L^{E396K} mice indicated that overt disease phenotype such as, aberrant hind limb posture, foot deformities, and gait alterations initiate at 4-months of

age (Dale et al., 2012; Shen et al., 2011). Thus we analyzed motor coordination defects on symptomatic, 6-month-old hNF-L^{E396K} and hNF-L control mice. 6-month-old mice were trained for 5 days to walk on three progressively smaller circular wooden beams (5, 2.5 and 1cm diameter) 120 cm in length, suspended 50 cm from a bedding surface. During training, mice walked on each of the three beams for 3 minutes with at least 20 minutes of rest. After training, experiments were performed on the smallest beam, with markings in 5cm increments along the beam. Escape from beam was obstructed at each end. A digital camera was placed both perpendicular and parallel to the beam allowing for delineation of walking speed and foot slips, respectively. Mice were tested in three trials per day for three consecutive days (day 1, day 2, day 3) with at least 20 minutes of rest between trials. The number of falls, number of foot slips, total time walking, and the latency to fall within the 3-minute trials were scored for each day tested. The number of foot slips and falls were counted and normalized to amount of time walking per genotype per day tested. In addition, the average voluntary walking distance was measured using the 5cm intersection marks, and was used to calculate the average walking speed per genotype on the last day tested.

Thermal nociception.

Response to thermal nociception was analyzed by Hargreaves assay (Hargreaves et al., 1988) utilizing a Paw Thermal Stimulator System (Department of Anesthesiology, University of California, San Diego). 6-month-old mice were placed under wire cages on a glass surface that was maintained at 30°C. Latencies of limb withdrawal from a focused source of light were measured. Latencies of withdrawal were converted to temperatures

by the construction of a standard curve using an attached thermocoupler under the glass surface. Averages were analyzed for statistical significance by Student's *t*-test.

Mechanical nociception.

Threshold response to mechanical allgesia was measured with a Dynamic Plantar Aesthesiometer (DPA) model # 37450 (Ugo Basile, Italy) in 6-month-old mice. Mice were set on a wire-mesh platform and allowed to habituate for at least 15 min. After habituation, the DPA monitored paw withdrawal thresholds. A metal filament was pushed against the hind and front paws with an ascending linear force (10 g/s and 2 g/s, respectively) until a strong, immediate withdrawal occurred. Measurements were taken in triplicate and averages were reported as paw withdrawal thresholds in grams. Averages were analyzed for statistical significance by Student's *t*-test.

Auditory brainstem response (ABR).

ABRs were performed with a Cadwell Sierra Wave electrodiagnostic unit running version 8.0 software (Cadwell Industries, Inc., Kennewick, WA). 6-month-old mice were sedated with an intraperitoneal injection of tribromoethanol (4mg/10g). Once adequate sedation was achieved, as determined by response to painful stimulus such as toe pinch, subdermal platinum wire recording electrodes were placed. The reference electrode was inserted at the vertex (-), the active electrode ventrolateral to the stimulated ear (+) and the ground electrode in the midneck region. Alternating condensation/rarefaction click stimuli of 80 decibels sound pressure level (dB SPL) were delivered through tubal earphones at the rate of 11.3 stimuli/s. Masking noise of 50 dB SPL was applied to the contralateral ear. 500 responses

were recorded with a band-pass filter hi-cut of 3 kHz and low-cut of 100 Hz and then averaged. Both left and right ears were stimulated and recorded from. The latency from the peak of waveform I-II and I-IV (mS) were measured. After the procedure was complete, mice were humanely euthanized with an overdose of tribromoethanol followed by cervical dislocation.

Immunohistochemistry.

Muscle spindle analysis was performed on the Extensor Digitorum Longus (EDL) muscle in 2 and 6-month-old mice. Fresh EDL muscles were isolated and quickly flash frozen in liquid nitrogen-cooled isopentane. Unfixed 16 μ m transverse serial sections were made through the entire length of each muscle, and every 12th section was collected and stored at -20°C until further processing. Fresh unfixed sections were blocked in Hen serum for 1 hour at 4°C and then in in blocking solution (10% normal goat serum, 1% NP-40) for another hour at 4°C.

Mouse monoclonal antibody against myosin heavy chain I (BA-D5-S, Developmental Studies Hybridoma Bank, University of Iowa, USA) in blocking solution (1:50) was applied to the sections and incubated overnight at 4°C. The sections were then washed 3x for 5 min with PBS, fixed with 4% PFA for 10 min at 4°C and washed again 3x for 5 min with PBS at room temperature. Sections were incubated in a chicken polyclonal antibody against neurofilament medium (CPCA-NF-M) in blocking solution (1:2000) at 4°C overnight to label axons followed by PBS washes 3x for 5 min at room temp. Subsequently, sections were washed for 5 min 3x with PBS, incubated with species-specific secondary antibodies that were conjugated with either Alexa Fluor 488 or 555 (Molecular Probes, Invitrogen) (1:500) diluted in blocking buffer, and washed again for 5min 3x with PBS. Slides were mounted in

Vectashield with DAPI (Vector Labs, Burlingame, CA, USA), and imaged on a confocal microscope (Leica Microsystems, Inc, Model TPS SPE, Buffalo Grove, IL 60089).

Muscle Spindle Analysis.

Individual muscle spindles were identified and traced through sequential serial sections. The area of each muscle spindle was measured in each serial section, and maximum, median, and minimum cross sectional areas were determined for each spindle. The approximate length of each muscle spindle was calculated by multiplying section thickness (16µm) by the number of spindle positive sections per individual spindle. Cross sectional area and calculated length were used to calculate muscle spindle volume. Measurements of all muscle spindles were averaged per genotype. Averages of all muscle spindles were analyzed for statistical significance by Student's *t*-test.

Statistical analysis.

Average measurements for each observation from the balance beam results were analyzed for statistical significance by two-way repeated measures ANOVA followed by a Holm Sidak *post hoc* test (SigmaPlot, Systat Software Inc., San Jose, CA, US). Average measurements of axon counts, thermal nociception, mechanical nociception, auditory brainstem responses and muscle spindle analyses were all analyzed for statistical significance by Student's *t*-test.

2.4. Results.

Reduced motor coordination in hNF-L^{E396K} mice.

Time walking, distance walked, and walking speed.

To analyze overall motor performance, we measured the total time spent walking (Fig. 2.1A), the distance walked (Fig. 2.1B) and the average walking speed (Fig. 2.1C) at each day tested. No significant differences were observed in any measurement between genotypes or across days tested.

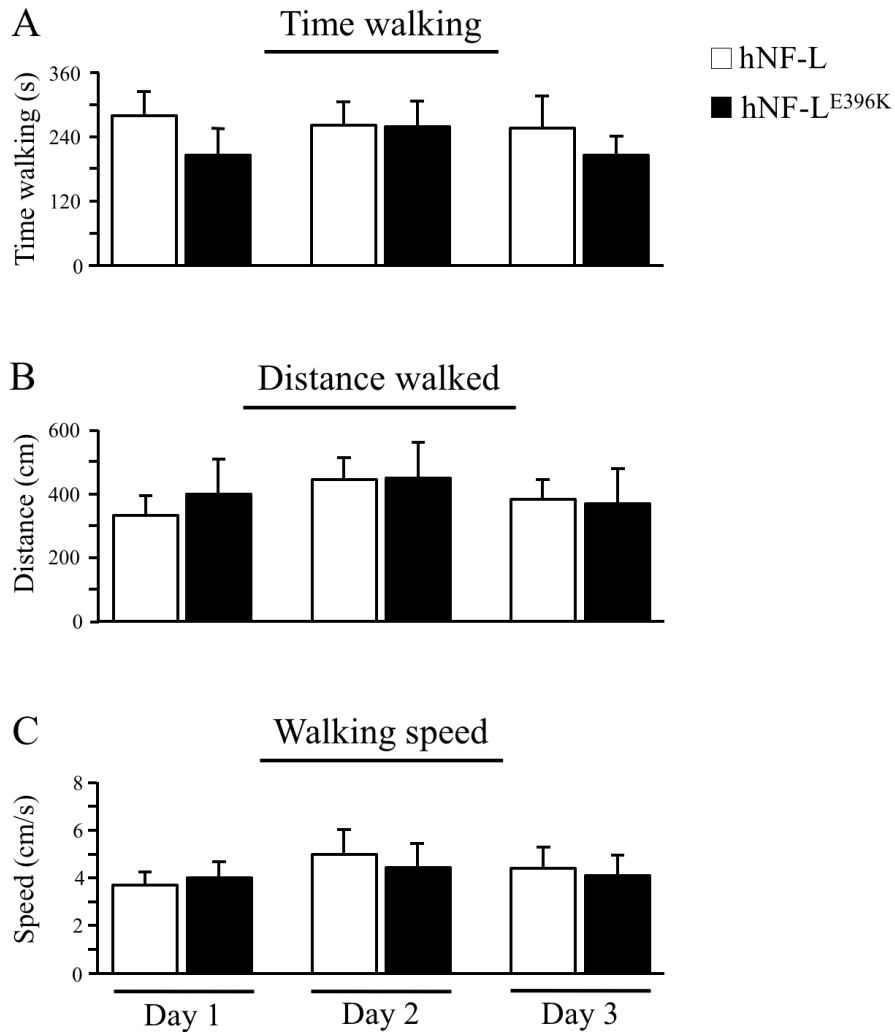


Figure 2.1. Ability to traverse the balance beam was not altered in symptomatic hNF-L^{E396K} mice. Ability to traverse the beam was analyzed by measuring total walking time, distance walked, and walking speed in 5 - 6-month-old hNF-L and hNF-L^{E396K} mice. No differences were observed in total walking time (A), distance walked (B) or walking speed (C) on any day between symptomatic hNF-L^{E396K} and hNF-L control mice. All observations were averaged per day per genotype, and analyzed for statistical significance by two-way repeated measures ANOVA followed by a Holm Sidak post-hoc test for pairwise comparisons. Error bars = SEM. N = 6 for hNF-L and hNF-L^{E396K}.

Falls

The frequency of falls was also used to investigate motor coordination and balance (Carter et al., 1999; Lepicard et al., 2003). hNF-L^{E396K} mice had significantly ($F_{2,20} = 7.84$, $p < 0.001$) more falls (~3.0 fold) on day 1 compared to hNF-L controls (Fig. 2A). On days 2 and 3, the number of falls in hNF-L^{E396K} mice significantly dropped relative to day 1 ($F_{1,2} = 1.60$, $p = 0.0$, day 1 vs. day 2; $F_{1,2} = 1.60$ $p = 0.034$, day 1 vs. day 3) such that there was no difference between hNF-L^{E396K} and hNF-L mice. This suggested that hNF-L^{E396K} mice adapted to the balance beam. hNF-L control falls remained similar throughout all three days (Fig. 2.2A).

Foot Slips.

Quantifying foot slips is an established method for analyzing motor coordination (Carter et al., 1999; Stanley et al., 2005), and increased slips reflect proprioceptive dysfunction (Muller et al., 2008; Taylor et al., 2001). A foot slip was classified as any event in which a paw fell off the top of the beam (Fig. 2.2B). The number of foot slips was quantified per trial on all test days. On day 1, hNF-L^{E396K} mice had ~ 2.0 times more foot slips compared to the hNF-L controls (Fig. 2.2C). However, these differences did not reach statistical significance. By day 2, the number of foot slips increased to ~2.5 times more than the controls (Fig. 2.2C), which was statistically significant ($F_{1,8} = 39.50$, $p = 0.031$). On day 3, the number of foot slips increased to ~3.5 times more than hNF-L controls (Fig. 2.2C). The number of foot slips on day 3 was significantly higher than controls ($F_{1, 8} = 39.50$ $p < 0.001$), and was also significant relative to hNF-L^{E396K} foot

slips on day 2 ($F_{2,16} = 4.50$, $p = 0.020$) and day 1 ($F_{2,16} = 4.50$, $p = 0.002$). The number of foot slips did not change throughout the study for age matched hNF-L control mice (Fig. 2.2C). Taken together these analyses suggested that symptomatic hNF-L^{E396K} mice developed alterations in motor coordination consistent with loss of joint position sense.

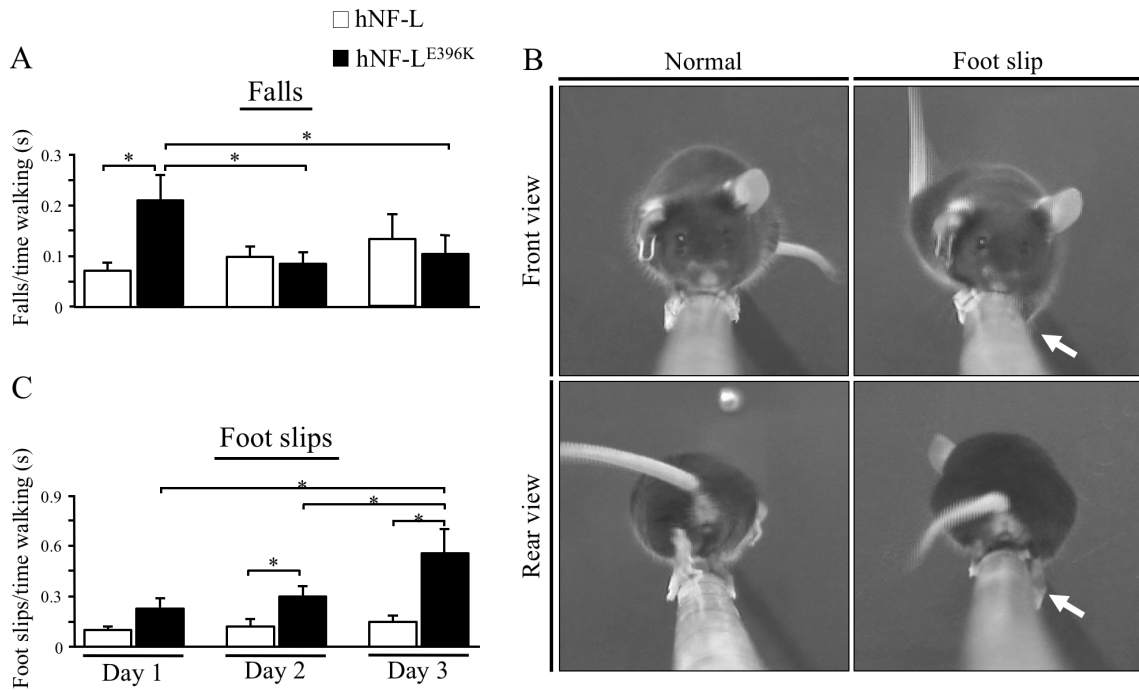


Figure 2.2. Motor coordination was reduced in symptomatic hNF-L^{E396K} mice. Motor coordination was analyzed by balance beam in 5 - 6-month-old hNF-L^{E396K} and hNF-L mice. (A) On day 1, symptomatic hNF-L^{E396K} mice had significantly more falls than aged matched hNF-L control mice. However, by day 2 and 3, symptomatic hNF-L^{E396K} mice fell the same number of times as hNF-L control mice. (B) Illustration of a normal mouse on the balance beam (left) and a mouse experiencing a foot slip (right). A foot slip was considered any event when the foot fell below the top surface of the beam (arrows). (C) Symptomatic hNF-L^{E396K} mice had a progressive increase in the number of foot slips on the balance beam over the three consecutive days. All observations were averaged per day per genotype, and analyzed for statistical significance by two-way repeated measures ANOVA followed by a Holm Sidak post-hoc test for pairwise comparisons. Error bars = SEM. N = 6 for hNF-L and hNF-L^{E396K}. * = p < 0.05.

Attenuated response to mechanical but not thermal nociception in hNF-L^{E396K} mice.

We utilized two different paradigms to analyze nociception and target specific sensory axons in 6-month-old hNF-L and hNF-L^{E396K} mice: mechanical (group II, large myelinated axons) (Fig. 2.3) and thermal nociception (group III and IV, and unmyelinated) (Fig. 2.4). hNF-L^{E396K} mice required significantly more force to elicit a response in both the right hind ($p = 0.001$) (Fig. 2.3A) and left hind ($p = 0.013$) (Fig. 2.3B) paws compared to hNF-L controls. No differences were observed in evoked response in either right (Fig. 2.3C) or left front (Fig. 2.3D) paw. We analyzed thermal nociception by Hargreaves assay (Fig. 2.4). No differences were found in temperature threshold required to elicit a response (Fig. 2.4A – 4D), suggesting that reduction in mechanical nociception was not due to a generalized reduction in nociception. Taken together these results indicate that hNF-L^{E396K} mice develop deficits in large sensory axon function without altered function of small diameter sensory axons.

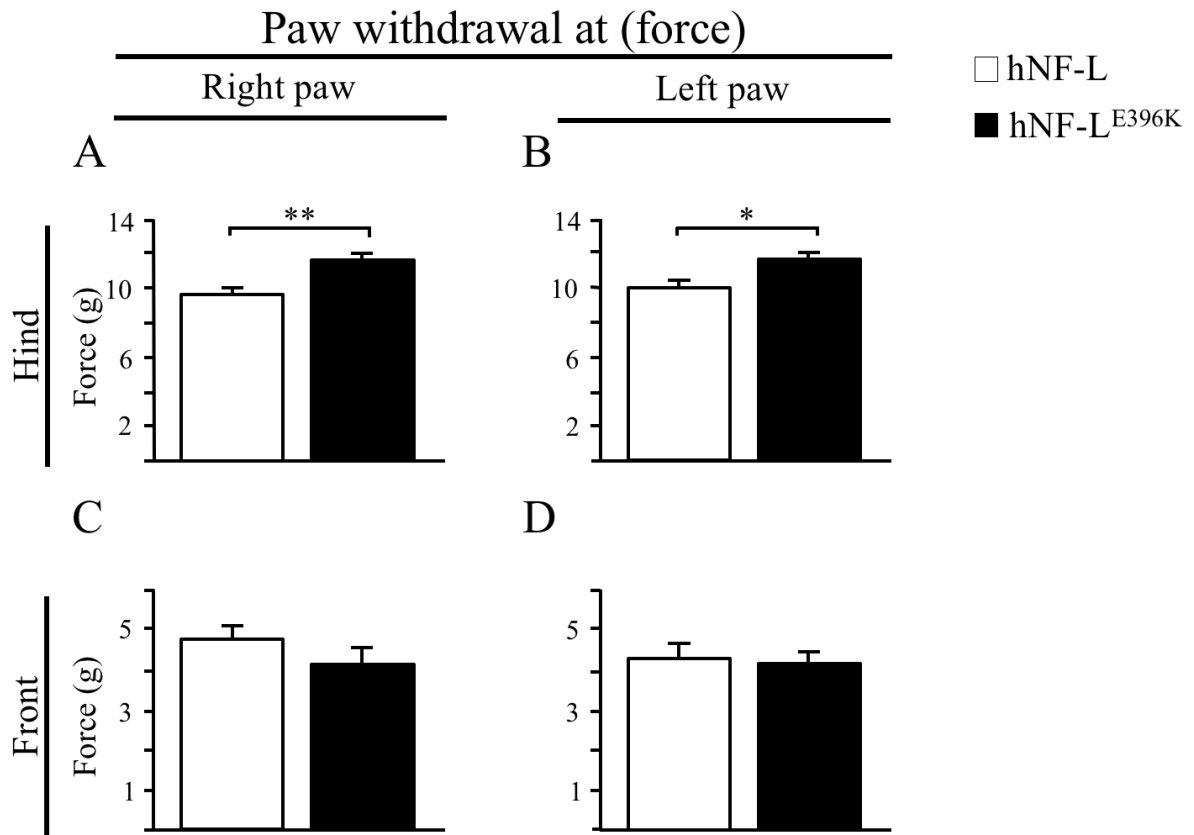


Figure 2.3. Sensitivity to mechanical stimulation was reduced in hind limbs of symptomatic hNF-L^{E396K} mice. Flexor withdrawal reflex was measured in 6-month-old hNF-L^{E396K} and hNF-L mice. (A and B) Grams of force required to elicit the withdrawal reflex was significantly higher in the right hind (A) and left hind (B) paws of symptomatic hNF-L^{E396K} mice compared to age matched hNF-L mice. (C and D) No differences were observed in the amount of force required to elicit a response in the right (C) or left (D) front paws. All observations were averaged per genotype, and analyzed for statistical significance by a Student's *t*-test. Error bars = SEM. N = 8 for hNF-L controls, and N = 15 for hNF-L^{E396K}. * = $p < 0.05$, ** = $p < 0.001$.

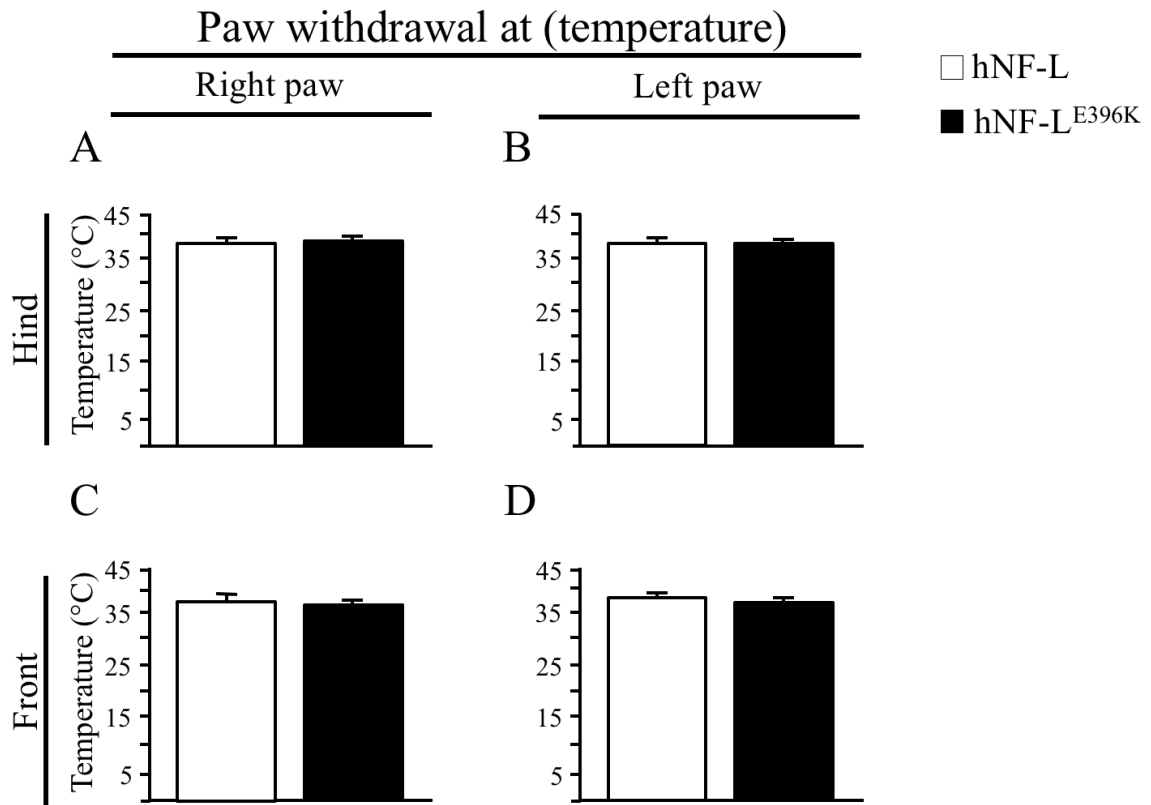


Figure 2.4. Sensitivity to thermal stimulation was not affected in symptomatic hNF-L^{E396K} mice. The flexor withdrawal reflex was further analyzed utilizing noxious thermal stimulation in 6-month-old hNF-L and hNF-L^{E396K} mice. (A, B, C, and D). No differences in response to noxious thermal stimulation were observed in the right hind (A), left hind (B), right front (C), or left front (D) paws between symptomatic hNF-L^{E396K} or hNF-L control mice. Measurements were averaged per paw and genotype, and analyzed for statistical significance using a Student's *t*-test. Error bars = SEM. N = 15 for hNF-L and N = 22 for hNF-L^{E396K}.

Progression from pre-symptomatic to symptomatic correlated with loss of large diameter sensory axons in hNF-L^{E396K} mice.

Increased number of foot slips and decreased sensitivity to touch suggested alterations in proprioceptive and mechanoreceptive sensory neurons, which are large myelinated ($>5\ \mu\text{m}$) sensory axons (Casellini and Vinik, 2007; Tourtellotte and Milbrandt, 1998). In 2-month-old hNF-L^{E396K} mice, the number of small ($\leq 5\ \mu\text{m}$) (Fig. 2.5A) and large ($>5\ \mu\text{m}$) (Fig. 2.5B) diameter axons was indistinguishable from age matched hNF-L controls. Aging from 2 to 6 months resulted in a reduction of ~ 300 small sensory axons in both hNF-L and hNF-L^{E396K} mice (Fig. 2.5C). Concomitantly, the number of large sensory axons increased by ~ 300 axons in hNF-L control mice (Fig. 2.5D). However, there was no increase in the number of large diameter sensory axons in 6-month-old hNF-L^{E396K} mice resulting in significantly fewer large sensory axons relative to age matched hNF-L controls (Fig. 2.5D), which is consistent with previous data showing a decrease (non-significant) of similar magnitude in the total number of sensory axons in symptomatic hNF-L^{E396K} mice (Shen et al., 2011). Thus, our current analysis demonstrates that progressing from pre-symptomatic to symptomatic was associated with a specific loss of ~ 300 ($\sim 50\%$) large diameter sensory axons in hNF-L^{E396K} mice.

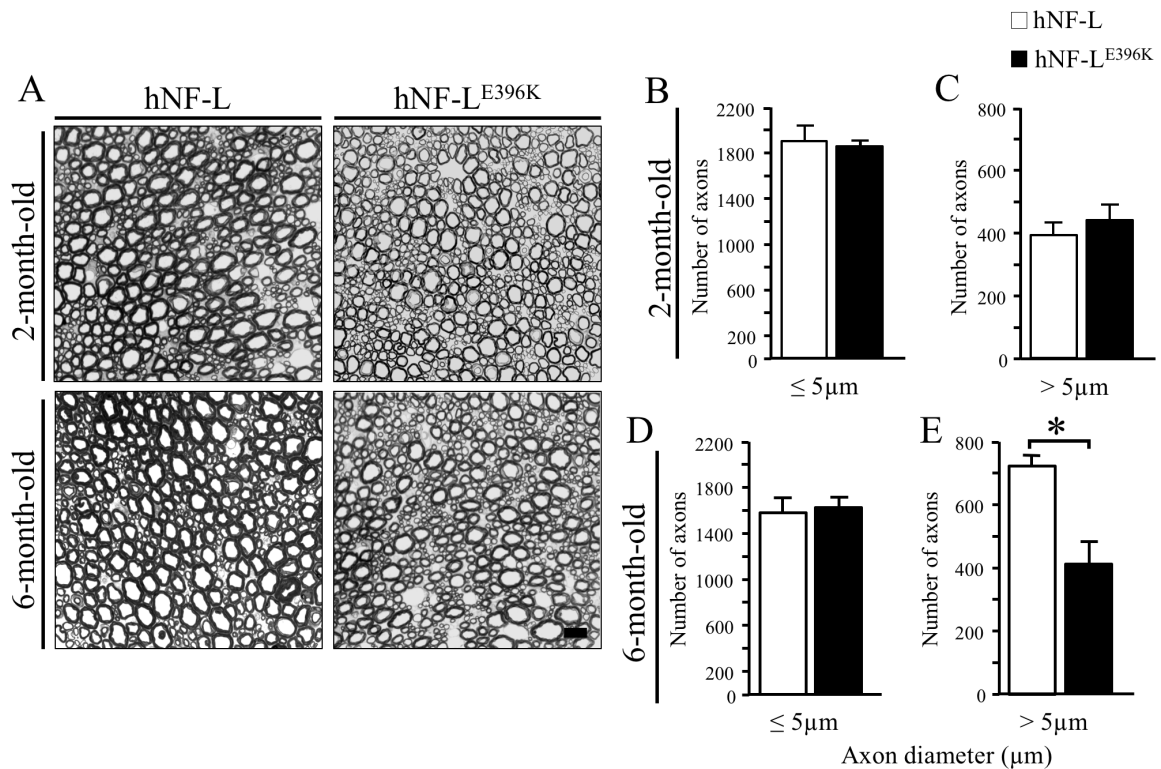


Figure 2.5. Progression from pre-symptomatic to symptomatic resulted in loss of large diameter sensory axons in hNF-L^{E396K} mice. Representative micrographs of hNF-L and hNF-L^{E396K} fifth lumbar sensory roots (scale bar = 10μm) (A). Fifth lumbar sensory root axons were divided into small (< 5μm) and large (> 5μm) diameter populations in 2-month-old and 6-month-old hNF-L and hNF-L^{E396K} mice. (B and C) The number of small (B) and large (C) diameter sensory axons was not different in pre-symptomatic hNF-L^{E396K} and age matched hNF-L controls. (D) In symptomatic hNF-L^{E396K} and age matched hNF-L mice, small diameter sensory axons were reduced by approximately 300 axons. As hNF-L and hNF-L^{E396K} both had reduced numbers, there was no difference in total number of small diameter axons. (E) In 6-month-old hNF-L mice, the number of large diameter axons was increased by approximately 300 axons. However, large diameter axons did not increase in symptomatic hNF-L^{E396K} mice resulting in a significant reduction in the total number of large diameter axons. Axon counts were averaged per genotype and analyzed for statistical significance by a Student's *t*-test. Error bars = SEM. N = 3 for 2-month-old hNF-L and hNF-L^{E396K}. N = 4 for 6-month-old hNF-L and hNF-L^{E396K}. * = p < 0.05.

Muscle spindles cross sectional area and volume were reduced prior to disease onset in CMT2E mice.

To determine if the loss of large diameter sensory axons was associated with alterations in muscle spindle number or morphology we analyzed muscle spindles from the EDL muscle. In each muscle section, several muscle spindles were identified (Fig. 2.6A). Each muscle spindle was then traced (as illustrated in Fig. 2.6B) to count the total number of muscle spindles in each muscle. No differences in muscle spindle number were found in 2 or 6-month-old hNF-L^{E396K} mice compared to age matched hNF-L controls (Fig. 2.6C).

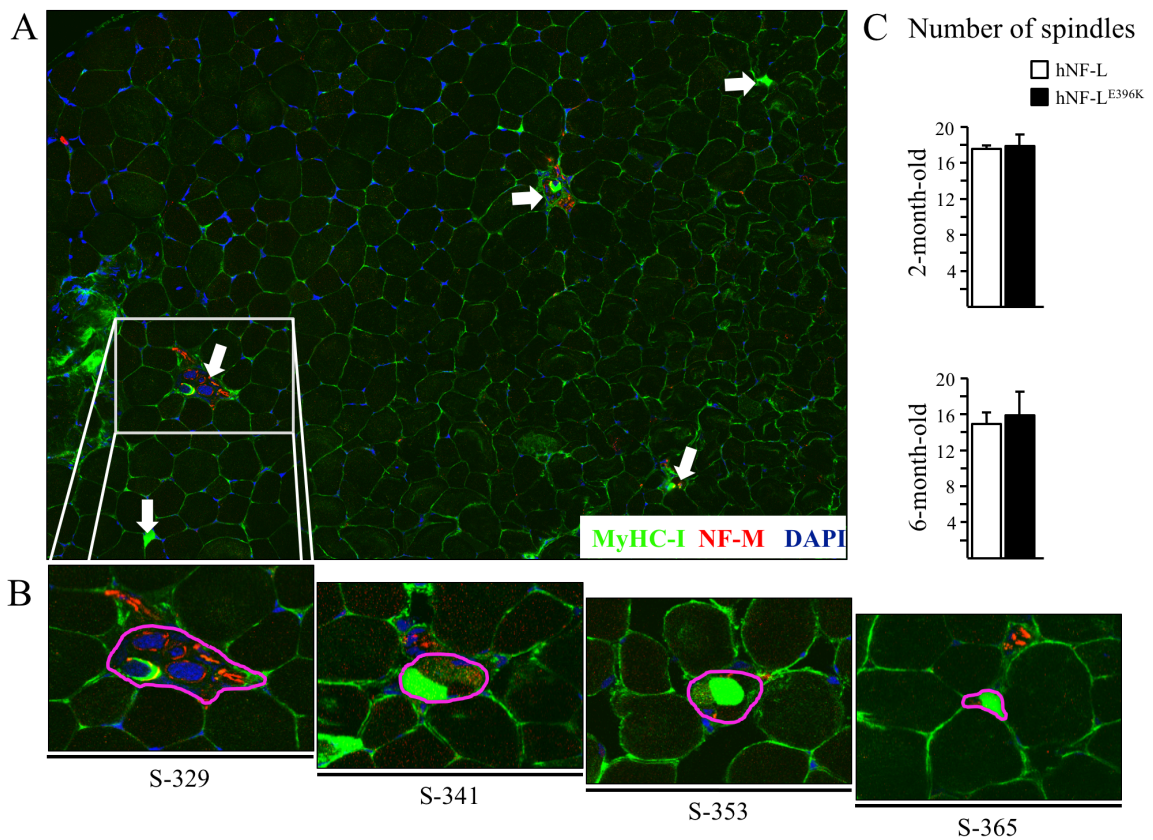


Figure 2.6. Muscle spindle number was unaffected in extensor digitorum longus muscles from pre-symptomatic and symptomatic hNF-L^{E396K} mice. (A) Extensor digitorum longus (EDL) muscles were serially sectioned (16 μ m), and every 12th serial section was immunostained using antibodies specific for myosin heavy chain type I (green) and neurofilament medium (red) to identify muscle spindles and associated axons (arrows point to individual muscle spindles). (B) Individual muscle spindles were traced through the sections they appeared in and the area they occupied was outlined for cross sectional area analyses. (C) Muscle spindles were counted in 2 and 6-month-old hNF-L and hNF-L^{E396K} mice. No difference was observed in muscle spindle number in pre-symptomatic or symptomatic hNF-L^{E396K} mice compared to respective age matched hNF-L controls. Muscle spindles were averaged per genotype and analyzed for statistical significance by a Student's *t*-test. Error bars = SEM. N = 3 for both hNF-L and hNF-L^{E396K}. S-329: section 329, S-341: section 341, etc.

The maximum ($p = 0.032$) (Fig. 7A), median ($p = 0.040$) (Fig. 2.7B), and minimum ($p = 0.010$) (Fig. 2.7C) cross sectional area were significantly reduced in 2-month-old hNF-L^{E396K} mice. Similarly, in 6-month-old hNF-L^{E396K}, the maximum ($p = 0.341$) (Fig. 2.7D), median ($p = 0.001$) (Fig. 2.7E) and minimum ($p = 0.018$) (Fig. 2.7F) cross sectional area were reduced in 6-month-old hNF-L^{E396K} mice compared to age matched hNF-L controls.

Muscle spindle cross-sectional area

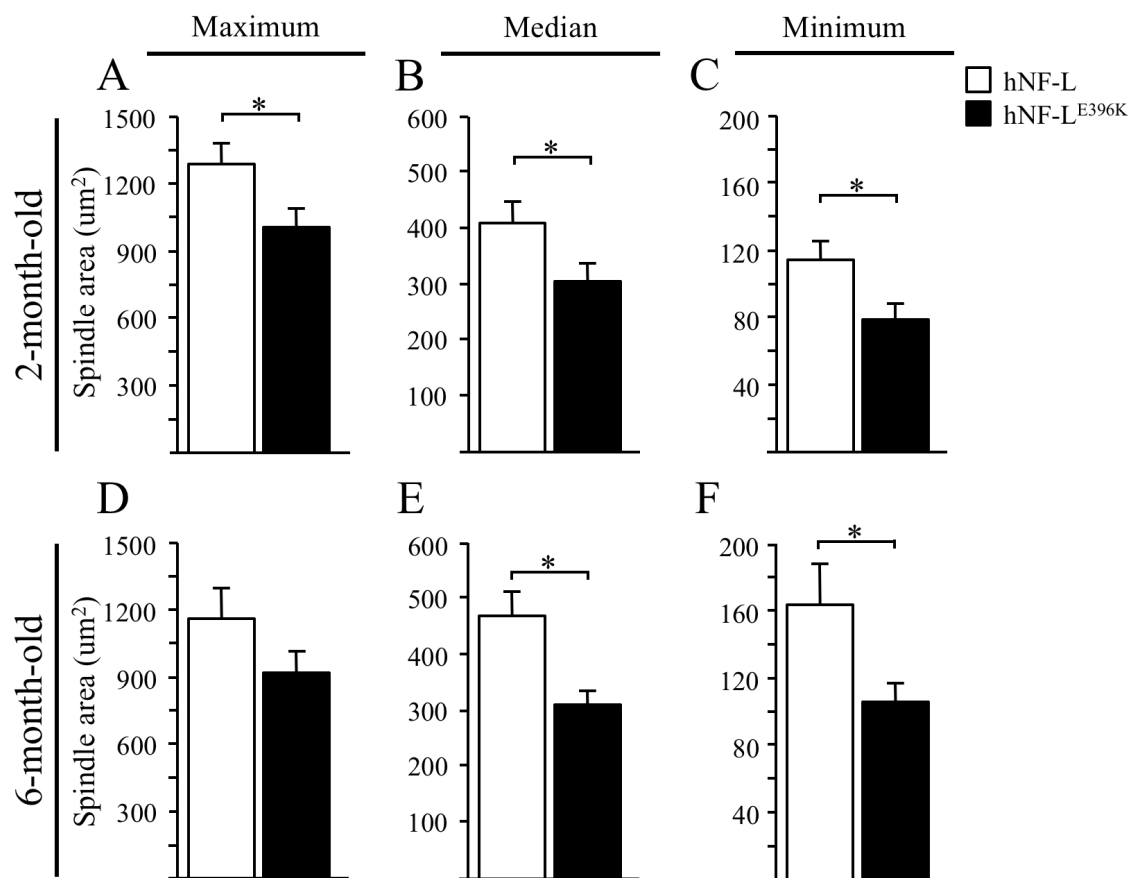


Figure 2.7. Muscle spindle cross sectional area was reduced in pre-symptomatic and symptomatic hNF-L^{E396K} mice. Muscle spindle cross sectional area was analyzed in 2 and 6-month-old hNF-L and hNF-L^{E396K} mice. (A, B, and C) Maximum (A), median (B), and minimum (C) muscle spindle cross sectional area was significantly reduced in pre-symptomatic hNF-L^{E396K} mice relative to age matched hNF-L controls. (D) Maximum cross sectional area was reduced in symptomatic hNF-L^{E396K} mice compared to age matched hNF-L controls. However, the differences did not reach statistical significance. (E and F) Median (E) and minimum (F) muscle spindle cross sectional area was significantly reduced in symptomatic hNF-L^{E396K} mice compared to age matched hNF-L controls. Averages per genotype were calculated from measurements of all counted muscle spindles, and analyzed for statistical significance by a Student's *t*-test. Error bars = SEM. N ≥ 15 for both hNF-L and hNF-L^{E396K}. * = p < 0.05.

Muscle spindle length calculations revealed no difference in muscle spindle length between 2-month-old hNF-L^{E396K} (Fig. 2.8A) or 6-month-old hNF-L^{E396K} (Fig. 2.8B) and age matched hNF-L controls.

Utilizing the maximum area, minimum area, and length data we calculated the volume occupied by each muscle spindle. Our results revealed a significant decrease in muscle spindle volume of ~25% in 2-month-old (Fig. 2.8C) ($p = 0.027$) and ~26% in 6-month-old (Fig. 2.8D) ($p = 0.018$) hNF-L^{E396K} mice compared to the corresponding age matched controls. Taken together these data suggested that alterations in muscle spindle morphology preceded the loss of large diameter sensory axons in hNF-L^{E396K} mice.

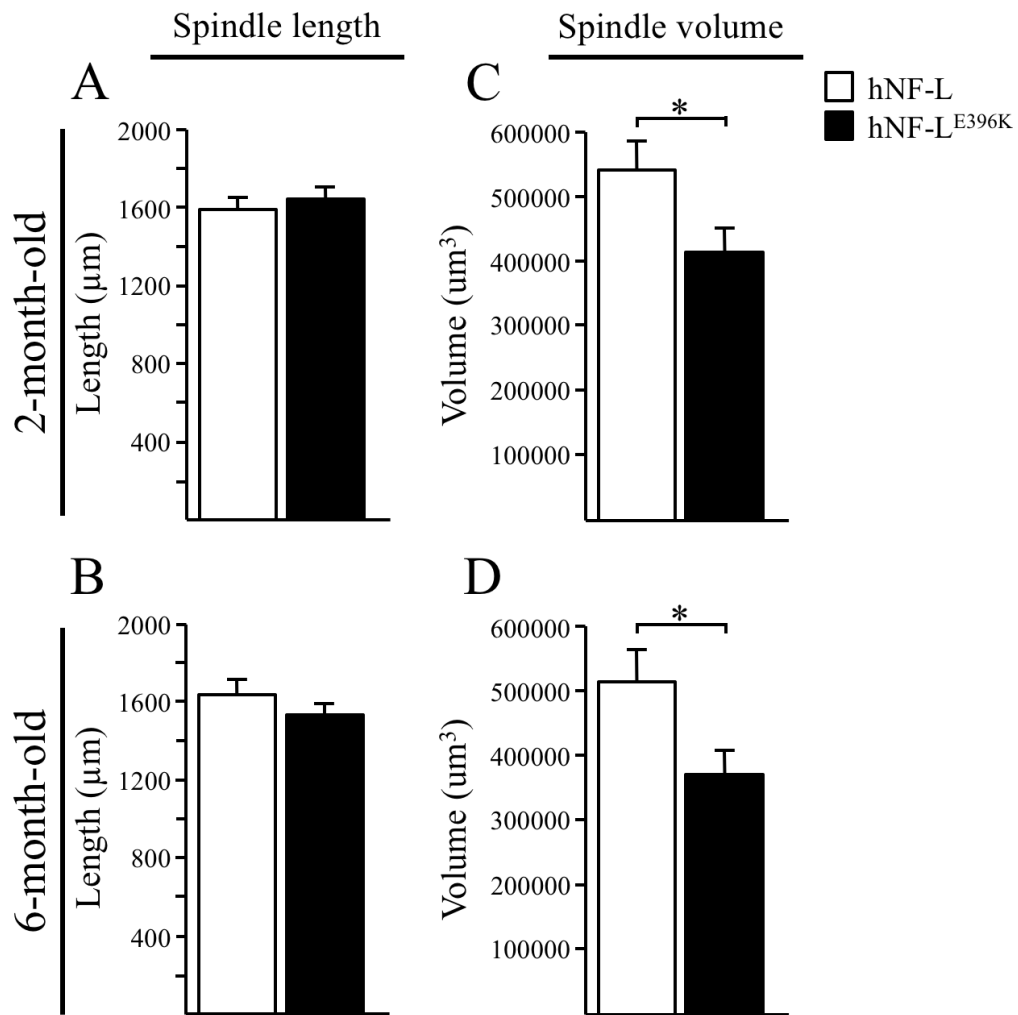


Figure 2.8. Muscle spindle volume was reduced in pre-symptomatic and symptomatic hNF-L^{E396K} mice. Muscle spindle length and volume were calculated in 2 and 6-month-old hNF-L and hNF-L^{E396K} mice. (A and B) Muscle spindle length was not different in pre-symptomatic (A) and symptomatic (B) hNF-L^{E396K} mice relative to age matched hNF-L controls. (C and D) There was a significant reduction in muscle spindle volume in pre-symptomatic (C) and symptomatic (D) hNF-L^{E396K} mice compared to age matched hNF-L controls. Averages per genotype were calculated from measurements of all counted muscle spindles, and analyzed for statistical significance by a Student's *t*-test. Error bars = SEM. N ≥ 15 for both hNF-L and hNF-L^{E396K}. * = p < 0.05.

2.5. Discussion.

Expressing hNF-L^{E396K} in mice recapitulated many of the phenotypes observed in patients (Dale et al., 2012; Shen et al., 2011; Villalon et al., 2015). The first overt phenotype observed in hNF-L^{E396K} mice was reduced ability to spread toes and reduced ability to abduct hind limbs, which was visible in ~4 month old mice (Shen et al., 2011). This initial phenotype was suggestive of sensorimotor defects, but does not identify the site of pathogenesis. Our analyses have identified alterations that occur before onset of aberrant hind limb posture. At one month, neurofilament accumulations were visible in motor neuron cell bodies (Shen et al., 2011). Ectopic accumulations persisted to 13 months, but were not progressive (Shen et al., 2011). At two months, muscle spindle cross sectional area and volume were reduced, and axon diameter was reduced in gamma motor neurons (Shen et al., 2011). These early alterations support pathogenesis within sensorimotor systems with predominant involvement of the proprioceptive system.

Altered motor function could contribute to many of the subsequent phenotypes. Reduced hind limb abduction is a gross measurement of sensorimotor function that could be explained by muscle weakness due to altered motor function (Clark, 2009). Motor coordination was compromised in freely ambulating hNF-L^{E396K} mice on a flat surface, which included left hind limb drag (Dale et al., 2012). Foot drop is associated with muscle weakness (Bird, 1993a; Bird, 1993b). Muscle atrophy could directly result from reduced motor function (Akay, 2014; Boillee et al., 2006) or indirectly from reduced voluntary activity (Clark, 2009), which was observed in hNF-L^{E396K} mice (Shen et al., 2011).

Sensory dysfunction observed in hNF-L^{E396K} mice was specific to functions mediated by large diameter sensory axons. Increased number of foot slips on balance beam suggested possible dysfunction of group Ia or Ib sensory axons, which are large diameter sensory axons that transmit proprioception and joint position sense, respectively (Gilman, 2002). Furthermore, sensitivity to mechanical stimulation suggested altered function in group II sensory axons, which are also large sensory axons (Casellini and Vinik, 2007). However, functions mediated by unmyelinated axons, thermal nociception (Yeomans et al., 1996; Yeomans and Proudfit, 1996), and small, myelinated axons, auditory brainstem responses (Fig. 2.9) (Gleich and Wilson, 1993), were unaltered suggesting normal axonal function. Furthermore, morphological analysis of sensory axons supported large axon specificity, and identified a population of late developing sensory axons that were particularly vulnerable. Quantification of sensory axons at 2- and 6-months in hNF-L mice suggested an age related expansion in axonal diameter resulting in an increased number of large axons by ~300 axons. hNF-L^{E396K} mice also had a reduction in the number of small sensory axons, but the number of large diameter axons failed to increase suggesting loss of ~300 large sensory axons. Thus, functional deficits and morphological alterations indicated that hNF-L^{E396K}-linked CMT2E primarily affected sensory systems that utilize large diameter axons.

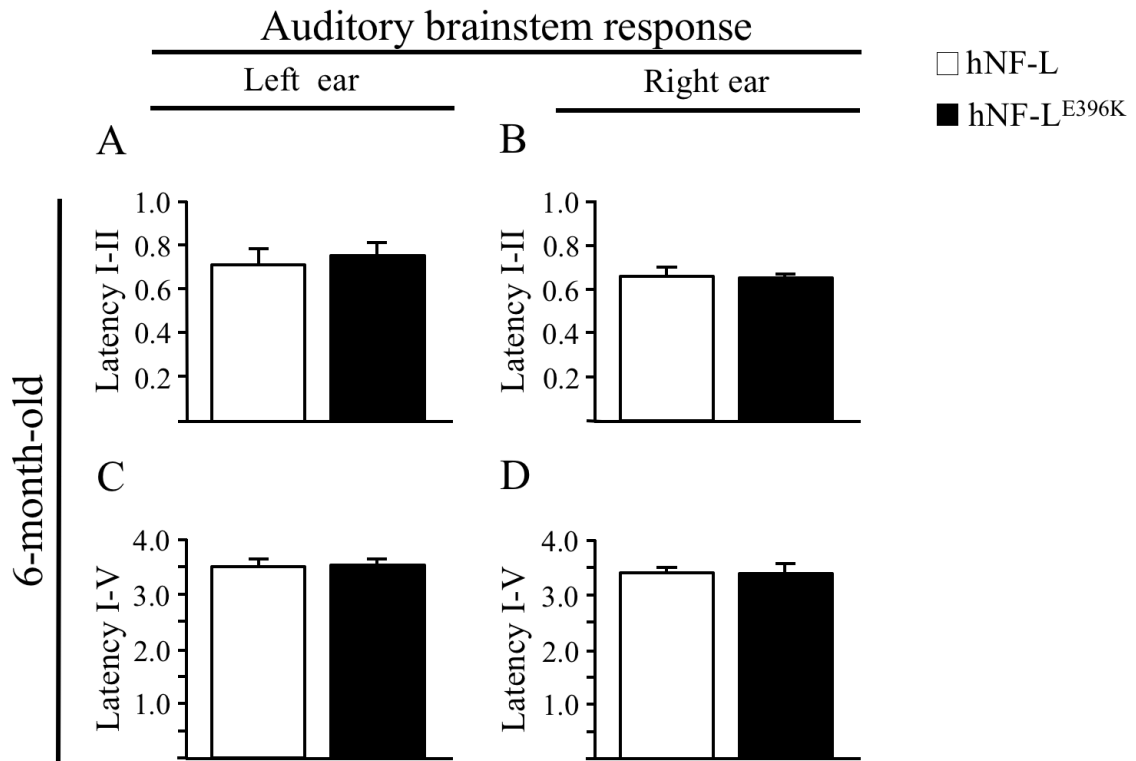


Figure 2.9. Auditory Brainstem Responses (ABRs) were unaltered in symptomatic hNF-L^{E396K} mice. ABRs were recorded in 6-month-old hNF-L^{E396K} and hNF-L mice (A, B, C, and D). No differences were found in the response latency from the peak of waveform I-II between symptomatic hNF-L^{E396K} and age matched hNF-L mice in the left ear (A) or the right ear (B). Response latencies from the peak of waveform I-IV were also not different between symptomatic hNF-L^{E396K} and age matched hNF-L controls in the left ear (C) or the right ear (D). Averages per genotype were calculated and analyzed for statistical significance by a Student's *t*-test. Error bars = SEM. N = 4 for both hNF-L and hNF-L^{E396K}.

Muscle spindle cross sectional area and volume were significantly reduced in 2-month-old hNF-L^{E396K} mice. Loss of large sensory axons occurred subsequent to muscle spindle alterations. Moreover, gamma motor axon diameter was also reduced prior to onset of aberrant hind limb posture (Shen et al., 2011). It is possible that reduced function and altered morphology of muscle spindles in hNF-L^{E396K} mice resulted in secondary loss of large sensory axons and reduced gamma motor axon diameter. While the phenotype is much more extreme than the phenotype observed in hNF-L^{E396K} mice, muscle spindle agenesis resulted in secondary loss of large myelinated sensory and gamma motor axons during development in *Egr3*^{-/-} mice (Tourtellotte and Milbrandt, 1998). However, further analysis is required to determine cause and effect in hNF-L^{E396K} mice, as muscle spindles do form in hNF-L^{E396K} mice.

Approximately 60 genes with over 900 unique mutations have been linked to a type of CMT (Bouhy and Timmerman, 2013). Given the large number of genes, it is unclear how mutations in such a wide array of genes that are expressed in different cell types leads to similar clinical presentations. Analysis of rodent models may begin to offer insights into convergence of disease phenotypes. Previous analyses of several CMT rodent models suggest early alterations in sensory systems (Achilli et al., 2009; d'Ydewalle et al., 2011; Gillespie et al., 2000; Lee et al., 2013; Sereda et al., 1996). Our analyses of hNF-L^{E396K} mice suggest early changes in sensorimotor systems with predominant involvement of the proprioceptive system. Therefore, early and selective dysfunction in proprioceptive sensory systems might provide a unifying hypothesis of disease pathogenesis in CMT.

Given the heterogeneity of disease onset even within families with the same mutation (Berciano et al., 2015; Züchner et al., 2004), investigating proprioceptive system defects might be a useful diagnostic tool for early detection of pathologic changes in patients with family history of CMT. Moreover, specific alterations in proprioceptive systems observed prior to the onset of CMT-like pathology suggest that early intervention with therapies designed to enhance or maintain proprioception could be of significant therapeutic value to CMT patients

CHAPTER 3

EXACERBATION OF CHARCOT-MARIE-TOOTH TYPE 2E NEUROPATHY FOLLOWING TRAUMATIC NERVE INJURY

(This work was published in *Brain and Behavior*. 2015. Vol. 1627. p. 143 - 153)

Eric Villalon^{1,2}, Jeffrey M. Dale, Hailian Shen³, and Michael L. Garcia^{1,2†}

¹Division of Biological Sciences, ²Bond Life Sciences Center, University of Missouri-Columbia, Columbia, MO 65211, USA.

³CurRenji-Medx Clinical Stem Cell Research Center, Renji Hospital, School of Medicine, Shanghai Jiaotong University, Shanghai, China 200127.

Keywords: Charcot-Marie-Tooth type 2E, neuropathy exacerbation, nerve injury, functional recovery, gait alterations, neurofilament.

3.1. Abstract.

Charcot-Marie-Tooth disease (CMT) is the most commonly inherited peripheral neuropathy. CMT disease signs include distal limb neuropathy, abnormal gait, sensory defects, and deafness. We generated a novel line of CMT2E mice expressing hNF-L^{E397K}, which displayed muscle atrophy of the lower limbs without denervation, proximal reduction in large caliber axons, and decreased nerve conduction velocity. In this study, we challenged wild type, hNF-L, and hNF-L^{E397K} mice with crush injury to the sciatic nerve. We analyzed functional recovery by measuring toe spread and analyzed gait using the Catwalk system. hNF-L^{E397K} mice demonstrated reduced recovery from nerve injury consistent with increased susceptibility to neuropathy observed in CMT patients. In addition, hNF-L^{E397K} developed a permanent reduction in their ability to weight bear, increased mechanical allodynia, and premature gait shift in the injured limb, which led to increasingly disrupted interlimb coordination in hNF-L^{E397K}. Exacerbation of neuropathy after injury and identification of gait alterations in combination with previously described pathology suggests that hNF-L^{E397K} mice recapitulate many of clinical signs associated with CMT2. Therefore, hNF-L^{E397K} mice provide a model for determining the efficacy of novel therapies.

3.2. Introduction.

Charcot-Marie-Tooth (CMT) disease is the most commonly inherited peripheral neuropathy (Emery, 1991; Skre, 1974), and it is grouped into four main types, CMT1-4, depending on the specific genetic defect. Despite these different classifications, most CMT patients present wasting of distal limb muscles, reduction in axonal diameters and nerve conduction velocities, sensory defects, deafness, and abnormal gaiting (Emery, 1991; Georgiou et al., 2002; Shy and Patzko, 2011; Züchner et al., 2004). CMT age of onset and severity can vary between sub-types and can vary within a single family (Züchner et al., 2004).

CMT patients can also experience exacerbation of their existing neuropathy. Evidence suggests administration non-toxic doses of prescribed drugs can exacerbate CMT disease neuropathy (Chaudhry et al., 2003; Hildebrand et al., 2000; Martino et al., 2005; Weimer and Podwall, 2006). Patients that were administered such agents developed deterioration of nerve conduction velocity, severe pain, sensory impairments of upper and lower extremities, ataxia of gait, and in some cases inability to walk (Chaudhry et al., 2003; Hildebrand et al., 2000; Martino et al., 2005). The typical intervention in such cases is discontinued administration of agent, which typically leads to incomplete to no recovery (Hildebrand et al., 2000; Weimer and Podwall, 2006). Moreover, upon exacerbation of the neuropathy, the mechanisms leading to poor or incomplete recovery are not well understood and poorly studied due to the lack of a reliable model of neuropathy exacerbation.

Mutations in neurofilament light gene (*nefl*) cause CMT type 2E (Barry et al., 2007; Dale and Garcia, 2012). Neurofilament light (NF-L) protein associates with either

neurofilament medium (NF-M) or heavy (NF-H) to form a 10nm filament (NF) (Lee et al., 1993). Once formed, NFs are intrinsic determinants of axonal diameter (Eyer and Peterson, 1994; Garcia et al., 2003; Xu et al., 1996; Zhu et al., 1997), a major axonal property influencing neuronal conduction velocity (Kriz et al., 2000; Waxman, 1980). Furthermore, NFs provide the axons with structural stability and tensile strength in response to physical stress (Barry et al., 2007; Gilbert, 1975; Lee and Shea, 2014; Rammensee et al., 2007). Currently, there are two well established mouse models of CMT 2E, hNF-L^{P22S} (Dequen et al., 2010) and hNF-L^{E397K} (Shen et al., 2011). hNF-L^{P22S} mice develop hypertrophy of muscle fibers and muscle denervation without neuronal loss (Dequen et al., 2010). hNF-L^{E397K} mice develop muscle atrophy without muscle denervation or significant neuronal loss (Shen et al., 2011). Interestingly, both models develop aberrant hind limb posture, altered gait, and sensorimotor defects, which recapitulate the disease pathology seen in human patients (Dale et al., 2012; Dequen et al., 2010; Filali et al., 2011; Shen et al., 2011). More recently, two additional models of CMT2E have been generated, NF-L^{P8R} and NF-L^{N98S}, of which only NF-L^{N98S} displays molecular pathology similar to human patients (Adebola et al., 2015).

In this study, we investigated the effect of traumatic nerve injury on CMT neuropathy in our hNF-L^{E397K} mouse model by analyzing functional recovery and gait alterations. Evidence suggests that wild type animals develop gait alterations following sciatic nerve crush injury that disappear after recovery (Bozkurt et al., 2008). We found that hNF-L^{E397K} animals, following a nerve injury, develop functional and gait alterations that do not fully recover suggesting increased vulnerability to injury, decreased recovery following injury, or both. Moreover, this data shows that our hNF-L^{E397K} mouse model

could be a viable model to study the mechanisms of neuropathy exacerbation after nerve injury.

3.3. Experimental procedures.

Animals.

All procedures were in compliance with the University of Missouri Animal Care and Use Committee and with all local and federal laws governing the humane treatment of animals. Mice were housed in microisolator cages on a 12-h light/dark cycle and were given food and water *ad libitum*.

Sciatic nerve crush.

Mice were placed under isoflurane anesthesia and the sciatic nerve was exposed via an incision in the flank followed by separation of underlying musculature by blunt dissection. The nerve was crushed using fine jewelers forceps at the level of the obturator tendon. To assess functional recovery of the injured limb, the mouse was induced to spread its toes by briefly lifting the hind limbs off the bench and slowly placing the mouse hind paws back on the floor. During this process the mouse spreads its toes when lifted by the tail and maintains them spread while it is being lowered and placed down on the floor again. The distance between the first and fifth digits was then measured using a compass and a ruler. Measurements were expressed as a percentage of pre-crush spread distance. Measurements were made in triplicate for up to 30 days. Means for each daily toe spread measurement were analyzed for overall statistical differences by two-way repeated measures ANOVA with Holm-Sidak post hoc analysis (SigmaPlot, Systat Software Inc.,

San Jose, CA, US).

Gait.

Gait for hNF-L (n = 9) and symptomatic hNF-L^{E397K} (n = 11) mice was monitored using the Catwalk XT gait analysis system (Noldus Information Technology, Asheville, NC) during the animal's light phase. Gait was analyzed on both hNF-L and hNF-L^{E397K} mice before nerve crush, and at 5, 10, 20 and 25 days after crush. Animals were allowed to ambulate freely on a restricted area of an illuminated glass walkway. Footprints were recorded using a high-speed camera. Runs with average speeds of 2.0 ± 0.5 cm/s were recorded for each animal and mean values were calculated. All means were analyzed for statistical differences by a two way ANOVA followed by a Holm-Sidak *post hoc* analysis for pair wise comparisons. For time course analysis (Supplemental Figures) all means were analyzed for statistical differences by a two way repeated measures ANOVA followed by a Holm-Sidak *post hoc* analysis for pairwise comparisons (SigmaPlot, Systat Software Inc., San Jose, CA, US).

Definition of reported measures.

Print Width.

A rectangle is outlined around each paw so that the paw fits perfectly in the rectangle. Print width is measured by measuring the width (perpendicular to the paw axis) of the rectangle. This gives a measure of the distance between the first and last digit of the paw, perpendicular to the paw axis.

Print length.

This is measured by measuring the length of the rectangle fitted to the paw print. This gives a measure of the distance between the beginning of the heel and the tip of the longest digit parallel to the paw axis.

Max contact area.

Defined as the maximum area contacted by the paw when paw is at maximum contact with the floor during a stance phase.

Max contact at % .

Defined as the percentage time (seconds) since the start of a run that a paw reaches maximum contact with the glass plate relative to the stand phase for that paw. It is defined by the following formula:

$$(1) \quad \text{Max contact at} = \frac{\text{MaxContact at (s)} - \text{Initial Contact (s)}}{\text{Stand (s)}} \times 100\%$$

Max intensity

Is the maximum print intensity that each paw reaches while in contact with the walking surface during the stance phase of the step cycle.

Duty Cycle % .

Defined as the percentage of the Stand phase (s) in a step cycle (stand + swing) and it is defined by:

$$\text{Duty cycle} = \frac{\text{Stand (s)}}{\text{Stand (s)} + \text{Swing (s)}} \times 100\% \quad (2)$$

Couplings.

Defined as the difference between initial contact (IC) of a target paw and the reference paw relative to a reference paw's stride cycle (time interval between first contact of the reference paw and the subsequent contact).

$$\frac{\text{IC}_{\text{target}} - \text{IC}_{\text{reference}}}{\text{Stride cycle}} \times 100 \quad (1)$$

For diagonal (**LH**→RF and **RH**→LF) and ipsilateral (**LH**→LF and **RH**→RF) limb pairs, we assigned the hind paw as the reference paw. For girdle (**LH**→RH and **LF**→RF) limb pairs, we assigned the left paw as the reference paw. For diagonal limb pairs values approaching 0 % are more coordinated and for ipsilateral and girdle limb pairs values approaching 50 % are more coordinated (Dale et al., 2012).

3.4. Results.

Reduced functional recovery after nerve injury in hNF-L^{E397K} mice.

Evidence suggests that pre-existing neuropathies can be exacerbated by non-toxic dosages of neurotoxic agents (Chaudhry et al., 2003). Moreover, many prescribed drugs can exacerbate CMT disease neuropathy in humans (Hildebrand et al., 2000; Weimer and Podwall, 2006). Stopping administration of exacerbating compounds leads to reduced or no recovery in CMT patients (Chaudhry et al., 2003; Hildebrand et al., 2000). It is unclear if reduced or failed recovery is due to enhanced susceptibility to injury or reduced recovery following exposure to noxious stimuli. Therefore, we analyzed functional

recovery from sciatic nerve injury in wild type (n = 10), hNF-L (n = 20), and hNF-L^{E397K} (n = 12) mice. The left sciatic nerve was crushed at the level of the obturator tendon, and toe spread was monitored in the ipsilateral paw (Fig. 3.1A). Distance between the first and fifth digits was measured pre-injury and post-injury (Fig. 3.1B) over a time course of 25 days (Fig. 3.1C). Recovery was analyzed in aged matched wild type, aged matched hNF-L and symptomatic (4 month old) hNF-L^{E397K} mice. Post-injury measurements were plotted as a percentage of the pre-injury values (Fig. 3.1C).

Toe spread recovery in wild type and hNF-L mice was similar over the entire time course. Although, ultimately hNF-L mice recovered to only about 98% of their pre-injury values, this difference was not significant when compared to wild type controls. Recovery in hNF-L^{E397K} mice was similar to hNF-L and wild type controls from day 1 to day 14 post-injury. From day 15 post-injury, functional recovery in hNF-L^{E397K} mice began to plateau while hNF-L and wild type controls continued to recover. Functional recovery in hNF-L^{E397K} was significantly reduced compared to wild type but not compared to hNF-L controls at day 15. From day 16 to day 25 post-injury, recovery in hNF-L^{E397K} mice was significantly lower compared to both controls, with the exception of day 20 where hNF-L^{E397K} recovery was significantly lower only compared to wild type mice (Fig. 3.1C; $p < 0.05$). Unlike wild type and hNF-L controls, hNF-L^{E397K} mice recover to only about 89% of their pre-injury toe spread values (Fig. 3.1C).

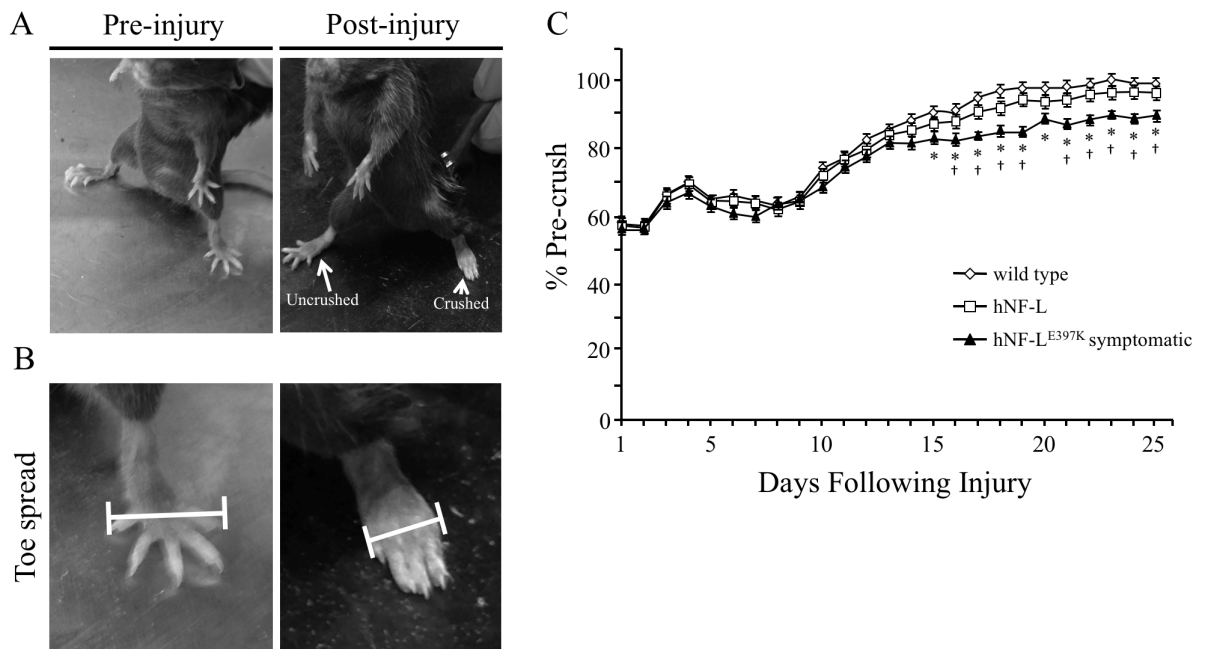


Figure 3.1. Functional recovery from sciatic nerve injury was reduced in hNF-L^{E397K} mice. Sciatic nerves were crushed at the level of the obturator tendon on four-month-old wild type, hNF-L and symptomatic hNF-L^{E397K} mice. Nerve injury prevented toe spread on the injured limb (A). Toe spread was quantified by measuring the distance between the first and fifth digit of the paw (B) over a time course for up to 25 days (C). Wild type and hNF-L mice fully recovered 25 days post-injury (C). Functional recovery was significantly reduced in hNF-L^{E397K} mice beginning at day 15 (C), and hNF-L^{E397K} mice failed to fully recover (C). Means for each daily toe spread measurement were analyzed for overall statistical differences by two way repeated measures ANOVA with Holm-Sidak post hoc analysis. *, $p < 0.05$ as compared to wild type toe spread; †, $p < 0.05$ as compared to hNF-L toe spread.

Gait alterations after recovery from nerve injury.

Wild type animals develop gait alterations following nerve injury. Interestingly, wild type animals are able to completely recover resulting in complete reversal of gait alterations observed with nerve injury (Bozkurt et al., 2008). Moreover, evidence shows that in human patients exacerbation of CMT disease results in sensorimotor defects that cause severe gait alterations (Chaudhry et al., 2003; Hildebrand et al., 2000; Martino et al., 2005). To investigate if nerve injury leads to disease exacerbation and alterations to gait in our hNF-L^{E397K} model, we crushed the left sciatic nerve and analyzed gait. Gait was analyzed pre-injury, 5, 10, 15, and 25 days post-injury (Supplemental Figures). Functional recovery analysis showed maximal recovery 25 days after injury (Fig. 3.1C). Therefore, we have focused the present studies on pre-injury and 25 days post-injury time points. Since there were no differences in functional recovery between wild type and hNF-L control groups, only hNF-L animals were used as controls for gait analysis. The automated CatWalk system has been shown to be effective for objective, rapid and reproducible assessment of individual paw parameters as well as interlimb coordination on freely ambulating animals (Chen et al., 2014; Hamers et al., 2001).

Decreased ability to support weight in injured limb affects gait in diagonal limb.

Print Width: Evidence from rat and mouse neuropathic pain models suggest that decreased ability to bear weight on a limb is strongly correlated with alterations to Print Width, Print Length and Max Contact Area metrics during voluntary locomotion (Angeby-Moller et al., 2008; Gabriel et al., 2007; Medhurst et al., 2002; Min et al., 2001; Tabo et al., 1998). Print Width is defined as the width of the paw from the first to the fifth

digit. Nerve crush recovery analyses showed that hNF-L^{E397K} mice recovered toe spread ability to ~90% of their pre-injury value. Therefore, to investigate if these deficits were also reflected on the Catwalk system, we analyzed the print width of the mice during ambulation. Catwalk analysis revealed that Print Width in both hNF-L and hNF-L^{E397K} mice did not recover to pre-injured values (Fig. 3.2A). Similar to toe spread analysis, hNF-L mice recovered Print Width better than hNF-L^{E397K} mice (Fig. 3.2A). Print Width was also reduced after recovery in hNF-L and hNF-L^{E397K} right, hind limbs (Fig. 3.2B). However, none of the changes reached statistical significance. Interestingly, both front paws had reduced Print Width in hNF-L^{E397K} mice following recovery (Fig. 3.2C and D).

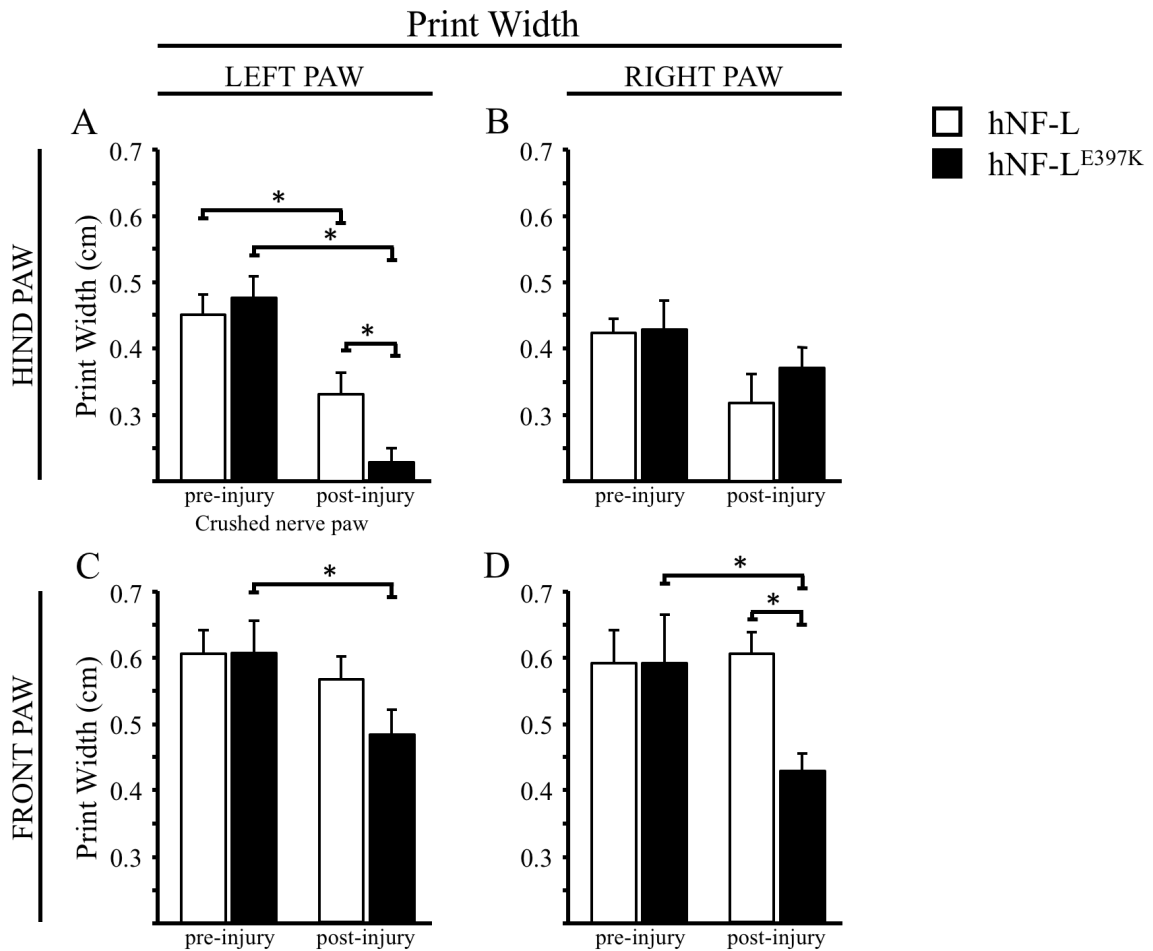


Figure 3.2. Reduced Print Width after nerve crush recovery. Print Width is defined as the width of the paw from the first to the fifth digit. Print width (cm) values are reported for the left hind (A), right hind (B), left front (C), and right front (D) paws from pre-crush and post-injury analyses. Print Width failed to recover to pre-injury values for hNF-L mice only in the left hind paw (A). For hNF-L^{E397K} mice, Print Width was significantly decreased following recovery compared to its pre-injury values for left hind (A), left front (C), and right front (D). On the left hind (A) and right front (D) paw, hNF-L^{E397K} mice recovered less than hNF-L mice. The differences in means were analyzed for overall statistical differences using a two-way ANOVA with Holm-Sidak post hoc analysis. *, $P < 0.05$.

Print Length: Print Length is measured from the beginning of the heel to the tip of the longest digit. CMT patients and mouse models develop alterations in foot structure (Adebola et al., 2015; Dequen et al., 2010; Filali et al., 2011; Shen et al., 2011; Skre, 1974; Züchner et al., 2004), such as hammertoes and high arches, which directly influence paw print length. Therefore, we analyzed Print Length to investigate if our mice develop alterations to this metric following recovery. Moreover, simultaneous reductions in both Print Width and Print Length could indicate the development of neuropathic pain (Angeby-Moller et al., 2008; Gabriel et al., 2007; Medhurst et al., 2002; Min et al., 2001; Tabo et al., 1998). Similar to changes in Print Width, hNF-L and hNF-L^{E397K} mice showed a significant reduction in Print Length following recovery. Moreover, hNF-L mice recovered better than hNF-L^{E397K} mice (Fig. 3.3A). On the right, hind paw, hNF-L mice showed a slight (not significant) decrease in Print Length, while hNF-L^{E397K} showed no alterations post-injury (Fig. 3.3B). Print Length on the left front paw showed slight (not significant) reductions post-injury in both hNF-L and hNF-L^{E397K} (Fig. 3.3C). On the right front paw, hNF-L mice showed no Print Length alterations post-injury. However, Print Length of hNF-L^{E397K} mice was significantly reduced compared to hNF-L Print Length following recovery (Fig. 3.3D).

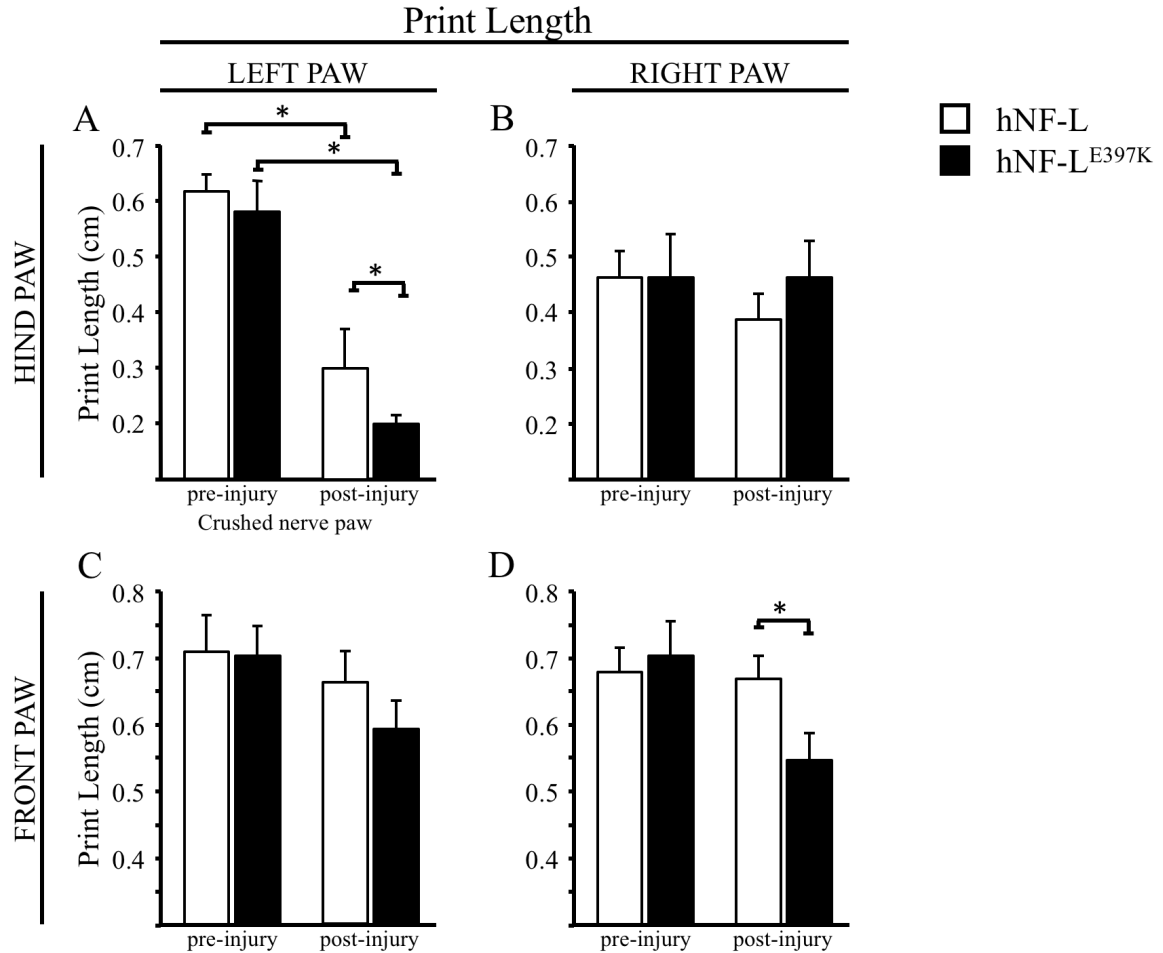


Figure 3.3. Reduced Print Length on the injured limb after recovery. Print Length is measured from the beginning of the heel to the tip of the longest digit. Print Length was significantly lower in hNF-L and hNF-L^{E397K} mice following recovery compared to pre-injury values (A). Additionally, hNF-L^{E397K} mice did not recover Print Length as well as hNF-L mice (A). Print Length values for all right hind and left front paws were unchanged after recovery (B, and C). On the right, front paw, hNF-L^{E397K} lengths were significantly lower compared to hNF-L lengths (D). The differences in means were analyzed for overall statistical differences using a two-way ANOVA with Holm-Sidak post hoc analysis. *, $P < 0.05$.

Max Contact Area: Max Contact Area is a measure of the area contacted by a paw when the most pressure is being applied. On the injured paw, hNF-L and hNF-L^{E397K} mice showed a significant decrease in Max Contact Area following recovery. However, Max Contact Area recovered better in hNF-L mice relative to hNF-L^{E397K} mice (Fig. 3.4A). Reductions in Max Contact Area were observed in the right hind paw of both hNF-L and hNF-L^{E397K} mice, but these changes were not statistically significant (Fig. 3.4B). On the left, front paw, hNF-L mice showed no alterations to Max Contact Area. However, hNF-L^{E397K} Max Contact Area was significantly reduced following recovery compared to hNF-L controls (Fig. 3.4C). Interestingly, recovery of Max Contact Area of the diagonal, right front limb was significantly reduced in hNF-L^{E397K} mice relative to hNF-L mice (Fig. 3.4D).

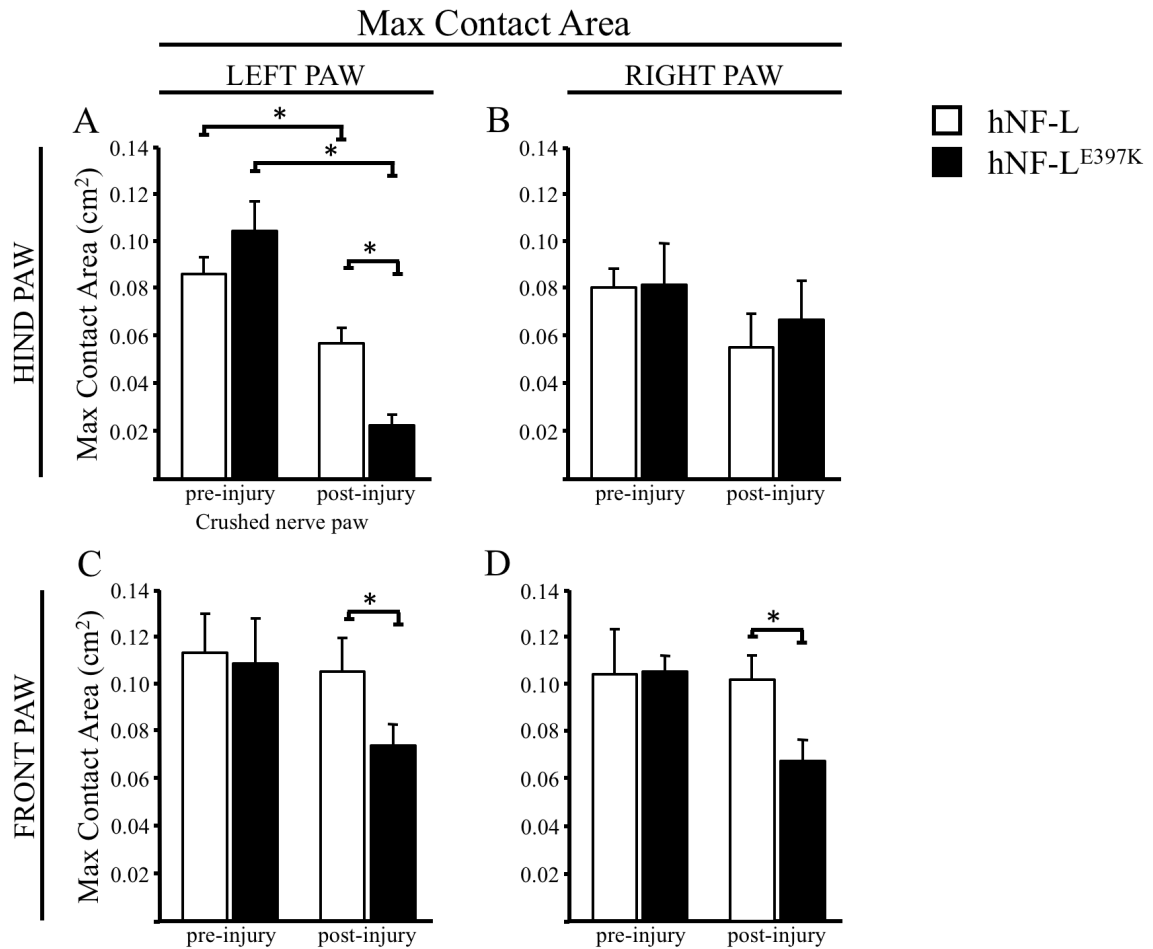


Figure 3.4. Max Contact Area is decreased in hind left and diagonal paw after recovery. Max Contact Area is a measure of the area contacted by a paw when the most pressure is being applied. Max Contact Area was reduced following recovery in the left hind paw of hNF-L and hNF-L^{E397K} mice (A). Additionally, hNF-L^{E397K} mice failed to recover to the same extent as hNF-L (A). Max Contact Area was unaltered in the right hind paw of hNF-L and hNF-L^{E397K} mice (B). Interestingly, Max Contact Area was reduced in left (C) and right (D) front paws in hNF-L^{E397K} mice. The differences in means were analyzed for overall statistical differences using a two-way ANOVA with Holm-Sidak post hoc analysis. *, $P < 0.05$.

Increased mechanical allodynia to injured paw alters weight bearing on diagonal paw after recovery from injury.

Max Intensity is a measure of the maximum light intensity of a paw print, and it correlates with the amount of pressure placed on a paw while the paw is in contact with the glass regardless of the area of contact. This is a parameter that is commonly used to evaluate effects of neuropathic pain, specifically mechanical allodynia (Angeby-Moller et al., 2008; Gabriel et al., 2007; Gabriel et al., 2009; Vrinten and Hamers, 2003). Max Intensity on the injured paw (left hind) of hNF-L mice recovered to values that were similar to pre-injury values (Fig 3.5A). Unlike hNF-L mice, Max Intensity failed to recover in hNF-L^{E397K} mice to pre-injured values (Fig. 3.5A), indicating decreased ability to bear weight. Max Intensity was unaffected in the right hind (Fig. 3.5B) and left front (Fig. 3.5C) paws in either hNF-L or hNF-L^{E397K} mice. Interestingly, the Max Intensity on the right front paw of hNF-L^{E397K} mice was significantly reduced following recovery relative to pre-injury and hNF-L control values (Fig. 3.5D).

These results suggest that hNF-L^{E397K} develop alterations to Max Intensity, which translates into decreased ability to bear weight, on the injured paw that do not return to baseline levels after recovery from nerve injury. Moreover, our results also suggest that hNF-L^{E397K} mice develop similar weight bearing deficits on the uninjured diagonal paw (right front) after recovery from injury.

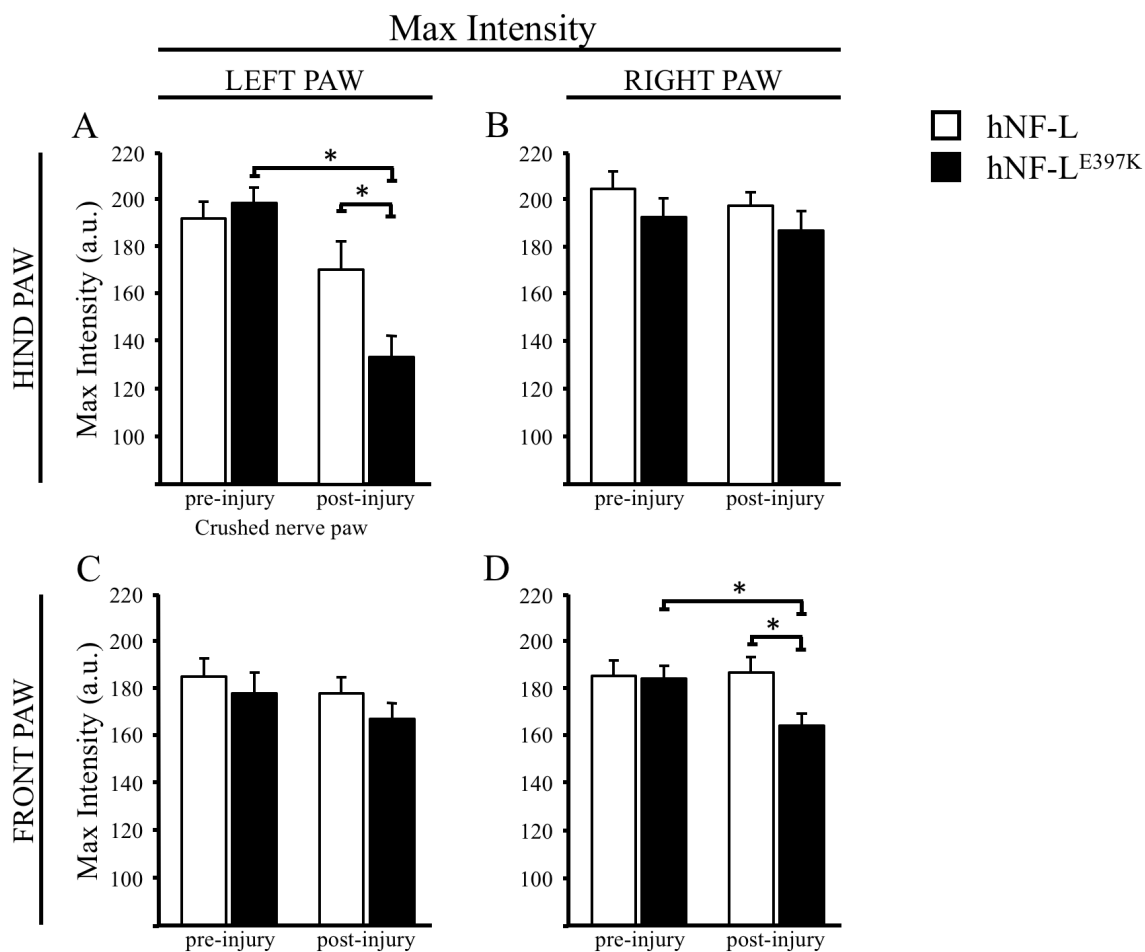


Figure 3.5. Reduced Max Intensity in right front and left hind limbs post-injury.

Max Intensity is a measure of the maximum light intensity of a paw print. Max Intensity correlates with the amount of pressure placed on a paw while the paw is in contact with the glass regardless of the area of contact. Max intensity failed to recover to pre-injury levels in the left hind (A) and right front (D) paws of hNF-L^{E397K} mice. Moreover, hNF-L^{E397K} animals had significantly lower Max Intensity values compared to hNF-L following recovery (A and D). Max Intensity values were unchanged in the right hind (B) and left front (C) paws. The differences in means were analyzed for overall statistical differences using a two-way ANOVA with Holm-Sidak post hoc analysis. *, $P < 0.05$.

Premature phase shift during ambulation after recovery from nerve injury.

A model of a typical step cycle is provided (Fig. 3.6A). In the step cycle (Fig. 3.6A), the Stand phase of ambulation can be separated into braking and propulsion sub-phases (Fig. 3.6B). The point at which the braking sub-phase transitions into the propulsion sub-phase is defined by the maximum contact of a paw. The time it takes for a contacting paw to reach its maximum contact is referred to as Max Contact At (s) (Fig. 3.6B). Max Contact At (%) can be regarded as the point where the braking phase transitions into the propulsion phase during the Stand phase.

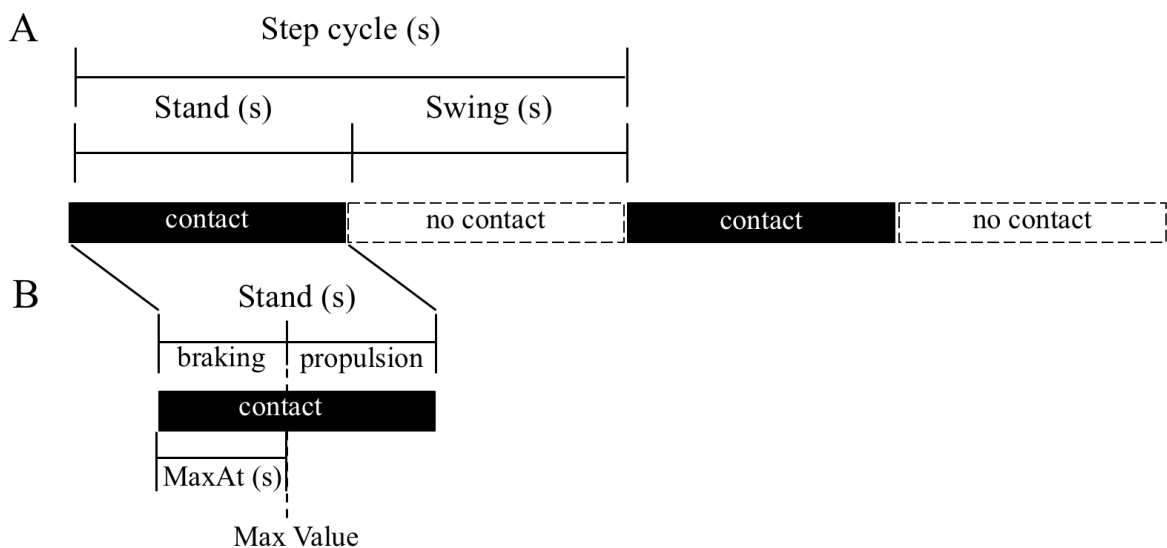


Figure 3.6. Schematic outlining parameters measured by CatWalk. Step cycle of all paws is composed of alternating contacting (black) and non-contacting (white) phases (A). Within a step cycle, the contacting phase is referred to as the stand phase [reported as Stand (s)] and the non-contacting phase is referred to as the swing phase [reported as Swing (s)] (A). Each stand phase contains both a braking phase and propulsion phase. Maximum contact or max value of a paw roughly defines the point at which the braking phase transitions into the propulsion phase. The time it takes a paw to reach the Max Value is reported as Max Intensity At (s). Max Contact At (%) can be regarded as the point where the braking phase transitions into the propulsion phase during the Stand phase (B).

Following recovery, hNF-L Max Contact At (%) returned to pre-injury values (Fig. 3.7A). Interestingly, hNF-L^{E397K} mice Max Contact At (%) values failed to recover to pre-injury values, and recovered less than hNF-L mice (Fig. 3.7A). Max Contact At (%) was not affected on the right hind (Fig. 3.7B) and left front paws (Fig. 3.7C). On the right, front paw, Max Contact At (%) recovered to pre-injury values in hNF-L animals, but not in hNF-L^{E397K} animals (Fig. 3.7D).

Altered Max Contact At (%) in the left hind and right front paws of hNF-L^{E397K} mice can result from either a decreased Stand (s) time or increased Max Contact At (s) time (Fig. 3.6). Therefore, the relative stand (s) and Max Contact At (s) for each paw and time point were examined and revealed no alterations to these metrics (data not shown) suggesting that the decreased Max Contact At (%) values are due to a premature phase shift during the Stand phase.

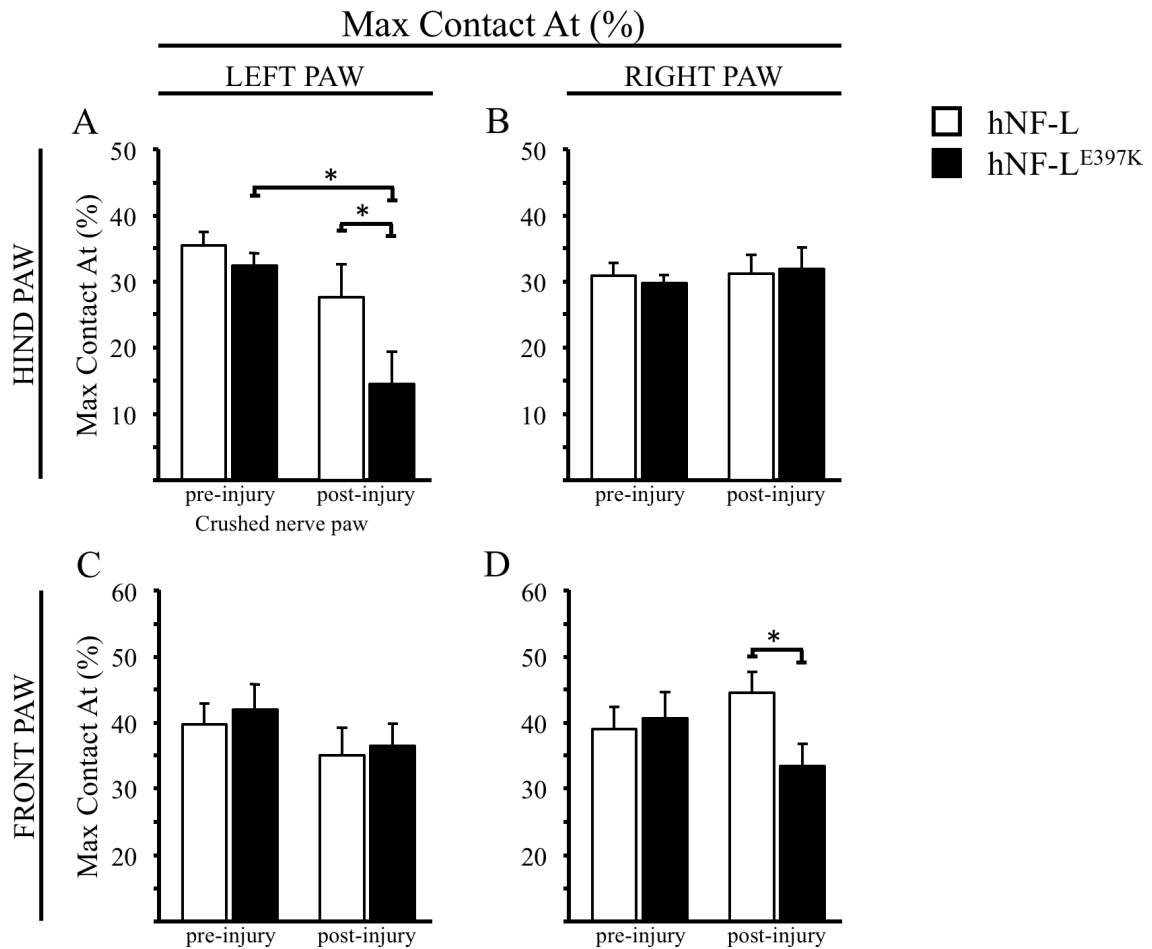


Figure 3.7. Reduced Max Contact At (%) in right front and left hind paws following nerve injury recovery. As Max Contact At (%) is regarded as the point where gait transitions from braking to propulsion, Max Contact At (%) is also a measure of the point within a stand phase where the maximal contact area with the walking surface is reached. hNF-L^{E397K} Max Contact At (%) failed to recover to pre-injury values, and was recovered less than hNF-L controls (A). Max Contact At (%) was not altered on the right hind (B) or left front (C) paws. On the right front paw, hNF-L^{E397K} Max Contact At (%) was significantly reduced compared to hNF-L Max Contact At (%) following recovery (D). The differences in means were analyzed for overall statistical differences using a two-way ANOVA with Holm-Sidak post hoc analysis. *, $P < 0.05$.

Altered interlimb coordination after recovery from nerve injury.

Limb coupling is a measurement of interlimb coordination. Coordinated diagonal limbs (LH→RF, RH→LF) should produce coupling values of ~ 0% as they move synchronously and their paws should be in contact with the glass at the same time. Girdle (LH→RH and LF→RF) and ipsilateral (LH→LF and RF→RH), which move alternatively, should produce coupling values of ~50%. Animals which have uncoordinated limb couplings present values that deviate from these expected percentages (Dale et al., 2012; Kloos et al., 2005).

hNF-L^{E397K} mice displayed significantly altered coordination in the girdle (LH→RH, Fig. 3.8A), ipsilateral (LH→LF, Fig. 3.8B), and diagonal (LH→RF, Fig. 3.8F) limbs following recovery. Interestingly, in hNF-L^{E397K} ipsilateral (RH→RF, Fig. 3.8C), girdle (LF→RF, Fig. 3.8D) and diagonal (RH→LF, Fig. 3.8E) limbs, which do not involve the LH limb, showed no alterations to limb coordination (Fig. 3.8A-F). hNF-L control mice showed no alterations to interlimb coordination. Analysis of alternative coupling patterns showed similar alterations (data not shown). These results indicate that interlimb coordination was significantly altered, and did not return to pre-injury coordination for limb combinations involving the injured limb in the hNF-L^{E397K} mice.

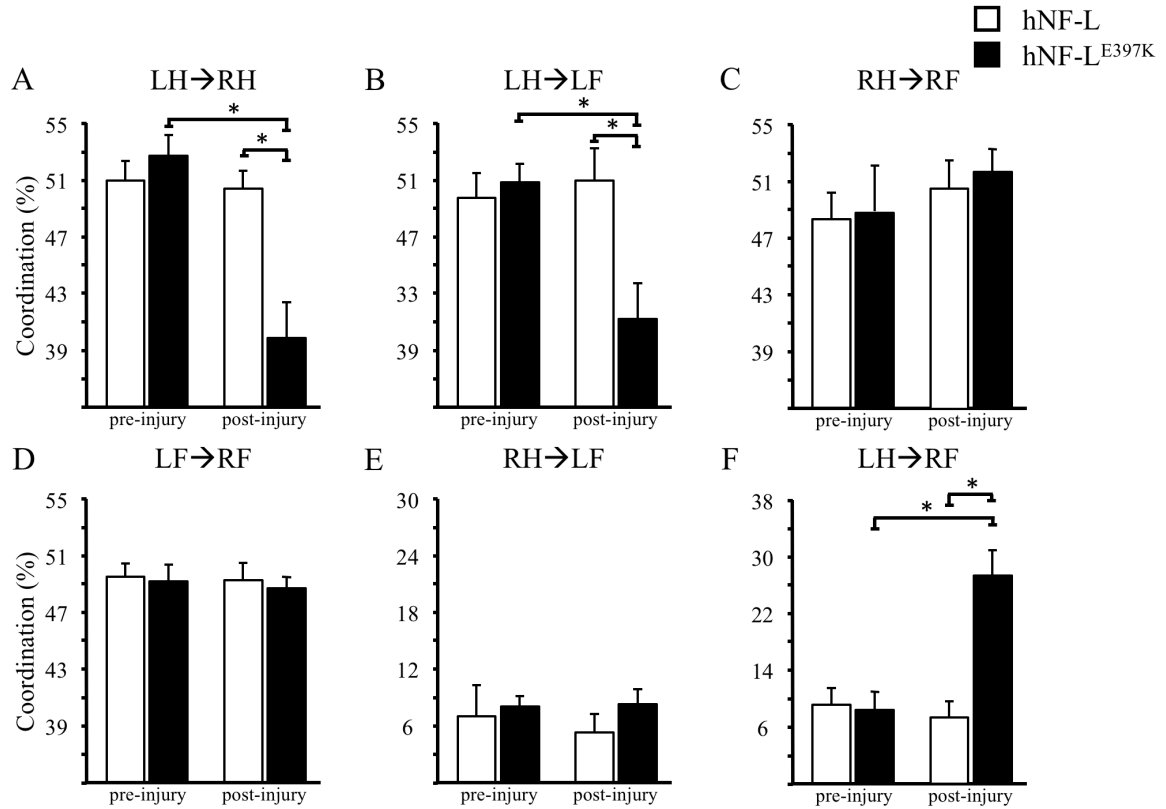


Figure 3.8. Limb coordination in hNF-L^{E397K} mice is altered after recovery from nerve injury. Perfectly coordinated diagonal (LH→RF and RH→LF) limbs have coupling values of ~0, whereas perfectly coordinated girdle (LH→RH and LF→RF) and ipsilateral (LH→LF and RH→RF) limbs have coupling values of ~50. Coordination failed to recover for all coupling values that included the left hind (LH) limb in hNF-L^{E397K} mice relative to pre-injury and hNF-L measurements (A, B and F). Coordination between limbs that did not include the left hind limb was unaffected following recovery (B, C and D). The differences in means were analyzed for overall statistical differences using a two-way ANOVA with Holm-Sidak post hoc analysis. *, $P < 0.05$.

3.5. Discussion.

Evidence suggests that pre-existing neuropathies can be exacerbated by non-toxic dosages of neurotoxic agents and by administration of prescribed drugs (Chaudhry et al., 2003; Hildebrand et al., 2000; Martino et al., 2005). In human patients, exacerbation of neuropathy has been reported to result in muscle weakness in both upper and lower limbs, inability to support weight (Hildebrand et al., 2000), development of pain, and decreased coordination while walking (Chaudhry et al., 2003; Martino et al., 2005). Currently, it is not known whether exacerbation is due to functional or structural alterations to the nerves, thus no current treatments, other than physical therapy, are available (Hildebrand et al., 2000; Weimer and Podwall, 2006). We investigated if CMT2E neuropathy is exacerbated following a nerve challenge. We challenged these mice with a crush to the left sciatic nerve, and analyzed function and gait during (supplemental figures) and after recovery.

Previous analyses of hNF-L^{E397K} animals, by Catwalk, revealed alterations in interlimb coordination in symptomatic animals without alterations to Print Width, Print Length, or Max Contact Area (Dale et al., 2012). During recovery from nerve injury, hNF-L^{E397K} mice developed alterations to Print Width, Print Length, Max Contact Area, and Max Intensity, all of which are indicative of decreased ability to bear weight and mechanical allodynia on the injured paw. Decreased ability to bear weight or increased mechanical allodynia, or a combination of both, could have resulted in the development of a premature phase shift observed during the Stand phase, as indicated by altered Max Contact At (%) values, in hNF-L^{E397K} mice. Development of such alterations ultimately caused disruption to interlimb coordination that were more pronounced than those previously seen in normal (uninjured) hNF-L^{E397K} mice (Dale et al., 2012).

Following a nerve crush injury, nerves degenerate from the day of injury to about 7 days post injury, which is followed by a period of nerve regeneration and re-innervation from 7 to about 20 days post-injury (Gordon and Stein, 1982a; Gordon and Stein, 1982b; Jager et al., 2014; Ronchi et al., 2010). After re-innervation, axons undergo radial growth to regain pre-injury axonal diameters and recover normal nerve conduction velocity (Gordon and Stein, 1982a; Gordon and Stein, 1982b; Sta et al., 2014; Wood et al., 2011). Our functional recovery analyses suggest hFN-L^{E397K} mice recover similar to hNF-L mice up to day 20 post-injury. From day 20 to day 25, hNF-L mice further improve, whereas hNF-L^{E397K} mice do not continue to recover. In some instances, hNF-L^{E397K} recovery declines. This suggests that, following nerve injury, axons of hNF-L^{E397K} animals are able to regenerate and re-innervate their targets similarly to control animals. However, the lack of, or decline in, recovery from day 20 onwards in hNF-L^{E397K} animals suggests possible defects in axonal radial growth. Initial characterization of symptomatic hNF-L^{E397K} mice revealed a reduction nerve conduction velocity and axonal diameters in the motor nerves (Shen et al., 2011). This suggests that a possible mechanism of disease exacerbation following a nerve injury could be the inability of axons to expand radially leading to even further reduced nerve conduction velocities. Further analyses will be required to investigate the molecular mechanisms leading neuropathy exacerbation in our CMT2E mouse model.

Taken together, our results suggest that nerve injury exacerbates CMT2E neuropathy, which manifests as alterations in sensory and motor coordination pathways on the injured limb. This provides a possible new approach for investigating exacerbation of neuropathies in patients suffering from a peripheral neuropathy. Furthermore, our data

suggests that hNF-L^{E397K} mice may be a useful model for developing and screening potential therapies for treating or preventing disease exacerbation. Given that neuronal recovery is altered, hNF-L^{E397K} mice may also provide valuable insight into potential neurological toxicity of new and existing compounds.

CHAPTER 4

SCHWANN CELL ELONGATION DURING MYELINATION AND REMYELINATION IS RESTRICTED BY NEUROFILAMENT MEDIUM PHOSPHORYLATION LEADING TO REDUCED INTERNODE LENGTH.

(This work was submitted for publication to *Acta Neuropathologica* and is under review)

Eric Villalón^{1,2,*}, Devin M. Barry^{3,*}, Nathan Byers⁶, Maria R. Jones^{1,2}, Dan S. Landayan⁴,
Jeffrey M. Dale^{1,2}, Natalie L. Downer⁷, Nigel A. Calcutt⁵, Michael L. Garcia^{1,2,†}

¹Department of Biological Sciences, ²C.S. Bond Life Sciences Center, University of Missouri, Columbia, MO 65211, ³Department of Anesthesiology, Center for the Study of Itch, Washington University School of Medicine, St. Louis, MO 63110, ⁴Department of Quantitative and Systems Biology, University of California Merced, Merced, CA 95343, and ⁵Department of Pathology, University of California San Diego, La Jolla, CA 92093, ⁶Department of Biomedical Sciences, Colorado State University, Fort Collins, CO 80523, ⁷Department of Biology, Truman State University, Kirksville, MO 63501.

Keywords: Nerve injury, Remyelination, Reduced nerve conduction, Axon, Neurofilaments

4.1. Abstract.

The distance between nodes of Ranvier, referred to as internode length, positively correlates with axon diameter, and is optimized during development to ensure maximal neuronal conduction velocity. Following myelin loss, internode length is reestablished through remyelination. However, remyelination results in short internode lengths and reduced conduction rates. We analyzed the potential role of neurofilament phosphorylation in regulating internode length during remyelination and myelination. Following ethidium bromide induced demyelination, levels of neurofilament medium (NF-M) and heavy (NF-H) phosphorylation were unaffected. Preventing NF-M lysine-serine-proline (KSP) repeat phosphorylation increased internode length by 30% after remyelination. To further analyze the role of NF-M phosphorylation in regulating internode length, gene replacement was used to produce mice in which all KSP serine residues were replaced with glutamate to mimic constitutive phosphorylation. Mimicking constitutive KSP phosphorylation reduced internode length by 16% during myelination and motor nerve conduction velocity by ~27% without altering sensory nerve structure or function. Our results suggest that NF-M KSP phosphorylation is a negative regulator of Schwann cell elongation, and suggest motor and sensory axons utilize different mechanisms to establish internode length.

4.2. Introduction.

Postnatal development of peripheral nerves requires myelination and establishment of axonal diameter, which are required for rapid impulse transmission. Myelination includes formation of compact myelin and bidirectional elongation of myelinating Schwann cells along axons (Sherman and Brophy, 2005). While insights into the formation of compact myelin have been made, comparatively little is known about Schwann cell elongation. During development there are two periods of Schwann cell elongation that establish internode length. The first period occurs during initial myelination from post-natal day 1 to approximately 14 days later, when myelination is complete (Webster, 1971). The initial period of elongation clusters ion channels (Dugandzija-Novakovic et al., 1995; Schafer et al., 2006; Vabnick et al., 1996) and establishes optimal internode length to maximize neuronal conduction velocity (Goldman and Albus, 1968; Hardy, 1971; Huxley and Stampfli, 1949). After initial establishment of internode length, Schwann cells continue to elongate during normal developmental growth to maintain optimal internode length and maximal conduction velocity (Bunge et al., 1989; Simpson et al., 2013; Vizoso, 1950).

A positive correlation between internode length and axon diameter was established over 140 years ago (Key and Retzius, 1875) such that larger diameter axons have longer internodes. Radial growth establishes axon diameter, and is dependent upon myelination (de Waegh et al., 1992). Myelination induces radial growth, so myelinated regions of an axon have larger diameters compared to unmyelinated regions of the same axon (nodes of Ranvier) (Yin et al., 1998). Moreover, increases in axonal diameter correlate with neurofilament (NF) number (Friede and Samorajski, 1970), which are the

main cytoskeletal proteins of myelinated axons (Perrot et al., 2008). NF composition varies with developmental stage (Shaw and Weber, 1982; Shen et al., 2010) and within central versus peripheral nervous systems (Yuan et al., 2006; Yuan et al., 2012). However, all NFs are composed of a common core of three subunits proteins neurofilament Light (NF-L), Medium (NF-M), and Heavy (NF-H), (Jones et al., 2016). Upon myelination (de Waegh et al., 1992; Yin et al., 1998), NF-H and NF-M become phosphorylated on C-terminal lysine-serine-proline (KSP) repeats. Thus, Schwann cell elongation, radial axonal growth, and NF KSP phosphorylation occur in parallel during postnatal development.

After nerve injury, the positive correlation between internode length and axon diameter is lost (Hildebrand et al., 1985; Vizoso and Young, 1948). Remyelination results in uniformly short internodes (Hildebrand et al., 1987; Sanders and Whitteridge, 1946; Vizoso and Young, 1948) resulting in reduced conduction velocity (Court et al., 2004). Loss of myelin also reverts several axonal properties to a pre-myelin phenotype. Sodium channels, normally clustered within nodes of Ranvier become diffusely localized within the axonal plasma membrane after myelin loss (Boiko et al., 2001; Waxman et al., 2004). Demyelination results in re-expression of $Na_v1.2$ a subunit of voltage sensitive sodium channels (Craner et al., 2004; Schafer et al., 2006) and suppression of $Na_v1.6$ (Craner et al., 2004; Schafer et al., 2006), which is the predominant a subunit of myelinated peripheral nerves (Boiko et al., 2001; Schafer et al., 2006; Vabnick et al., 1996). However, one axonal property that does not revert to a pre-myelination phenotype is the phosphorylation status of NF proteins (Arroyo et al., 2004; Cole et al., 1994). To revert back to a pre-myelination phenotype, NF-M and NF-H would need to be

dephosphorylated during demyelination. The significance of maintaining NF-M and NF-H phosphorylation is unknown as the role of NF-M and NF-H KSP phosphorylation is unclear (Garcia et al., 2009).

In this study, we demonstrate that NF-M KSP phosphorylation regulates internode length during remyelination and myelination. Preventing NF-M KSP phosphorylation resulted in formation of longer internodes during remyelination. Mimicking constitutive NF-M KSP phosphorylation during myelination reduced internode length. These results provide the first mechanistic insights into reduced internode length that occurs with remyelination.

4.3. Experimental procedures.

Animals.

Mice were housed in microisolator cages on a 12-h light/dark cycle, and were given food and water ad libitum. All procedures were in compliance with the University of Missouri and University of California San Diego Animal Care and Use Committees and with all local and federal laws governing the humane treatment of animals.

Nerve demyelination by Ethidium bromide injection.

Mice were placed under isoflurane anesthesia and the left sciatic nerve was exposed via an incision in the flank followed by separation of underlying musculature by blunt dissection. Utilizing pulled microcapillary needles 2 μ L of 0.1% ethidium bromide in normal saline was injected into the middle third of the exposed sciatic nerve to induce demyelination. The mice were allowed to recover and placed back in their cage. Successful injection of 2 μ L of 0.1% ethidium bromide into the sciatic nerve was confirmed by a change in color of the nerve compared to the uninjected and saline injected controls. Seven days after injection, the animals injected with ethidium bromide displayed loss of function of the injected nerve, which is consistent with affected nerve function after an injury (Villalon et al., 2015). Furthermore, gross examination of the nerves at 7 days post-injected showed inflammation and discoloration of the ethidium bromide injected nerve, consistent with nerve demyelination. Sciatic nerves were collected for analysis at three different time points; maximal demyelination point, at 7 days post-injection; beginning of remyelination, 14 days post-injection; and complete remyelination point, 30 days post-injection (Bondan et al., 2009; Bondan and Monteiro

Martins Mde, 2013; Riet-Correa et al., 2002).

Detection and quantification of NF proteins by immunoblotting.

Sciatic nerves (demyelination experiments) and L5 motor and sensory roots were harvested and snap frozen in liquid nitrogen or were homogenized immediately. Tissues were homogenized on ice in a buffer containing 50 mM Tris, pH 7.5, 0.5 mM EDTA, pH 8, and protease inhibitors were added according to manufacturer's instructions. (Complete Mini, Roche, Mannheim, Germany). An equal volume of lysis buffer containing 50 mM Tris, pH 7.5, 150 mM NaCl, 1% NP-40, 1% sodium deoxycholate, and 2% SDS was added. The homogenates were sonicated for 10 seconds 2X, then boiled for 10 minutes in a sand bath, and clarified by centrifugation at 16,000 g for 10 minutes. Protein concentration was determined using the Bio-Rad Protein Assay kit (Bio-Rad, Hercules, CA, USA). Protein extracts were resolved on 7.5% SDS-polyacrylamide gels and transferred onto nitrocellulose membrane or stained with Coomassie-blue. NF-L (CPCA-NF-L, EnCor Biotechnology, Gainesville, FL, USA), NF-M (CPCA-NF-M, EnCor Biotechnology, Gainesville, FL, USA) and NF-H (CPCA-NF-H, EnCor Biotechnology) were identified with polyclonal antibodies. Phosphorylated NF-H and NF-M were identified using a mouse monoclonal antibody that recognizes the protein in a phospho-dependent manner (SMI-31, Covance, Emeryville, CA, USA). Mouse and chicken primary antibodies were detected with donkey anti-mouse and goat anti-chicken secondary antibodies conjugated to IRdye-700X® infrared fluorophores (Rockland, Gilbertsville, PA, USA) respectively. Immunoreactive bands were visualized by infrared detection with an Odyssey image scanner (LICOR Biosciences, Lincoln, NE, USA). Quantification of immunoblots was performed by the relative optical density (ROD) method.

Absolute intensities of the immunoreactive bands were obtained using Photoshop (Adobe Systems Inc.) and RODs were calculated in the following manner: $[(NF \text{ protein mean intensity} - \text{background mean intensity}) * (\text{number of pixels})] / [(\text{loading control band mean intensity} - \text{background intensity}) * (\text{number of pixels})]$. Optical densities of immunoreactive bands were calculated as follows: $[(\text{absolute intensity} - \text{background intensity}) * (\text{number of pixels})]$ Average optical densities for each genotype were calculated and compared to the wild type averages, which were arbitrarily set to a value of 1. All optical densities were analyzed for statistical significance by one-way ANOVA with Holm-Sidak *post hoc* analysis for pair wise comparisons or by a Student's *t*-test (SigmaPlot, Systat Software).

Teased fiber analysis.

Mice were sacrificed and the sciatic nerve was exposed by blunt dissection (for demyelination experiments) and immediately extracted and processed as subsequently described. For L5 root teased fibers experiments, the mice were transcardially perfused with 0.1M PBS, pH 7.4 for no more than 5 minutes. The L5 root was dissected. The dorsal root was shortened relative to the ventral root for easy identification. In all cases the nerves or roots were submersion fixed in a 2.5M glutaraldehyde, 0.025M sodium cacodylate, pH 7.38 solution for 25 min at 4°C. The nerves or roots were then rinsed in 1X PBS for 5 minutes and transferred to a saturated solution of Sudan black in 70% ethanol and allowed to incubate for 1 hr at room temperature. The samples were then rinsed twice in 70% ethanol for 5 min and transferred to a 10% glycerin solution. Fifty to one hundred axon bundles were separated from the ventral root and the tibial branch of the sciatic nerve. The bundle was transferred to a super frost microscope slide containing a thin layer of a 10% aqueous solution of glycerin:

BSA (1:1). Individual fibers were teased apart from the bundle and laid out on the glass slide. Fibers were then allowed to dry over night on a 50°C hot plate. Digital photos of the fibers were taken using the AxioVision Digital Image Processing Software (Carl Zeiss MicroImaging). Internode lengths were measured using ImageJ (NIH). At least 200 internodes were measured from each tissue sample and at least 3 animals were used per genotype and treatment. An average of the internode lengths for each genotype was calculated and used for statistical analyses. The data was analyzed for variability using the SAS analytics software (SAS Institute Inc.). Possible influential outliers were calculated using a CooksD test and the data was analyzed for statistical significance using one-way nested ANOVA.

Site directed mutagenesis and construction of NF-M^{S→E} mice by gene replacement.

A genomic clone isolated from mouse 129 SVJ library was used for construction of NF-M^{S→E} [a generous gift from J. P. Julien]. A ~1.1 kb *AccI/BclI* fragment, containing all KSP repeats, was subcloned into pBluescript KS. Five oligonucleotides were designed to convert the phosphorylated KSP serine residues to glutamate (Fig. 4.1A) using a PCR approach as previously described (Garcia et al., 2009). DNA sequence analysis confirmed the substitution of the 7 serine codons with glutamate codons without the introduction of additional sequence changes (data not shown). The modified NF-M fragment was recloned back into the *nefm* gene. *Nefm* 5' UTR and 3' UTR regions were amplified from mouse 129SvEv genomic DNA to increase homology from 5 kb to a total of 8 kb. Diphtheria toxin alpha gene with poly adenylation (DT-ApA) clone was a generous gift from Y. Yanagawa and T. Yagi (Yanagawa et al., 1999). DT-ApA was introduced at the

3' end of the construct as a negative selection marker. Finally, the *nefl* 3' UTR and a PKG Neo cassette were cloned at the 3' end of *nefm* exon 3 (inserted at the *SaII* and *MluI* sites, which were cloned into the *nefm* 3' UTR using a linker) (Fig. 4.1B). The targeting construct was linearized with *AatII* and electroporated into mouse 129SvEv ES cells (Millipore Corporation) by the MU Transgenic Core and selected with G418 at 250µg/ml (Joyner, 1994). Drug resistant colonies were amplified and screened by PCR at the 3' end and by Southern Blot at the 5' end. DNA sequence analysis (MU DNA Core) was used to ensure incorporation of the *nefm*^{S→E} exon 3. Four out of the 192 ES clones were identified to have undergone homologous recombination at both the 5' and 3' ends of the gene to produce the NF-M^{S→E} targeted allele. One of the positive ES cell clones was injected into mouse C57Bl6 blastocysts, and the MU Transgenic Core implanted blastocysts into the uteri of pseudo-pregnant surrogates. Six chimeric male mice were identified from the surrogates. Germ line transmission of the NF-M^{S→E} allele was confirmed by PCR amplification of genomic DNA purified from tail biopsies using Invitrogen Taq (Clontech Laboratories, Inc., A Takara Bio Company, Madison, WI, USA) with the following primers: NF-M Exon 3 Forward- 5'TGCAGAGGGAGAAGAAAGGAGAGGA3', NF-M 3'UTR Reverse Primer- 5'AACTGGCGAATCCCTAGGTACAT3', NF-L 3'UTR Reverse Primer- 5'GTTGACCTGATTGGGGAGAA3'. Mice of either sex were bred to homozygosity and wild type littermates were used as controls (Fig. 4.1C).

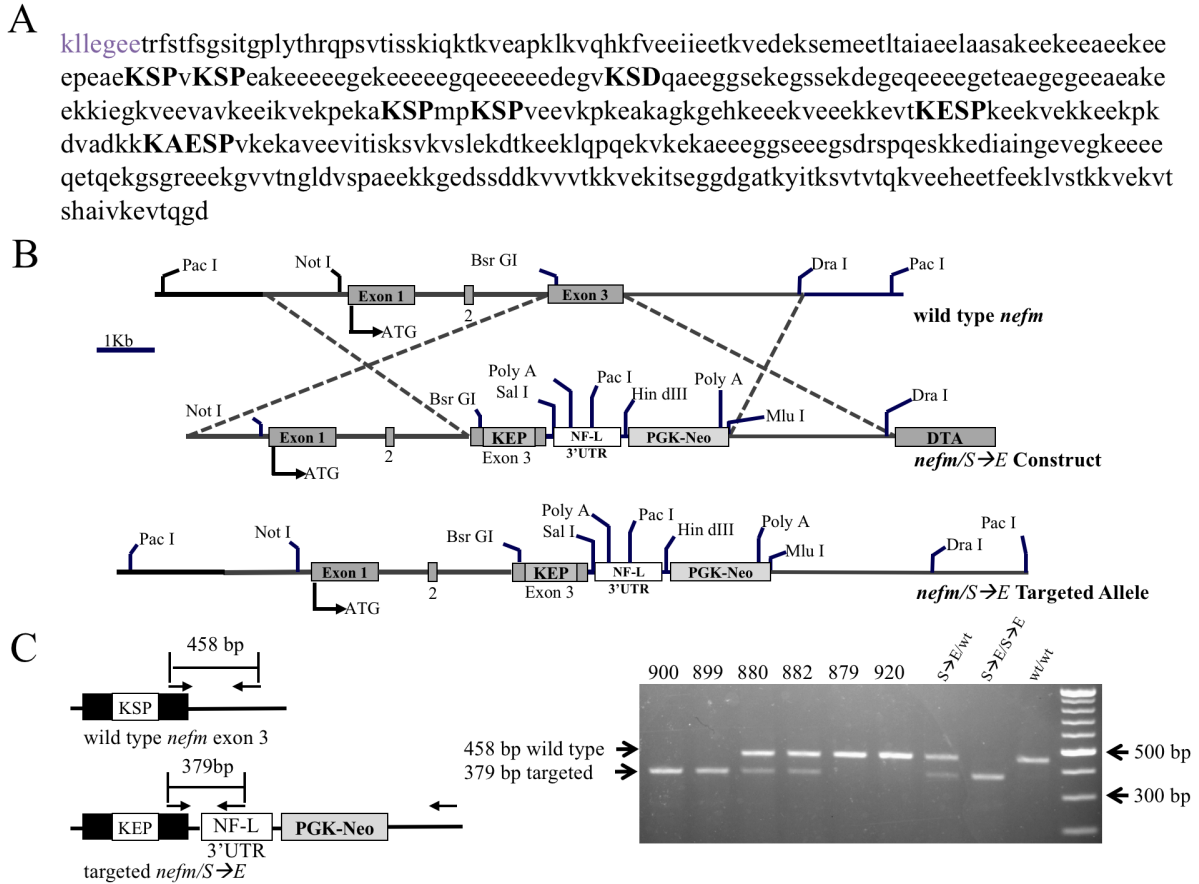


Figure 4.1. Generation of a constitutively phosphorylated NF-M protein. (A) Murine NF-M C-terminus domain. The conserved “KLLEGEE” (in bold) sequence marked the end of the rod domain in all three neurofilament subunits. All the KSP, KXSP, KXXSP and the variant KSD were highlighted in bold, uppercase letters. Murine NF-M NCBI accession number NP_032717. (B) Construction of the NF-M^{S→E} allele in which the serine residues of the highly conserved KSP repeats were substituted with glutamate residues. The three filled boxes indicated the three NF-M exons separated by two introns. ATG indicated the translation initiation codon. Dotted lines identified regions where homologous recombination could occur between the targeting vector and the endogenous gene. (C) Mouse genomic DNA was screened for targeting of the NF-M^{S→E} allele using three primers for genotyping. Left, schematic of the NF-M endogenous and NF-M^{S→E} alleles identified approximate locations for primer annealing sites and predicted sizes of amplified regions. Right, PCR amplification of genomic DNA from mouse-tail biopsies with both the endogenous and targeted alleles identified.

Nerve conduction velocity measurements.

Nerve conduction velocities were measured in the sciatic nerve, interosseus muscle system of 6-month-old as previously described (Jolivald et al., 2009). In brief, mice were anesthetized with halothane (4% in O₂ for induction, 2-3% for maintenance) with body temperature maintained at 37 °C by a heating lamp and thermal pad connected to a temperature regulator and a rectal thermistor probe. The sciatic nerve was stimulated with single supramaximal square wave pulses (4-8 V and 0.05 ms duration) via fine needle electrodes placed at the sciatic notch and Achilles tendon. Evoked early (M waves) and late (H waves) responses were recorded from the interosseus muscles of the ipsilateral foot via two fine needle electrodes and displayed on a digital storage oscilloscope. The distance between the two sites of stimulation was measured using calipers, and motor sciatic nerve conduction velocity was calculated using the M wave response and sensory sciatic nerve conduction velocity using the H wave response as previously described (Jolivald et al., 2009). Measurements were made in triplicate from a minimum of six animals per genotype, and the median was used as the measure of velocity. Values were compared for overall statistical significance by a Student's *t*-test (InStat, GraphPad Software, la Jolla, CA, USA).

Tissue preparation for axon morphometry.

Mice were euthanized and perfused transcardially with a fixative solution of 2.5% glutaraldehyde, 4% paraformaldehyde in 0.1 M cacodylate buffer, pH 7.2, and post-fixed overnight in the same buffer. Fifth lumbar nerve roots were dissected, treated with 2% osmium tetroxide, washed, dehydrated, and embedded in Epon-Araldite resin. Thick sections

(0.75 μm) for light microscopy were stained with ρ -phenylenediamine. Images of transverse sections of L5 motor axons were collected with a Zeiss Axio Imager A1 light microscope (Carl Zeiss MicroImaging GmbH, Jena, Germany) and analyzed in at least five mice per genotype and age group. Entire roots were imaged, imaging thresholds were selected individually, and the cross-sectional area of each axon was calculated and reported as a diameter of a circle of equivalent area using the AxioVision Digital Image Processing Software (Carl Zeiss MicroImaging). The total number of axons was analyzed for statistical significance by a two-way ANOVA (SigmaPlot, Systat Software, Inc.). Axonal diameters were grouped into 0.5 μm bins. Diameter distributions for 2-month-old motor axons were analyzed for overall statistical significance by a Mann-Whitney U test. Diameter distributions for 6-month-old motor and 2 and 6-month-old sensory axons were analyzed for statistical significance by a two-way ANOVA. G-ratios were calculated by measuring the axonal diameter and fiber diameter of individual axons for at least 10% of all axons per motor root using AxioVision Digital Image Processing Software (Carl Zeiss Micro imaging). G-ratios were analyzed for statistical significance by a Student's t -test (SigmaPlot, Systat Software, Inc.).

Balance beam.

Mice were trained 5 days to walk on three progressively smaller circular wooden beams (5, 2.5 and 1cm diameter) 120 cm in length, suspended 50 cm from a bedding surface. During training, mice walked on each of the three beams for 3 minutes with at least 20 minutes of rest. After training, experiments were performed on the smallest beam, which was marked in 5 cm increments. Mice walking on the beam were recorded using a digital

camera for three trials per day for three consecutive days (9 total trials) with at least 20 minutes of rest between trials. Trials were recorded from two camera angles, parallel to the beam (6 trials) and perpendicular to the beam (3 trials). The number of falls, number of foot slips, total time walking, and the latency to fall within the 3-minute trials were scored from all 9 trials recorded. A fall was considered any event when the mouse fell off the beam, hanging under the beam was not considered a fall. Foot slips were events when the hind limbs of the mouse slipped off the surface of the beam. The total amount of time spent walking was measured from the beginning of a walking event to the end of that walking event. The total time walking per trial was calculated by adding the time of all individual walking events within a trial and it was used to normalize the number of falls and foot slips. Falling latency was calculated by measuring the time the mouse spent walking before each fall, therefore only mice that fell were included in this measurement. Average distance walked was calculated from the three perpendicular angle videos by using the 5 cm increment marks. To calculate the average walking speed, the time spent walking in the three perpendicular angle videos was also measured and together with the average distance walked was used to calculate the average velocity. The reported average time walked was also measured only from the three perpendicular angle videos. Averages of all observations were calculated for each genotype and analyzed for statistical significance by a Student's *t*-test.

Thermal algesia response latency.

Latency response to noxious heat stimulus was measured as previously described (Calcutt, 2004). In brief, mice were placed on the warmed glass top surface of the testing apparatus

and allowed to acclimate for 30 min. A mobile heating source was placed under the center of the hind paws and turned on. Turning on the heating source activated a timer and the heating source that locally heated the glass surface. When the animal responded to the stimulus by withdrawing its paw, movement sensors stopped the timer and the heating source. The time to response was recorded. Four measurements were taken for each paw with at least 5 min of rest between measurements. Both hind paws were tested and the average response time of both paws was used to calculate an average response for each mouse. Average response time across genotypes was analyzed for statistical significance by a Student's *t*-test.

Tactile algesia response threshold.

Threshold response to tactile algesia was measured with a Dynamic Plantar Aesthesiometer (DPA) model # 37450 (Ugo Basile, Italy). Mice were set on a wire-mesh platform and allowed to habituate for at least 15 min. After habituation, the DPA monitored paw withdrawal thresholds of the hind and front paws. A metal filament was pushed against the hind and front paws with an ascending linear force (10 g/s and 2 g/s, respectively) until a strong, immediate withdrawal occurred. Measurements were taken in triplicate and averages were reported as paw withdrawal thresholds in grams. Averages for each paw were analyzed for statistical significance by a Student's *t*-test.

4.4. Results.

Neurofilament heavy and medium subunits remained phosphorylated through remyelination.

Injection of ethidium bromide (EtBr) into sciatic nerves of wild type mice induced demyelination, and subsequent remyelination resulted in a 75% reduction in internode length at 30 days post injection (Fig 4.2). We utilized EtBr injections to analyze NF protein and phosphorylation levels at 7, 14 and 30 days post-EtBr injections. Sciatic nerve protein homogenates were resolved on 4% - 12% gradient SDS-PAGE gels. Myelin basic protein (MBP) levels were analyzed as a measure of myelination in control (C), saline injected (S) and EtBr injected (I) sciatic nerves (Fig. 1A and 1B). No differences were apparent between C and S controls (Fig. 4.3A). Immunoblots followed by relative optical density (ROD) analysis revealed reduced MBP levels beginning at day 7 and continuing throughout the time course ($p < 0.001$ at 7 and 14 days) with MBP levels beginning to recover by day 30 ($p = 0.005$) (Fig. 4.3B). Immunoblot and ROD analysis of neurofilament levels suggested an early decrease in all subunits ($p < 0.001$ for NF-L, $p = 0.015$ for NF-M, and $p = 0.004$ for NF-H) (Fig. 4.3C, 4.3D and 4.3F). Neurofilament light (NF-L) ($p < 0.001$) and medium (NF-M) ($p < 0.043$) remained reduced 14 days post-injection while neurofilament heavy (NF-H) recovered to pre-injection levels. By 30 days, NF-L and NF-M levels recovered to pre-injection levels, and NF-H levels were once again decreased ($p = 0.008$). Analysis of NF-H and NF-M phosphorylation levels suggested that the phosphorylation status of both subunits was unaltered during remyelination (Fig. 4.3E and 4.3G).

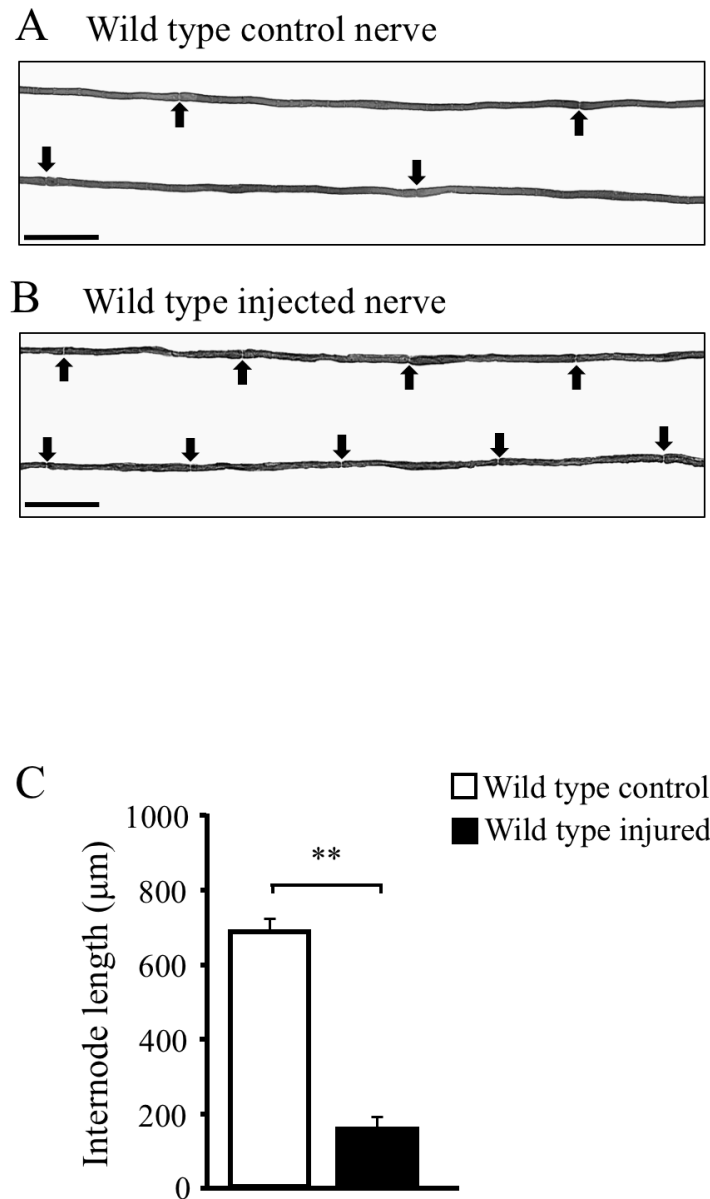


Figure 4.2. Ethidium Bromide demyelination results in drastically reduced internode length. (A and B) Sudan black stained teased fibers of control (A) and injected (B) sciatic nerve fibers at 30 days post-injection. Black arrows point to the approximate location of nodes of Ranvier. (C) Quantification of internode length revealed a significant decrease of ~75% in internode length following remyelination. Internode length measurements were analyzed for statistical significance by a one-way nested ANOVA. Error bars = SEM. N = 5. Black arrow = Node of Ranvier. Scale bars = 100μm.

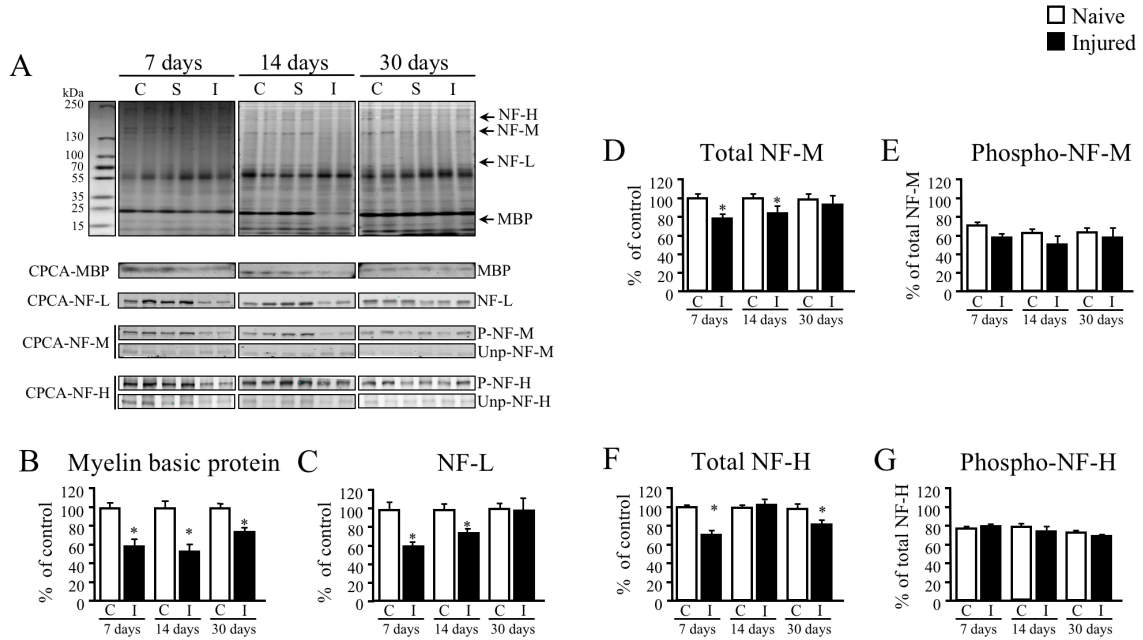


Figure 4.3. Neurofilament phosphorylation levels were maintained during remyelination. (A) Sciatic nerve protein extract from 7, 14, and 30 days post ethidium bromide (EtBr) injections were resolved on 4% - 12% gradient SDS-PAGE gels and stained with Coomassie blue. RODs suggested decreases in myelin basic protein (MBP) at 7 and 14 days post-injection that slightly recovered by 30 days post-injection (B). Total NF-L (C) and NF-M (D) levels were decreased 7 and 14 days post-injection recovering to control levels by 30 days. Total NF-H was decreased 7 and 30 days post-injection (F). Phosphorylated NF-M (E) and NF-H (G) levels were not different at any time point. ROD analyses were analyzed for statistical significance by a two-way ANOVA followed by Holm Sidak *post-hoc* test. Internode length measurements were analyzed for statistical significance by a one-way nested ANOVA. Error bars = SEM. N = 5. C, uninjected control. S, saline injected control. I, ethidium bromide injected. Black arrow = Node of Ranvier. Scale bars = 100 μ m.

Preventing NF-M KSP repeat phosphorylation increased internode length following remyelination.

Internode length positively correlates with axonal diameter (Key and Retzius, 1875), and we have previously reported that axonal diameter is determined by the length of NF-M C-terminus (Barry et al., 2012). We, therefore, focused our analysis on NF-M for the remainder of the study. NF-M phosphorylation occurs upon formation of compact myelin (de Waegh et al., 1992; Yin et al., 1998). Thus, Schwann cell elongation during myelination occurs when NF-M KSP repeats are not fully phosphorylated (de Waegh et al., 1992; Yin et al., 1998). To determine if NF-M KSP phosphorylation could influence Schwann cell elongation, we analyzed internode length following remyelination in a mouse model in which NF-M C-terminus cannot be phosphorylated (referred to as NF-M^{ΔTail}) (Garcia et al., 2003; Rao et al., 2003). Axons were teased from sciatic nerve of uninjected wild type and NF-M^{ΔTail} mice (Fig. 4.4A) at 30 days post-injection of EtBr (Fig. 4.4B). Remyelination resulted in reduced internode length from both wild type ($p < 0.001$) and NF-M^{ΔTail} ($p < 0.001$) mice relative to their uninjected controls. However, remyelination in NF-M^{ΔTail} mice resulted in internode lengths that were significantly ($p = 0.039$) longer (30%) than those of remyelinated wild type nerves (Fig. 4.4C). Analysis of Schwann cell number needed to myelinate a 1 cm axonal segment showed that after remyelination both wild type ($p < 0.001$) and NF-M^{ΔTail} ($p < 0.001$) nerves required significantly more Schwann cells/cm relative to uninjured controls (Fig. 4.4D). Supportive of longer internodes NF-M^{ΔTail} remyelinated nerves required ~20% ($p = 0.003$) fewer Schwann cells/cm than wild type remyelinated nerves (~ 44 Schwann cells/cm vs. 54 Schwann cells/cm, respectively) (Fig. 4.4D). Taken together these data

suggest that preventing NF-M KSP phosphorylation enhanced Schwann cell elongation during remyelination resulting in increased internode lengths.

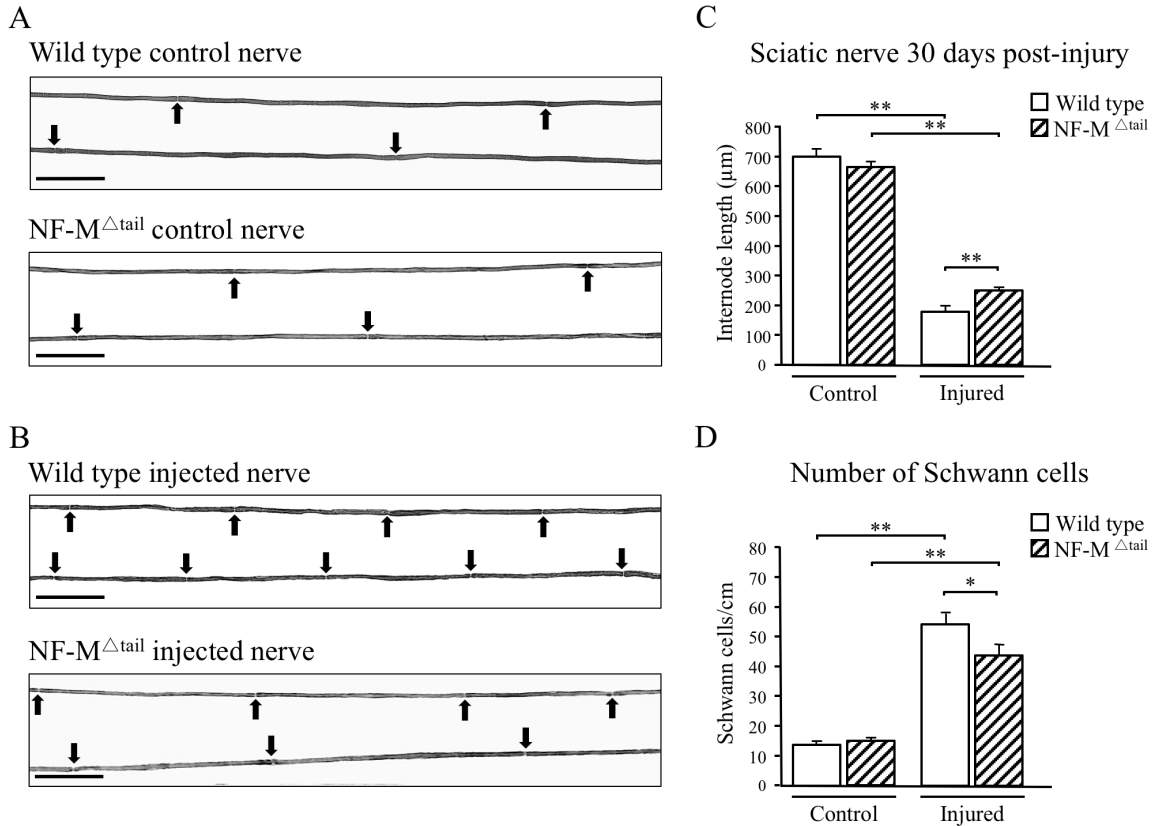


Figure 4.4. Preventing NF-M KSP phosphorylation increased internode length after remyelination. (A) Thirty days post-injection revealed no apparent difference in internode length between uninjected wild type (top) and NF-M Δ Tail controls (bottom). (B) Thirty days post-injection internode length was reduced in both wild type (top) and NF-M Δ Tail mice (bottom) relative to uninjected controls. (C) Quantification of internode length revealed the expected decrease in internode length between control and injected nerves at 30 days post-injection. However, internode length was \sim 30% longer in NF-M Δ Tail nerves. (D) The number of Schwann cell required to myelinate a 1cm long axon segment was increased in both injected wild type and NF-M Δ Tail nerves. Consistent with longer internode length injected NF-M Δ Tail nerves required \sim 20% fewer Schwann cells to myelinate the same axonal length. Averages per group were obtained and analyzed for statistical significance by a two-way ANOVA followed by a Holm Sidak *post-hoc* analysis. Error bars = SEM. $N \geq 4$. Black arrow = node of Ranvier. Scale bar = 100 μ m.

Expressing NF-M^{S→E} did not alter the electrophoretic mobility of NF-M or neurofilament subunit stoichiometry in sciatic nerve.

To further test our hypothesis that NF-M KSP phosphorylation influences internode length, we generated a new line of genetically modified mice expressing NF-M in which all 7 KSP serine residues were replaced with glutamate (S→E) to mimic constitutive KSP phosphorylation (NF-M^{S→E}). Analysis of phospho-KSP-incompetent NF-M (referred to as NF-M^{S→A}) mice revealed that preventing phosphorylation of NF-M KSP repeats increased the mobility of NF-M^{S→A} relative to wild type NF-M (Garcia et al., 2009). Upon SDS-PAGE fractionation, coomassie blue staining revealed that NF-M^{S→E} migrated at the same apparent molecular weight as wild type NF-M in tissue taken from mice at 2 (Fig. 4.5A) and 6 months (Fig. 4.5D) of age. Immunoblotting with an antibody specific to the KE region (Harris et al., 1991) of NF-M C-terminus confirmed the identical electrophoretic mobilities of the wild type and NF-M^{S→E} proteins. ROD analysis of immunoblotting with subunit specific antibodies suggested similar levels of all neurofilament subunit proteins at 2 (Fig. 4.5B and 4.5C) and 6 months (Fig. 4.5E and 4.5F). No statistical differences were found in subunit expression at either time point following statistical analysis of RODs by one-way ANOVA followed by a Holm-Sidak *post hoc* analysis for pair wise comparisons.

Expressing NF-M^{S→E} increased NF-H phosphorylation in young mice but not in older mice.

Preventing NF-M phosphorylation by C-terminal truncation (Garcia et al., 2003) or replacing KSP serine residues with alanines (Garcia et al., 2009) resulted in a compensatory increase in NF-H phosphorylation. To determine if mimicking constitutive phosphorylation of NF-M alters phosphorylation status of NF-H, a monoclonal antibody that detected phosphorylated NF epitopes was used to measure NF phosphorylation (Fig. 4.5G and 4.5I). SMI-31 reacted with phosphorylated NF-H at 2 (Fig. 4.5G) and 6 months (Fig. 4.5I) of age. At 2 months, ROD analysis suggested a significant ($p < 0.05$) increase in phosphorylation levels of NF-H in NF-M^{S→E/S→E} mice compared to wild type (Fig. 4.5H). However, by 6 months, NF-H phosphorylation levels were similar in NF-M^{S→E/S→E} and NF-M^{wt/wt} (Fig. 4.5J). These data suggested that expressing NF-M^{S→E} did not result in overall compensatory increases in NF-H phosphorylation in older mice. Statistical analyses were done by one-way ANOVA followed by a Holm-Sidak *post hoc* analysis for pairwise comparisons.

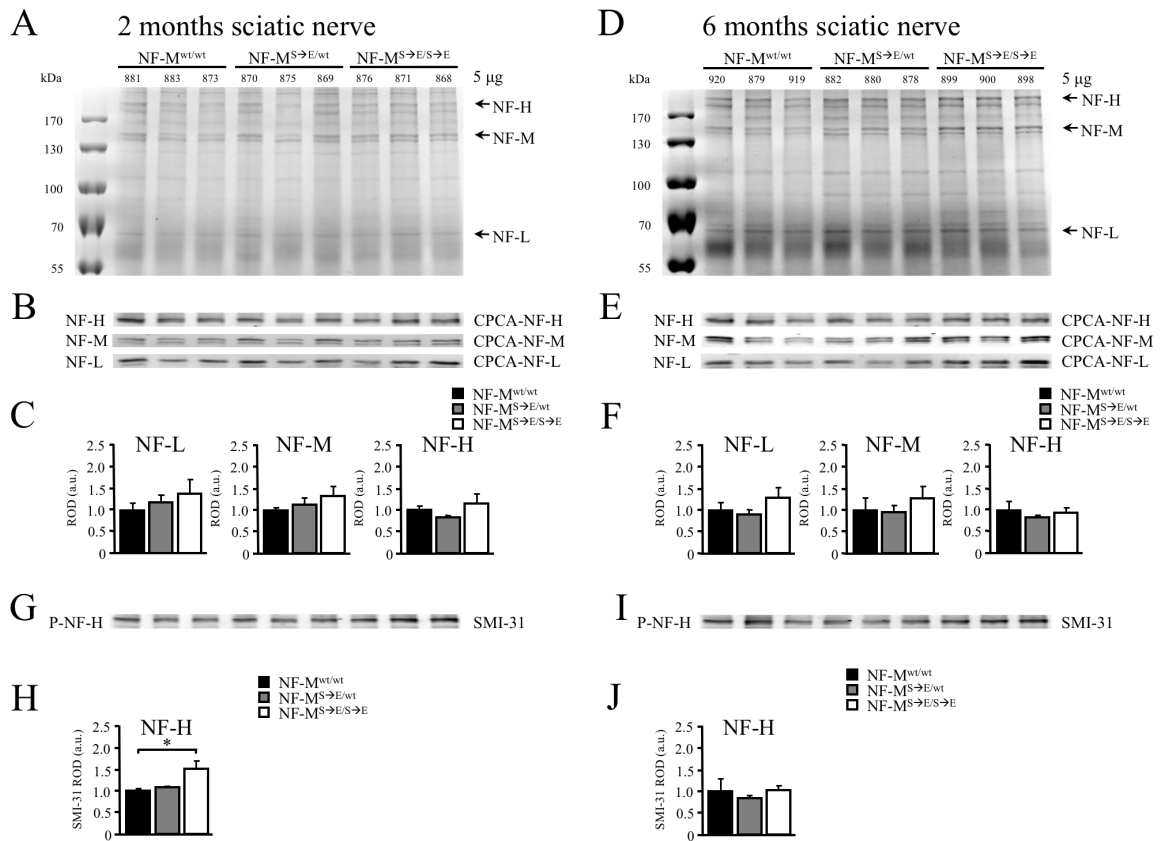


Figure 4.5. Expressing NF-M^{S→E} reduced phosphorylation dependent detection of NF-M in young mice. (A and D) Sciatic nerve protein extract from 2 and 6-month-old NF-M^{wt/wt}, NF-M^{wt/S→E}, and NF-M^{S→E/S→E} mice were resolved on a 7.5% SDS-polyacrylamide gel and stained with Coomassie Blue. NF-M mobility was not affected by expression of NF-M^{S→E} in the sciatic nerve. (B and E) Sciatic nerve extracts from 2 and 6-month-old mice were immunoblotted with antibodies that recognize NF-L (CPCA-NF-L), NF-M (CPCA-NF-M), and NF-H (CPCA-NF-H). Immunoblots confirmed that NF-M^{S→E} mobility was unaffected. (C and F) Relative optical densities (RODs) of immunoblots suggested that neurofilament subunit stoichiometry was not altered in NF-M^{S→E/S→E} or NF-M^{S→E/wt} mice relative to wild type. (G and I) Sciatic nerve extracts from 2 and 6 month-old mice were immunoblotted with an antibody that detects NF-H and NF-M in a phospho-dependent manner (SMI-31). (H and J) RODs suggested that the phospho-dependent antibody SMI-31 detected a significant increase in NF-H in NF-M^{S→E/S→E} mice and a significant decrease in NF-M in NF-M^{S→E/wt} at 2 months compared to NF-M^{wt/wt} mice (H). No alteration in NF-H or NF-M detection at 6 months was observed (J). ROD's were analyzed by one-way ANOVA. *, p < 0.05. Error bars = SEM. N= 3.

Motor, but not sensory, nerve conduction velocity was reduced in NF-M^{S→E/S→E} mice.

We measured motor and sensory nerve conduction velocity (NCV) in 6-month-old NF-M^{S→E/S→E} and NF-M^{wt/wt} mice (Fig. 4.6A and 4.6B). Motor NCV was ~27% reduced in NF-M^{S→E/S→E} mice relative to NF-M^{wt/wt} littermate controls ($p = 0.0123$, student's T-test) (Fig. 4.6A). Sensory NCV was unaffected (Fig. 4.6B).

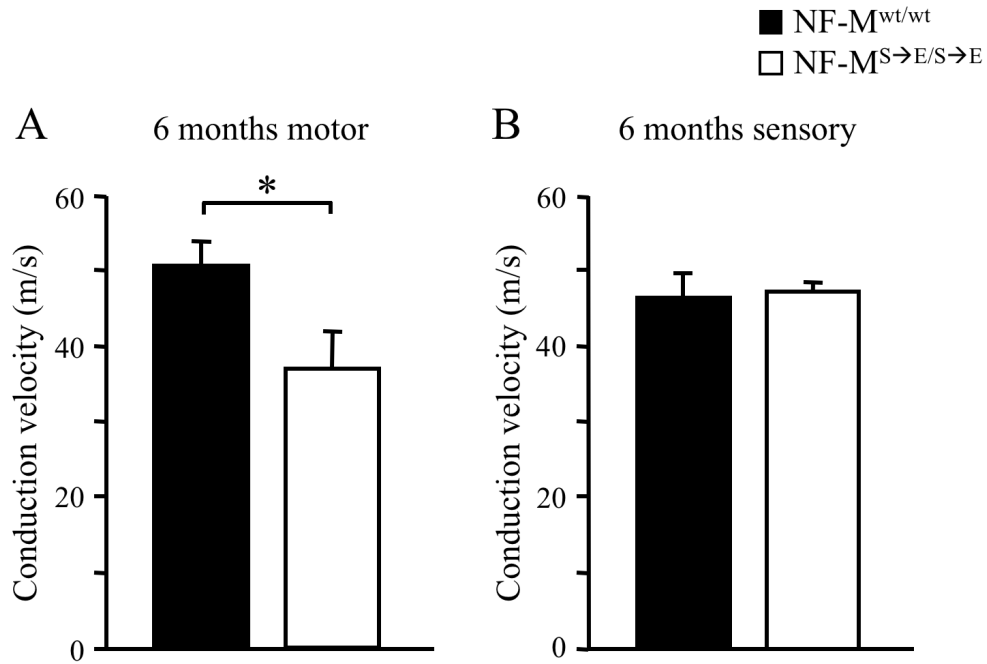


Figure 4.6. Motor, but not sensory, nerve conduction velocity was significantly reduced in NF-M^{S→E} mice. Motor and sensory nerve conduction velocity (NCV) was measured from sciatic nerve in 6-month-old NF-M^{wt/wt} and NF-M^{S→E/S→E} mice. NCV analysis revealed a ~27% decrease in motor NCV in NF-M^{S→E/S→E} mice (A). (B) Sensory NCV conduction velocity was indistinguishable between NF-M^{S→E/S→E} and NF-M^{wt/wt} controls. Nerve conduction velocities were analyzed by Student's *t*-test. *, *p* < 0.05. Error bars = SEM. N= 6.

Alterations in axonal diameter of motor but not sensory axons in mice expressing NF-M^{S→E}.

Three structural properties together determine the speed of neuronal conduction: axonal diameter, myelin thickness and internode length. To determine if mimicking phosphorylation of NF-M affected axon survival or growth, cross sections of the L5 motor (Fig. 4.7) and sensory (Fig. 4.6) root were taken from 2 and 6 month old NF-M^{S→E/S→E} and NF-M^{wt/wt} mice. There were no apparent differences in gross morphology (Fig. 4.7A and 4.8A) or axon number (Fig. 4.7B and 4.8B) at either time point for motor or sensory axons.

Cross-sectional areas were measured for all motor and sensory axons at both time points, and corresponding diameters were calculated. At 2 months, there was a 0.5µm increase in the peak axonal diameter of large diameter (> 4 µm) motor axons in NF-M^{S→E/S→E} compared to NF-M^{wt/wt} littermate controls (Fig. 4.7C). However, by 6 months, the diameters of all large diameter motor axons were indistinguishable between NF-M^{S→E/S→E} and NF-M^{wt/wt} mice (Fig. 4.7D). Small diameter motor axons (< 4µm) were similar at 2 months (Fig. 4.7C). However, at 6 months, the peak diameter for small diameter motor axons was 0.5 µm smaller in NF-M^{S→E/S→E} compared to NF-M^{wt/wt} (Fig. 4.7D). Axonal diameters of sensory axons were unaffected at 2 (Fig. 4.8C) or 6-months (Fig. 4.8D). Taken together these results suggested that alterations in axonal diameter were not the cause of reduced motor NCV in 6-month-old NF-M^{S→E/S→E} mice.

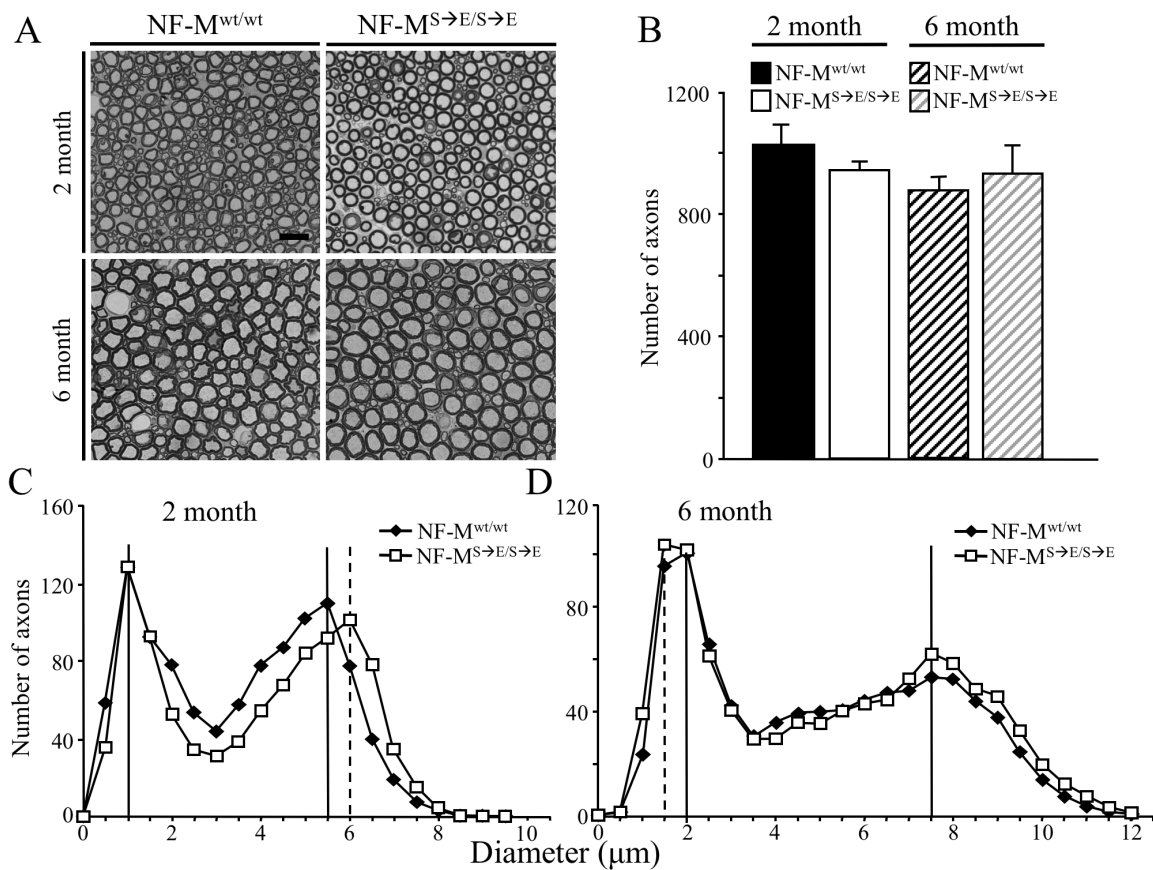


Figure 4.7. Expressing NF-M^{S→E} altered motor axon diameter without affecting survival. (A) Cross sections of the fifth lumbar motor (ventral) root (L5) from wild type and NF-M^{S→E/S→E} mice at 2 and 6 months. Scale bar, 10 μm. (B) Motor axon number was unaltered at 2 and 6 months in wild type and NF-M^{S→E/S→E} mice. (C and D) Axon diameter distribution from NF-M^{wt/wt} and NF-M^{S→E/S→E} mice at 2 and 6 months. Initially, NF-M^{S→E/S→E} mice had a 0.5μm increase in radial growth in large diameter motor axons (C). By 6 months, diameter distributions of large motor axons are indistinguishable between NF-M^{S→E/S→E} and NF-M^{wt/wt} mice (D). However, there was a 0.5μm decrease in the diameter of small motor axons in NF-M^{S→E/S→E} mice. Vertical lines in C and D identify peak diameters for small and large motor axons. N=6. Error bars = SEM. Axon counts were averaged from 5 animals per genotype per time point and analyzed for statistical significance by a two-way ANOVA.

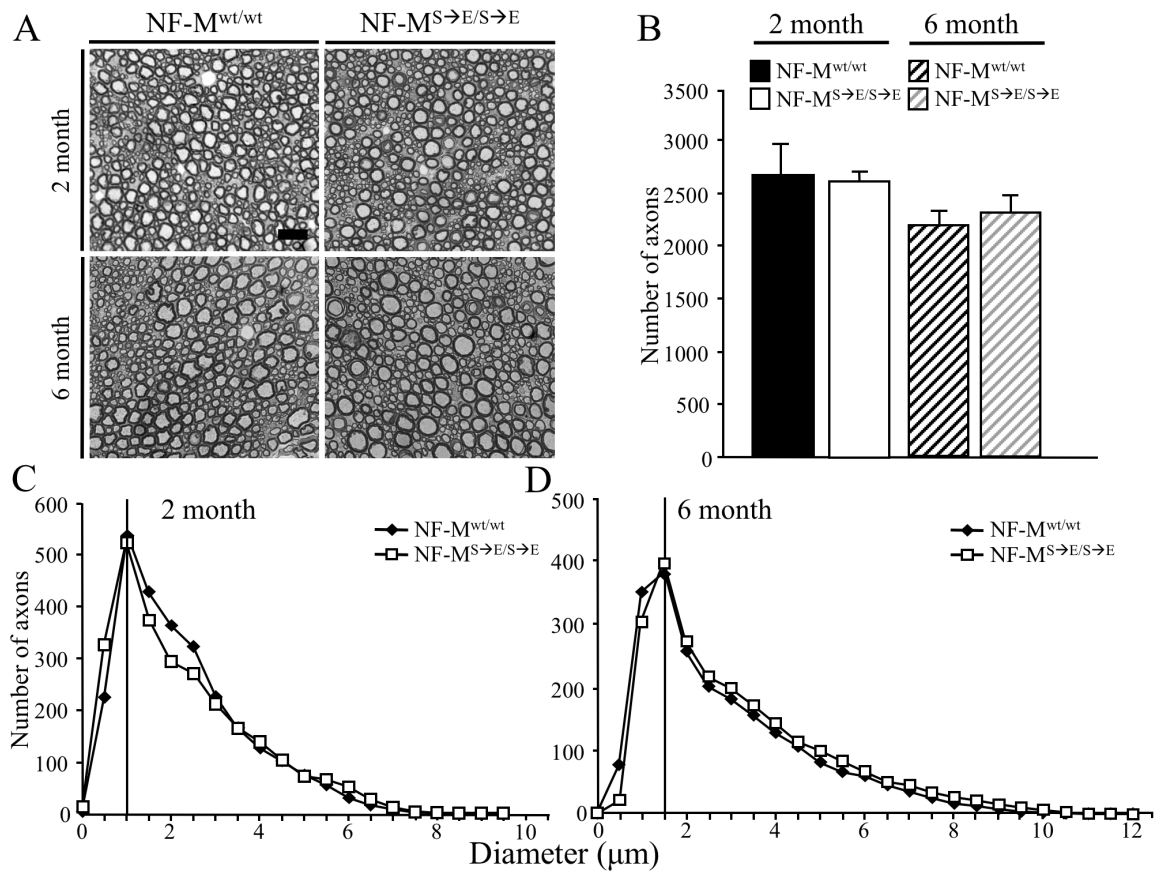


Figure 4.8. Expressing NF-M^{S→E} did not affect sensory axons. (A) Cross-sections of the fifth lumbar sensory root from NF-M^{wt/wt} and NF-M^{S→E/S→E} mice at 2 and 6 months. Scale bar, 10 μm. (B) Sensory axon number was unaltered at 2 and 6 months in wild type and NF-M^{S→E/S→E} mice. (C and D) Axon diameter distribution from NF-M^{wt/wt} and NF-M^{S→E/S→E} mice at 2 (C) and 6 (D) months. Peak diameters at both 2 (C) and 6 (D) were indistinguishable between NF-M^{S→E/S→E} and NF-M^{wt/wt}. Vertical lines in C and D identify peak diameters for sensory axons. Error bars = SEM. Axon counts were averaged from 5 animals per genotype per time point and analyzed for statistical significance by a two-way ANOVA.

Myelin thickness was unaltered in NF-M^{S→E/S→E} mice.

We next analyzed the ratio of axon diameter to fiber diameter (g-ratio) to determine if reduced motor NCV in NF-M^{S→E/S→E} mice was due to alterations in myelin thickness (Fig. 4.9A). Ten percent of the total axons were randomly selected for g-ratio calculations. At both 2 and 6 months, g-ratios of small (Fig. 4.9B) and large (Fig. 4.9C) motor axons were similar between NF-M^{S→E/S→E} and NF-M^{wt/wt}. NF-M^{S→E/S→E} sensory axon g-ratios were also indistinguishable from NF-M^{wt/wt} at 2 and 6 months (Fig. 4.9D). G-ratios were analyzed for statistical significance by Student's *t*-test, and no significant differences were found. These results suggested that decreased motor NCV of NF-M^{S→E/S→E} mice also cannot be explained by alterations in myelin thickness.

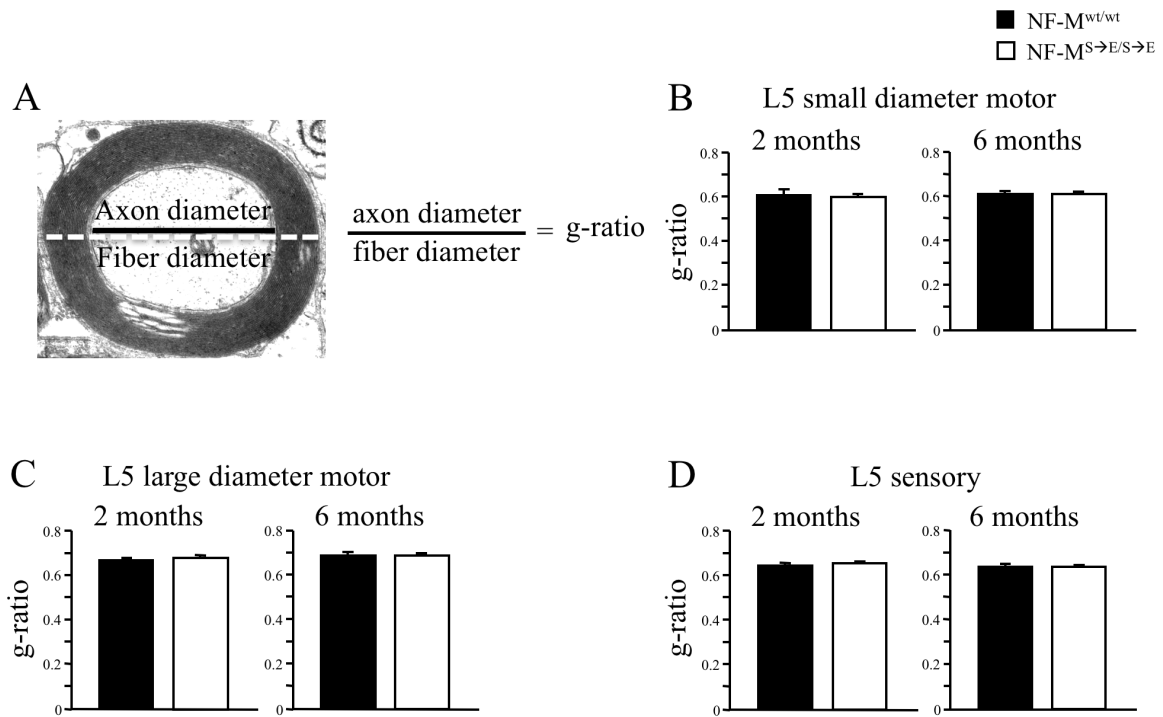


Figure 4.9. Myelin thickness was not affected in NF-M^{S→E} mice. (A) Schematic of measurements used to calculate g-ratios (g-ratio: axon diameter/fiber diameter) from 10% of large motor, small motor axons and sensory. (B, C and D) Analysis of axon diameter and myelin thickness suggested that g-ratio was unaltered in small motor (C), large motor (D), or sensory (E) L5 root axons. Results were analyzed for statistical significance with a Student's *t*-test. Error bars = SEM. N = 12.

Internode length of motor axons was reduced in NF-M^{S→E/S→E} mice.

Having eliminated alterations in axonal diameter and myelin thickness as potential explanations for reduced motor NCV, we analyzed the third structural property, internode length. Internode length was measured in teased fibers of the L5 motor (Fig. 4.10A) and sensory (Fig. 4.10B) roots. Internode length was significantly reduced in motor (Fig. 4.10C) but not sensory (Fig. 4.10D) axons in 6-month-old NF-M^{S→E/S→E} mice. Average internode length of motor axons was $927 \pm 26 \mu\text{m}$ and $778 \pm 45 \mu\text{m}$ for NF-M^{wt/wt} and NF-M^{S→E/S→E} mice, respectively (Fig. 4.10C). Average internode length of sensory axons was $831 \pm 34 \mu\text{m}$ for NF-M^{wt/wt} and $851 \pm 16 \mu\text{m}$ for NF-M^{S→E/S→E}, respectively (Fig. 4.10D). Internode lengths were analyzed for statistical significance by Student's *t*-test. These results indicate that expressing NF-M^{S→E} resulted in a 16% decrease in motor axon internode length, which may contribute to reduced motor NCV and that these effects were specific to motor axons.

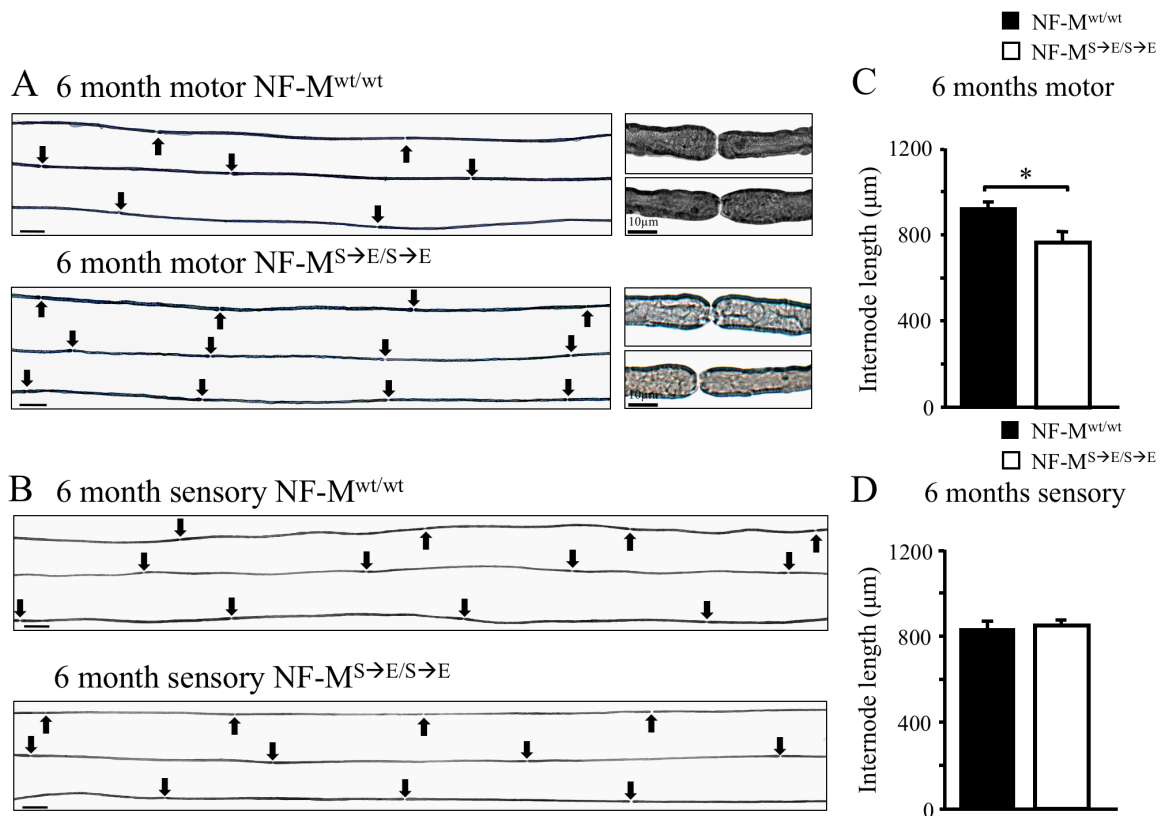


Figure 4.10. Internode length was decreased in L5 motor axons in NF-M^{S→E/S→E} mice. (A and B) Individual axons were teased from the L5 motor (A) and sensory (B) roots from 6-month-old NF-M^{wt/wt} and NF-M^{S→E/S→E} mice. Arrowheads identified the location of nodes of Ranvier. (A and B) Gross morphology of the nodes of Ranvier in L5 motor (A) and sensory (B) axons does not appear to be altered in NF-M^{S→E/S→E} mice compared to wild type controls. (C and D) ~ 5 internodes per axon from ~ 100 axons were analyzed for motor and ~ 4 internodes per axon from ~ 40 axons for sensory nerves were measured and analyzed from NF-M^{S→E/S→E} and NF-M^{wt/wt} mice. Analysis of teased fibers suggested that average internode length was significantly reduced in motor (C) but not sensory (D) axons of NF-M^{S→E/S→E} mice. Internode lengths were averaged and analyzed for statistical significance using a one-way nested ANOVA. *, $p < 0.05$. Error bars = SEM. N = 3.

Expressing NF-M^{S→E/S→E} reduced internode length early in Schwann cell elongation.

During development, two phases of Schwann cell elongation establish and maintain internode length. The first phase occurs with normal developmental myelination (Webster, 1971), and the second phase occurs during growth (Jacobs, 1988). To determine which phase was altered by expressing NF-M^{S→E/S→E}, we measured internode length over a time course (Fig. 4.11). Internode length was significantly reduced at 15 days (Fig. 4.11A), 1 month (Fig. 4.11B) and 6 months (Fig. 4.11C). Average internode lengths at 15 days were $475 \pm 27\mu\text{m}$ and $382 \pm 12\mu\text{m}$ for wild type and NF-M^{S→E/S→E}, respectively, which is approximately 20% reduced in NF-M^{S→E} mice. At 1 month, average internode lengths were approximately 16% reduced in NF-M^{S→E} mice ($708 \pm 25\mu\text{m}$ and $598 \pm 16\mu\text{m}$ for wild type and NF-M^{S→E} mice, respectively), which is similar to the reduction measured at 6 months. These results suggested that NF-M^{S→E} reduced internode length during the early phase of Schwann cell elongation and that it was maintained through the subsequent phase.

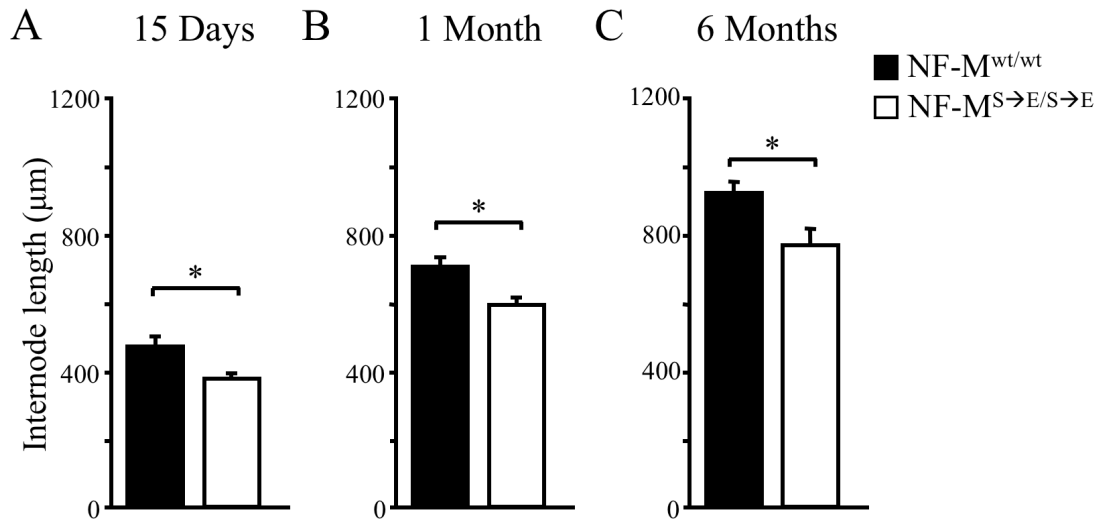


Figure 4.11. Expressing NF-M^{S→E} altered both phases of Schwann cell elongation. (A, B and C) Time course analysis of L5 motor axon internode length in NF-M^{S→E/S→E} mice at 15 days, 1 month and 6 months post birth. (A, B) ~ 200 internodes from varying number of L5 motor axons were measured from each animal at 15 days and 1-month postnatal. (C) L5 motor root teased fibers at 6-months as described in Fig. legend 9. Analysis of teased fibers suggested that average internode length was reduced at 15 days (A), 1 month (B) and 6 months (C). Average internode length was reduced by ~20%, ~16% and ~16% at 15 days, 1 month and 6 months, respectively. Internode lengths were averaged and analyzed for statistical significance using one-way nested ANOVA. *, p < 0.05. Error bars = SEM. N = 3 and 4 for NF-M^{wt/wt} and NF-M^{S→E/S→E} at 15 days, respectively. N = 5 for both NF-M^{wt/wt} and NF-M^{S→E/S→E} at 1 month.

Motor coordination is reduced in NF-M^{S→E/S→E} mice.

Decreased internode lengths and motor nerve conduction velocities are associated with deficits in motor coordination (Court et al., 2004; Wu et al., 2012). Motor coordination was, therefore, analyzed on the balance beam, which has been shown to provide a sensitive assessment of motor coordination in mice (Stanley et al., 2005). Relative to age matched controls NF-M^{S→E/S→E} mice had a significantly higher rate of falls (Fig. 4.12A) ($p = 0.0142$) and foot slips (Fig. 4.12B) ($p = 0.045$). Moreover, NF-M^{S→E/S→E} walked for a shorter period of time (not significant) (Fig. 4.12C) and a significantly shorter distance (Fig. 4.12D) ($p = 0.044$). However, the walking speed (Fig. 4.12E) and latency to fall (Fig. 4.12F) was similar in NF-M^{S→E/S→E} and NF-M^{wt/wt} controls. All measurements were analyzed for statistical significance by a Student's *t*-test. These results indicate that NF-M^{S→E/S→E} mice have impaired motor coordination by 2 months of age.

Sensitivity to noxious heat stimulation and tactile stimulation were not altered in NF-M^{S→E/S→E} mice.

Schwann cell elongation was significantly reduced in motor but not sensory axons. To determine if expressing NF-M^{S→E} altered sensory function, we measured response latency to thermal stimulus and response threshold to mechanical stimulus. Response to thermal stimulation was unaltered in NF-M^{S→E/S→E} mice relative to age-matched controls (Fig. 4.12G). Moreover, the response threshold to mechanical stimulus was also unaltered in NF-M^{S→E/S→E} mice (Fig. 4.12H). All measurements were analyzed for statistical significance by a Student's *t*-test. Taken together these results suggested that expressing

NF-M^{S→E} did not alter sensory nerve function, which was consistent with our result of unaltered sensory nerve morphology.

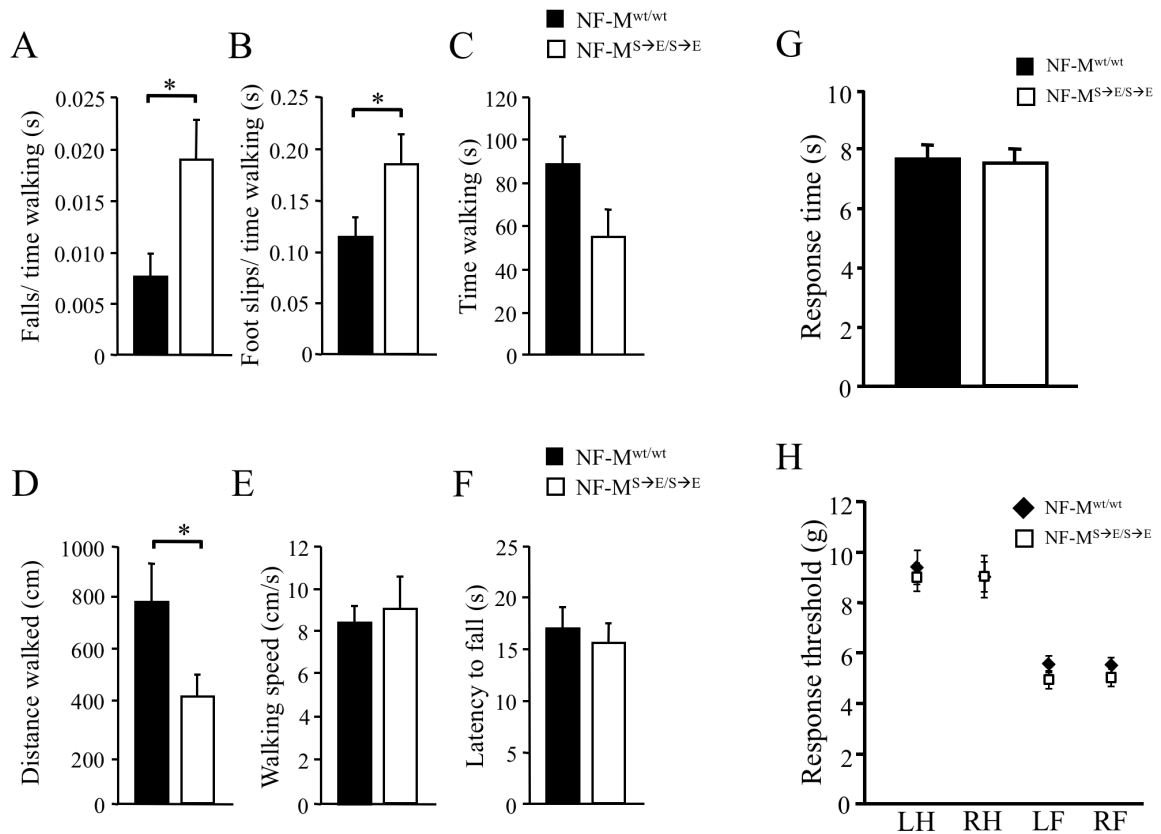


Figure 4.12. Motor coordination, but not sensory nerve function was reduced in NF-M^{S→E/S→E} mice. (A, B, C, D, E and F) Analysis of mouse performance on a balance beam at 2 months of age. NF-M^{S→E/S→E} mice had a significantly higher rate of falls (A) and foot slips (B) compared to wild type controls. In average, NF-M^{S→E/S→E} mice spent less time walking (C) and walked for a significantly shorter distance (D) than wild type controls. The time walking (C), walking speed (E) and the latency to fall (F) were not different in NF-M^{S→E/S→E} compared to NF-M^{wt/wt}. All observations were averaged for each genotype and analyzed for statistical significance by Student's *t*-test. *, *p* < 0.05. Error bars = SEM. *N* ≥ 13. (G) There was no difference in response to heat stimulus in the hind paws of NF-M^{S→E/S→E} mice and wild type. (H) Additionally, no difference was detected in response threshold to mechanical stimulus in front or hind paws of NF-M^{S→E/S→E} mice compared to wild type controls. Response to noxious heat (G) was averaged for each genotype by combining both hind paws measurements and analyzed for statistical significance by a Student's *t*-test. (*n* = 8). Response threshold to mechanical stimulus (H) was averaged for each individual paw and analyzed for statistical significance by Student's *t*-test. (*n* = 8). Error bars = SEM.

4.5. Discussion.

During developmental myelination, myelin thickness, internode length and axon diameter are all established cooperatively between Schwann cells and motor neurons. Moreover, during myelination, Lysine-Serine-Proline (KSP) repeats located within the C-termini of NF-M and NF-H become phosphorylated (de Waegh et al., 1992; Julien and Mushynski, 1983; Yin et al., 1998). While it has been known that myelination influences NF phosphorylation (de Waegh et al., 1992; Hsieh et al., 1994), the role for NF KSP phosphorylation is unclear (Garcia et al., 2009). Our results demonstrate, for the first time, that phosphorylation of NF-M KSP repeats is part of a mechanism that establishes the positive correlation between internode length and axon diameter, which was first observed over 140 years ago (Key and Retzius, 1875). We hypothesize that cooperatively establishing internode length during myelination involves interactions between neurons and elongating Schwann cells in a similar manner to defining edges during embryo development, which involves communication from cells on both sides of the developing border (Batlle and Wilkinson, 2012). Our results suggest that myelin-dependent phosphorylation of NF-M KSP repeats is a key step in defining boundaries between internodes and nodes of Ranvier.

Our results also provide a molecular basis for an empirical observation that was first made over 70 years ago (Vizoso and Young, 1948; Weiss and Hiscoe, 1948). The positive correlation between internode length and axon diameter is lost following remyelination since remyelinated internodes are uniformly short regardless of axon diameter (Gledhill et al., 1973; Vizoso and Young, 1948; Weiss and Hiscoe, 1948). Our data show that neurofilament phosphorylation is maintained after demyelination and

throughout remyelination, which correlates with reduced internode length. Similarly, constitutive expression of the phosphomimetic NF-M^{S→E} results in reduced internode length following developmental myelination. Both scenarios present cases where the spatial-temporal dynamics of adding negative charge to NF-M C-terminal KSP repeats is independent of myelination. Our results demonstrate that altering these dynamics restricts Schwann cell elongation reducing internode length, which provides the first mechanistic insights into reduced internode length following remyelination.

NF-M C-terminus establishes motor axon diameter (Barry et al., 2012; Garcia et al., 2003). The prevailing hypothesis was that myelin dependent phosphorylation of NF-M KSP repeats established axon diameter (de Waegh et al., 1992; Garcia et al., 2003; Yin et al., 1998). However, preventing NF-M KSP phosphorylation (NF-M^{S→A} mice) had no effect on axon diameter (Garcia et al., 2009) making the role of NF-M phosphorylation unclear. Our results provide a clear function for NF-M KSP phosphorylation, establishing internode length. Moreover, our results shed light on the dependency of NF-M phosphorylation on myelination (de Waegh et al., 1992). Premature phosphorylation results in short internodes, which alters nerve function by reducing the rate of impulse propagation along an axon (Brill et al., 1977; Court et al., 2004). Linking NF-M KSP phosphorylation with myelination allows for development of optimal internode length with clear demarcation between myelinated internodes and developing nodes of Ranvier. Interestingly, this role for NF-M phosphorylation is limited to motor axons. Expressing NF-M^{S→E} had no effect on sensory axon structure or function. In fact, altering NF proteins primarily affects motor axons (Rao et al., 2003; Rao et al., 2002b) suggesting that motor and sensory axon development depend on different molecular mechanisms.

Further analyses are required to investigate the disparity between motor and sensory axon development.

Lastly, our results provide a potential target for the development of therapies designed to enhance recovery from demyelinating diseases or from nerve injuries. Complete recovery from demyelination must include recovery of full-length internodes. Our results suggest that targeting neurofilament phosphorylation will enhance Schwann cell elongation during remyelination resulting in significantly longer internodes. Protein phosphatase 1 (Strack et al., 1997) and protein phosphatase 2A (Saito et al., 1995; Strack et al., 1997) have been co-purified with neurofilament proteins. Developing strategies for local delivery of small molecules that activate PP1 or PP2A could reduce neurofilament phosphorylation levels in demyelinated axonal segments allowing for more efficient Schwann cell elongation and longer internodes following remyelination.

CHAPTER 5

DISCUSSION

Vertebrate animal survival depends on their ability to respond and adapt to the surrounding environment, which requires an optimally functioning nervous system. The PNS function is to transmit signals to and from the periphery of the organism, which sometimes can be meters in length. Therefore, rapid PNS signaling is imperative for animals to respond quickly to their environment. While the main determinant of nerve conduction velocity is axonal diameter, myelination helps to maximize conduction speed (Waxman, 1980). Myelination, by Schwann cells in the PNS, leads to the formation of concentric layers of Schwann cell plasma membrane around the axon, known as compact myelin (Bhat, 2003; Bunge et al., 1989). The thickness of compact myelin is optimized for maximal conduction velocity (Waxman, 1980) by preventing loss of charge and decreasing capacitance across the axonal membrane (Huxley and Stampfli, 1949; Koles and Rasminski, 1972; Rasminski and Sears, 1972). During myelination, Schwann cells elongate along the axon, form the compact myelin layer, induce the clustering of Na_v^+ channels to form the nodes of Ranvier, and also establish optimal internodal length, all of which maximize conduction velocity (Brill et al., 1977; Huxley and Stampfli, 1949; Moore et al., 1978; Waxman, 1980). Formation of compact myelin also induces axonal radial growth to establish axonal diameter (de Waegh et al., 1992; Hsieh et al., 1994; Yin et al., 1998), which is dependent upon neurofilament proteins (Eyer and Peterson, 1994; Ohara et al., 1993; Zhu et al., 1997). All three axonal structures, myelin thickness, internodal length, and axonal diameter are optimized for maximal speed of electrical impulses and alterations to any of these structures compromise nerve conduction velocity

(Barry et al., 2012; Brill et al., 1977; Court et al., 2004; Garcia et al., 2003; Waxman, 1980).

Charcot-Marie-Tooth is the most common inherited disease of the peripheral nervous system and it is grouped into main types (CMT1-4) and X-linked depending on the specific genetic defects (Fridman et al., 2015; Szigeti and Lupski, 2009). To date, over 60 genes have been identified to cause a type of CMT (Bouhy and Timmerman, 2013). Despite the genetic variability of the disease, CMT patients present with very similar clinical phenotypes (Fridman et al., 2015). Typical CMT clinical presentations are reduced nerve conduction velocity, muscle wasting and atrophy, loss of sensation, and altered joint positioning sense (Fridman et al., 2015; Pareyson et al., 2006). Currently it is unclear as to how different types of CMT lead to similar clinical manifestations.

Moreover, CMT patients can experience exacerbation of neuropathy (Weimer and Podwall, 2006). Patients who were treated with non-toxic doses of prescribed drugs for the treatment of another underlying medical condition developed worsening of CMT symptoms (Chaudhry et al., 2003; Hildebrand et al., 2000; Martino et al., 2005; Weimer and Podwall, 2006). Discontinuing drug administration in these cases is the only way of preventing the disease from worsening even further (Weimer and Podwall, 2006). The mechanisms of neuropathy exacerbation are poorly understood and understudied and thus no treatment is available to prevent or reverse the effects of disease exacerbation.

Nerve damage due to disease, toxicity, or injury, typically leads to loss of myelin, or loss of both myelin and axons. Recovery from such injuries requires axon regeneration and myelination. Following recovery, both axon diameter and myelin sheath thickness increase back to pre-injury values (Devor and Govrin-Lippmann, 1979; Fricker et al.,

2013; Hoffman et al., 1984). However, internode length does not recover back to pre-injury values and compromises nerve function (Hildebrand et al., 1987; Sanders and Whitteridge, 1946; Vizoso and Young, 1948). Currently, it is not known why internode length does not recover after nerve injury.

Through the development of genetically modified mice significant insights have been made that help understand the pathogenesis of CMT neuropathy. My work provides further evidence to suggest that CMT2E neuropathy initiates within the proprioceptive sensory systems before affecting sensorimotor systems. These results allowed us to provide a unifying hypothesis to explain why CMT patients present with very similar clinical signs regardless of the type of CMT they are affected with. Moreover, my work demonstrates that insults to the peripheral nervous system, such as a nerve crush injury, lead to neuropathy exacerbation in our model of CMT 2E and establishes this model as a viable model to study the mechanisms of disease exacerbation. Lastly, utilizing genetically modified mouse models and demyelination paradigms my work provides novel molecular insights into the mechanisms that control Schwann cell elongation during formation of compact myelin that establish proper internodal length.

5.1. Charcot-Marie-Tooth type 2E neuropathy affects proprioceptive sensory systems before affecting sensorimotor systems.

CMT is classified into demyelinating (CMT1), axonal (CMT2), mixed (CMT3, and CMT 4) and X-linked (Fridman et al., 2015; Patzko and Shy, 2011). Despite the specific genetic defect CMT patients display typical disease signs like, foot deformities, muscle weakness and wasting, decreased nerve conduction velocity, decreased sensation

to heat and touch, and altered joint positioning sense (Fridman et al., 2015; Pareyson et al., 2006). Human patients carrying the E396K mutation in the neurofilament light gene develop typical CMT motor and sensory phenotypes (Berciano et al., 2015; Züchner et al., 2004). We generated CMT 2E mouse model carrying the human NF-L^{E396K} mutation, which developed similar motor phenotypes as those observed in humans (Dale et al., 2012; Shen et al., 2011; Villalon et al., 2015). However, it was unclear if this mouse model also developed alterations to sensory systems similar to humans with the hNF-L^{E396K} mutation. To determine if our CMT2E mouse model mimics the sensory alterations that human patients develop, I tested function of specific groups of sensory axons using different behavioral test paradigms at an age when typical symptoms appear (> 4 months).

Given that our mouse model develops overt CMT phenotype starting at 4 months of age, I investigated if at 6 months, they also develop motor coordination defects. For this, I tested the performance of our CMT mice on the balance beam. This test revealed a progressive increase in the number of foot slips while traversing the beam without alterations on time, distance, and walking speed. The frequency of foot slips while walking on the balance beam is a typical metric used to evaluate proprioceptive defects in mice (Muller et al., 2008; Stanley et al., 2005). These results together with previously observed increased number of hind limb foot drags while ambulating on a flat surface (Dale et al., 2012), suggested possible dysfunction group Ia and/or Ib sensory axons, which are large diameter sensory axons that mediate proprioception and joint positioning sense (Gilman, 2002). Next, I tested the mice sensitivity to mechanical stimulation by using a dynamic plantar stimulator. The results showed decreased sensitivity to touch in

the hind limbs and suggested altered function of group II sensory axons, which are also large diameter axons that mediate touch perception information (Casellini and Vinik, 2007). However, testing thermal sensitivity by the Hargreaves assay and hearing performance by auditory brainstem responses, revealed no alterations. This suggested that the function of small unmyelinated, group IV sensory axons (thermal nociception) (Yeomans et al., 1996; Yeomans and Proudfit, 1996) and small myelinated, group III, sensory axons (auditory response) (Gleich and Wilson, 1993), was unaltered. Taken together these results indicated specific functional alterations in large diameter sensory axons.

Previous analyses of the hNF-L^{E396K} animals revealed a slight decrease in the number of sensory axons within symptomatic animals compared to controls (Shen et al., 2011). However, these analyses reported no statistically significant differences in the number of sensory axons (Shen et al., 2011). Given that our previous behavioral analyses suggested alteration in a specific subset of sensory axons, I performed morphological analyses of L5 root sensory axons by dividing them into populations of large diameter axons (>5 μ m) and small diameter axons (\leq 5 μ m), at pre-symptomatic (2 months) and symptomatic (6 months) time points to gain insights into possible alterations that explained the behavioral results. Separation of sensory axons into small and large diameter types at two different time points revealed an age related increase in the number of large diameter axons of ~300 axons. Concomitantly, the number of small diameter axons decreased by ~ 300 axons suggesting that the small diameter axons grew in size from 2 to 6 months of age in control hNF-L mice. hNF-L^{E396K} mice showed the age related drop of ~300 small diameter axons similar to control animals. However, hNF-

L^{E396K} mice did not show the age related increase of large diameter sensory axons and thus ~300 large diameter axons were missing in symptomatic age hNF-L^{E396K} mice. These striking results together with the observed functional deficits suggested that hNF-L^{E396K} mice developed alterations primarily in sensory systems that utilize large diameter sensory axons, such as proprioception and joint position sense.

Evidence from a mouse model that lacks the ability to form muscle spindle due to the loss of the early growth response (Egr^{-/-}) gene suggested that absence of muscle spindle formation correlated with the loss of ~75% large diameter sensory axons (Tourtellotte and Milbrandt, 1998). Since my analysis revealed a loss of ~ 50 % large diameter sensory axons and altered performance on the balance beam, I investigated possible muscle spindle alterations in our CMT mice. Analysis of muscle spindle number and size from the EDL muscle revealed no difference in the number of muscle spindles either at 2- or 6- month-old mice. However, cross sectional area measurements and volume estimations revealed that hNF-L^{E396K} mice had overall significantly reduced muscle spindle cross sectional area and volume at 2 and 6 months of age. This was a surprising result, as the alterations in muscle spindle at 2 months of age became the first detectable pathological alteration in our CMT 2E mice. Taken together these results suggested that the loss of large diameter sensory axons was secondary to the muscle spindle alterations, similar to the observations made in the Egr^{-/-} mice (Tourtellotte and Milbrandt, 1998).

Taken together the results of my analyses on our CMT 2E mouse model allow us to propose that hNF-L^{E397K} pathology initiates in the proprioceptive sensory systems and then progresses to the sensorimotor systems to cause muscle atrophy and weakness,

reduced motor nerve function, gait alterations, and sensory loss. Our current results, together with the fact that a large number of mutations in many different genes result in similar CMT clinical manifestations (Bouhy and Timmerman, 2013) and that many CMT rodent models develop early sensory system alterations (Achilli et al., 2009; d'Ydewalle et al., 2011; Gillespie et al., 2000; Lee et al., 2013; Sereda et al., 1996), suggest that early and selective proprioceptive sensory dysfunction might provide a unifying hypothesis of disease pathogenesis in CMT.

5.2. Sciatic nerve crush injury results in neuropathy exacerbation in a mouse model of CMT2E.

CMT patients are prone to neuropathy exacerbation. Evidence suggests that treatment of CMT patients with non-toxic doses of prescribed drugs for a separate underlying condition often leads to worsening of CMT symptoms (Chaudhry et al., 2003; Hildebrand et al., 2000; Martino et al., 2005; Weimer and Podwall, 2006). Exacerbation of neuropathy results in muscle weakness in both upper and lower limbs, inability to support weight (Hildebrand et al., 2000), development of pain, and decreased coordination while walking (Chaudhry et al., 2003; Martino et al., 2005). Moreover, the only intervention available in these situations is discontinuation of drug treatment, which is followed by reduced or no recovery of CMT symptoms (Chaudhry et al., 2003; Hildebrand et al., 2000). The current understanding of CMT neuropathy exacerbation and recovery is marginal due to the lack of reliable animal model of the condition.

Therefore, I tested the effects of a traumatic nerve injury on CMT neuropathy in our hNF-L^{E396K} mouse model. Following a sciatic nerve crush to the left leg, I analyzed functional recovery and gait alterations after recovery from injury. Functional recovery

was analyzed by measuring the mouse ability to spread their digits on the injured limb during. My results showed that hNF-L^{E396K} mice recovered similarly to control animals up to day 15 post-injury. However from day 16 forward, hNF-L^{E396K} mice began to show reduced recovery compared to control mice. Ultimately hNF-L^{E396K} mice recovered only 89% of their ability to spread their toes, suggesting that their pre-existing neuropathy worsened after recovery from the nerve crush.

Previous Catwalk gait studies on our CMT animals revealed that they develop interlimb coordination defects with no alterations to print width, print length or max contact area (Dale et al., 2012). These metrics are used to investigate alterations in weight bearing ability during voluntary locomotion in rodents (Angeby-Moller et al., 2008; Gabriel et al., 2007; Medhurst et al., 2002; Min et al., 2001; Tabo et al., 1998). Gait analyses revealed that hNF-L^{E396K} mice developed significant reductions in print width, print length and max contact area after recovery from nerve injury compared to controls. These results suggested that recovery from nerve injury is accompanied by decreased ability to bear weight, or increased mechanical allodynia or a combination of both. Moreover, the altered ability to bear weight had subsequent effects on gait coordination while ambulating. Previous analyses revealed that hNF-L^{E396K} mice normally develop interlimb coordination while ambulating (Dale et al., 2012). My analysis revealed that following recovery from nerve injury our mice developed similar interlimb coordination defects that were more pronounced than previously seen (Dale et al., 2012). These results allowed us to conclude that nerve injury exacerbates CMT2E neuropathy and leads to alterations on sensory and motor coordination pathways on the injured limb after recovery.

Following a nerve crush injury there is a period of nerve degeneration that occurs from day 1 to day 7-post injury (Gordon and Stein, 1982a; Gordon and Stein, 1982b; Jager et al., 2014; Ronchi et al., 2010). This period is followed by a nerve regeneration and re-innervation period from day 7 to about day 20-post injury (Gordon and Stein, 1982a; Gordon and Stein, 1982b; Jager et al., 2014; Ronchi et al., 2010). After re-innervation, axons undergo radial growth to regain pre-injury axonal diameters (Gordon and Stein, 1982a; Gordon and Stein, 1982b; Sta et al., 2014; Wood et al., 2011). Our results indicate that hNF-L mice are able to recover similar to control mice up to day 20-post injury. This would correspond to the regeneration and re-innervation period. However, from day 20 post-crush onwards, hNF-L^{E396K} mice do not further recover like the controls do. This corresponds to the period of axonal diameter recovery and thus suggests possible axonal radial growth defects in hNF-L^{E396K} mice (Gordon and Stein, 1982a; Gordon and Stein, 1982b; Sta et al., 2014; Wood et al., 2011). Interestingly, initial characterization of symptomatic hNF-L^{E397K} mice revealed reductions in nerve conduction velocity and axonal diameters in the motor nerves (Shen et al., 2011). These data taken together allow us to suggest that inability of axons to expand radially following regeneration, which would cause further reductions in nerve conduction velocity, might be a possible mechanism of disease exacerbation in CMT2E neuropathy.

Finally, our functional recovery and gait analysis results suggest that nerve injury exacerbates CMT2E neuropathy by possibly preventing the recovery of axonal diameter and leading to decreased nerve function. This in turn affects the normal function of sensorimotor pathways causing exacerbated gait alterations. These results also provide a possible new approach for investigating exacerbation of neuropathies.

5.3. Proposed model of hNF-L^{E396K} disease pathogenesis.

CMT2E causes nerve dysfunction by altering the morphological development of the peripheral nervous system (Bird, 1993b; Bird, 2016). The NF-L^{E397K} mutation in humans leads to decreased nerve conduction velocity, muscle atrophy and sensory loss (Berciano et al., 2015; Züchner et al., 2004). However, the disease pathogenesis of this mutation remains unknown. Our current work utilizing mouse model provides new details that help provide a pathogenesis model of this mutation.

Taking our current findings together with previous data furthers our understanding on the pathogenic mechanisms by which the E396K mutation leads to disease. Following chronologically the development of disease in our mouse model, the earliest sign of pathogenesis in the hNF-L^{E396K} was detected at 1 month of age (Fig. 5.1). Motor neurons in the ventral horn, of the spinal cord show ectopic phosphorylation of neurofilaments, which appear to affect both α -motor or γ -motor neurons (Shen et al., 2011). Ectopic accumulations of phosphorylated neurofilaments are a hallmark for neurodegenerative diseases such as ALS and lead to significant reduction in axonal diameter, neuronal loss, and ultimately muscle atrophy due to denervation (Boillee et al., 2006; Clement et al., 2003; Hirano et al., 1984; Lobsiger et al., 2007) At this point, no abnormalities in muscle fiber morphology were found (Shen et al., 2011). By 2 months of age, L5 ventral root morphological analysis revealed a small reduction in γ -motor axon diameter (Shen et al., 2011). Diameters of α -motor axons were normal at this time point. In addition, the number and diameter of sensory axons from the L5 dorsal root did not show alterations compared to the controls (Shen et al., 2011). My current data demonstrates that at 2 months of age, the muscle spindle size in the extensor digitorum

longus (EDL) muscle was significantly reduced compared to controls (Fig. 5.1). Muscle spindles are innervated by γ -motor neurons and type I sensory axons (Friese et al., 2009). From the current data, I hypothesize that the accumulation of ectopically phosphorylated neurofilaments in γ -motor neuron cell body alters neurofilament dynamics in the axon and causes the reduction in axonal diameter observed in γ -motor axons at 2 months of age. This effect would be similar to what has been observed in ALS (Boillee et al., 2006; Clement et al., 2003; Hirano et al., 1984; Lobsiger et al., 2007). Axonal diameter is the main determinant of nerve conduction velocity and reductions in axonal diameter directly reduce conduction velocity (Garcia et al., 2003; Waxman, 1980). Thus, the reduced γ -motor axon diameters are likely to reduce function of γ -motor axons and limit the input to muscle spindles, which leads to atrophy of the muscle spindle fibers and consequently reduced muscle spindle size (Elsohemy et al., 2009) (Fig. 5.1). The reduced muscle spindle function early on could also contribute to the reduced voluntary activity observed in hNF-L^{E396K} mice (Fig. 5.1). Interestingly, at this time point, the number and diameter of α -motor and sensory axons are not different than those of the controls. I hypothesize that the ectopic accumulations of phosphorylated neurofilaments affect motor neurons in a size dependent manner such that the small motor neurons are affected prior to large motor neurons. Taking this in consideration then, as disease progresses, the ectopic neurofilament accumulation will eventually affect large motor neurons. By 6 months of age, muscle spindle size has not recovered and remains significantly reduced compared to controls. In addition, axonal diameter of large α -motor axons is reduced (Shen et al., 2011) similar to the reductions in γ -motor axons at 2 months (Fig. 5.1). The alterations in axonal diameters could be directly responsible for the reduced motor nerve conduction

velocity (Shen et al., 2011). Alterations to nerve function could directly impact the input to muscle fibers and this could be a contributor to the muscle atrophy observed at 6 months (Shen et al., 2011). In addition to reduced input to muscle fibers by motor neurons, reduced voluntary activity observed at earlier ages could contribute to the reductions in muscle fiber size as it has been well documented that reduced activity of muscles directly leads to muscle fiber atrophy (Jackson et al., 2015; Perkin et al., 2015).

Denervation of muscle fibers also causes muscle atrophy (Bongers et al., 2013). However, this is not likely explanation for the cause of muscle atrophy, as no muscle denervation was observed in our mice (Shen et al., 2011). Rather, I hypothesize that the reduced voluntary activity due to altered muscle spindle function early on leads to the muscle atrophy in later stages of disease pathogenesis. Moreover, at 6 months, my analysis of sensory axons revealed a loss of 50% large diameter sensory axons. Previous analysis by Shen et al. 2011 show a decrease in the total number of sensory axons of in symptomatic hNF-L^{E396K} mice compared to controls. However, those differences did not reach statistical significance since the analysis was performed on the total number of axons per root (Shen et al., 2011). In my current analysis I separated the total number of axons into two main sensory axon populations according to size. My analysis revealed demonstrates that the missing axons belong to a specific group of sensory axons, large sensory axons, which must be analyzed separately to detect these important differences. However, it is not clear from the existing data what caused the loss of those large diameter sensory axons. Consequently, the loss of large diameter axons, which could include type I (proprioceptive) and type II (mechanoreceptive) axons, directly causes

reduced mechanical sensitivity and motor coordination. Muscle spindle size reductions at 6 months of age can also contribute to the altered motor coordination.

By 6 months of age, our CMT mouse model displays several phenotypic alterations that reflect the phenotype developed by humans with the disease. Human patients suffering with the NF-L E397K mutation display reductions in axonal diameters, motor nerve conduction velocity, muscle atrophy, loss of sensation, and balance defects (Jordanova, 2003; Züchner et al., 2004). All of these alterations are also observed in our CMT mouse model confirming it as a reliable model of the disease. My analysis on our mouse model revealed important insights into alterations that have not been studied in human patients. Early development of undersized muscle spindles and significant loss of large diameter sensory axons in later stages of disease could be keys to understanding the pathogenesis of disease in human patients. Thus, these alterations should be further studied in both humans and other models of CMT2E.

My analysis of this mouse model in addition to previous data allowed me to propose the following mechanism of disease development. The NF-L^{E396K} mutation initially alters neurofilament dynamics and leads to ectopic accumulations of phosphorylated neurofilaments in the neuronal cell bodies. In early stages of disease, ectopic neurofilament accumulations affect motor neurons in a size dependent manner. This causes reduced axonal diameters in γ -motor axons, which eventually alter muscle spindle function and lead to reduced muscle spindle size. Altered muscle spindle function contributes to reduced voluntary activity. As disease progresses, neurofilament accumulations eventually affect large motor axons leading to reduced motor axon diameter and motor nerve conduction velocity, which alters input to muscle fibers. Early

reductions in voluntary activity continue throughout disease and result in muscle atrophy in later stages, which could be augmented by reduced motor nerve function. In later stages of disease, the reduced muscle spindle size in combination with loss of large sensory axons leads to altered proprioceptive function and causes motor coordination defects. Loss of sensation in later stages is also a result of the loss of large diameter sensory axons.

Therefore, if my proposed model is accurate, investigating early alterations to proprioceptive sensory organs in humans could be useful in detecting the development and possibly reducing disease progression in humans. If the reduced function of muscle spindles causes reduced voluntary activity, which eventually caused muscle atrophy, then including a regimen of physical activity in human patients that are carriers or at risk of developing disease could help prevent the atrophy of muscle fibers. To test this idea using our mouse model, I would set up two cohorts of mice with controls. I would give access to a running wheel to one cohort of mice since 2 weeks of age while the other cohort of mice will not be given access to a running wheel. At 6 months of age I would perform muscle morphology analysis. If my model is correct I expect to see a significant improvement in muscle spindle size and muscle fiber size in animals with readily access to a running wheel compared to animals with no access to a running wheel. To prove that the increase in voluntary activity rescues the loss of muscle spindle size and muscle fiber size I would perform another experiment with two more cohorts of animals. One cohort, hNF-L^{E396K} and controls would be submitted to daily rounds of exercise by placing the animals on the rotarod for 30 minutes at low speed every other day for 4 months and then analyze the muscle morphology. I would expect to see no signs of muscle atrophy on

mice forced to exercise compared to non-exercised mice. These results could be crucial for developing therapeutic treatments for human patients with the disease.

However, muscle fiber atrophy makes up one part of the disease pathogenesis in humans and in our mouse model. Reductions in motor axon diameters and loss of sensory axons are also key contributors to disease pathogenesis. In my model, I hypothesize that the reduction in axonal diameters in motor axons is caused by altered neurofilament dynamics, which affects axons in a size dependent manner. Reduced axonal diameters in human patients have also been observed (Züchner et al., 2004). However, analysis of ectopically phosphorylated neurofilaments has not been performed due to lack of tissue availability. This idea would be difficult to investigate in human patients, as a piece of their spinal cord would be needed to investigate ectopic accumulation of neurofilaments. Recent research in ALS patients shows that elevated levels of phosphorylated neurofilaments can be detected in cerebrospinal fluid (CSF) and plasma, which is a promising biomarker for early detection of disease development (Ganesalingam et al., 2012; Ganesalingam et al., 2011). Thus, perhaps using a similar protocol to screen for the presence of elevated levels of phosphorylated neurofilaments in the CSF and/or plasma of human patients with family history of CMT could give insights into disease development before development of overt phenotype. If ectopic neurofilament phosphorylation is an alteration detectable in very early stages in human patients, and if the ectopic neurofilament phosphorylation is responsible for the reduction of axonal diameters, then developing therapeutic treatments to prevent or reduce ectopic neurofilament phosphorylation could be an important area for future investigation to develop treatments for the disease.

Furthermore, the loss of large sensory axons remains a mystery. Research in sensory axons is limited in any model of peripheral neuropathy. Thus, further investigation focusing on alterations specifically in sensory neurons and axons could provide further insights into the development of disease. I hypothesize that ectopic neurofilament accumulation in sensory axon also plays an important role in causing the loss of sensory axons. To investigate this, I would begin by performing immunohistochemistry on dorsal root ganglion neurons to look for accumulation of ectopically phosphorylated neurons in a time course beginning at early ages. If a correlation between sensory axon loss and ectopic neurofilament phosphorylation is found then, the focus for future investigations should shift to prevent or reverse ectopic neurofilament phosphorylation in all peripheral nervous system neurons.

My current contributions are crucial for furthering the understanding of CMT2E disease pathogenesis. Alterations to muscle spindle have never been shown or investigated before in any model of CMT or in human patients. Muscle spindle alterations in the extensor digitorum longus (EDL) muscle in our mouse model opened the door to a new area of investigation for CMT2E. However, it is unclear if muscle spindles are equally affected in other muscles. Similarly, muscle atrophy was investigated in the gastrocnemius muscle only, and it is not clear if surrounding muscles are also atrophied. The EDL muscle is composed primarily of fast twitch muscle fibers (Augusto et al., 2004; Soukup et al., 2002), whereas the gastrocnemius muscle has a higher percentage of slow twitch fibers and the soleus muscle is composed of almost 50% slow twitch muscle fibers (Augusto et al., 2004). To investigate if the alterations to muscle spindle or muscle atrophy correlate with the fiber type composition of the muscle, spindle

and atrophy analyses should be performed in several different muscles in the distal limb that are affected by CMT. These muscles would include, the gastrocnemius, soleus, tibialis anterior, lumbricals, and flexor digitorum longus. All of which, have different composition of slow and fast twitch muscle fibers. Studies in animal models of spinal muscular atrophy (SMA), a disease that affects the nervous system, show that different muscle groups have different propensity to be affected by the disease (Ling et al., 2012; Murray et al., 2008). Therefore, if CMT2E acts similarly to SMA and affects different muscle groups to different degrees, then we could target muscle groups that are more severely affected to address the mechanisms of muscle spindle alterations and muscle atrophy. Moreover, this knowledge could allow future studies for developing and evaluating efficacy of therapeutic treatments for CMT2E.

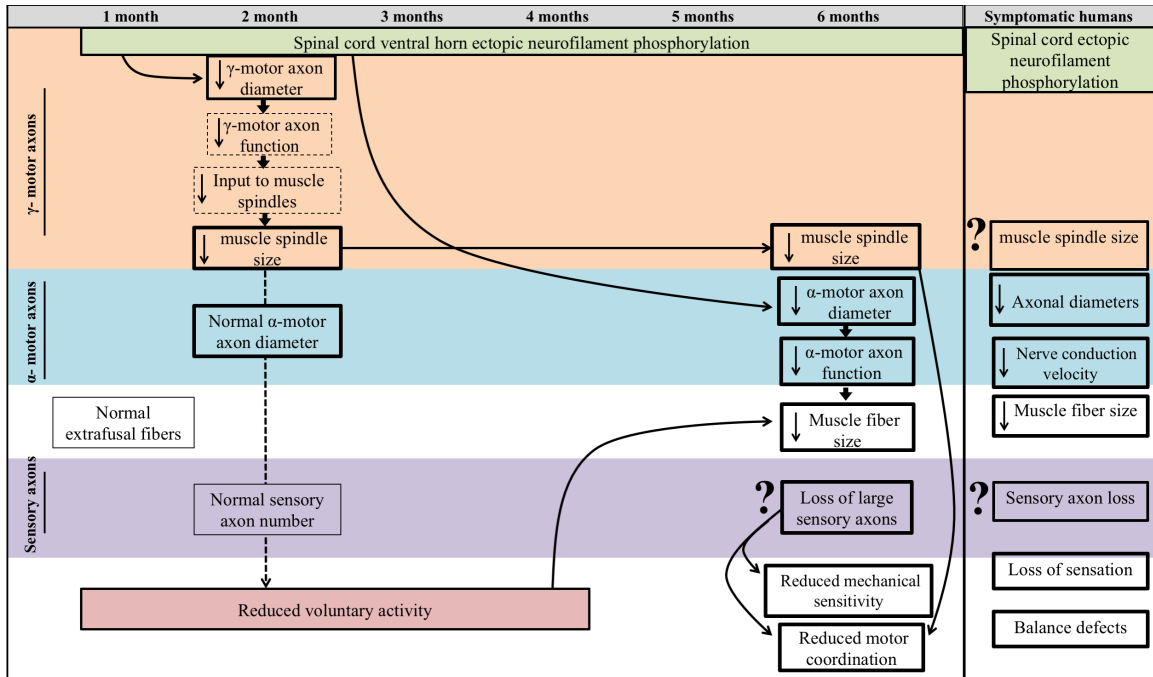


Figure 5.1. Model of hNF-L^{E396K} disease pathogenesis. Based on the current knowledge from our CMT mouse model disease pathogenesis initially causes ectopic accumulations of phosphorylated neurofilaments in motor neuron cell bodies detectable at 1 month of age. These NF accumulations affect motor neurons in a size dependent manner. By 2 months of age, NF accumulations cause the reduction of γ -motor axon diameter, which causes reduced γ -motor function and input to muscle spindles. The reduced input to muscle spindles leads to development of undersized muscle spindles by 2 months of age. Altered muscle spindle function in turn contributes to the reduced voluntary activity observed in mice from 1 to 4 months of age. As disease progresses NF accumulations begin to affect large motor neurons (α -motor neurons) and cause reductions in α -motor axons by 6 months of age. Reduced α -motor axon diameter causes reductions in nerve conduction, which alter nerve function and input to muscle fibers. Reduced input to muscle fibers in combination with reduced voluntary activity leads to muscle atrophy by 6 months of age. Moreover, by 6 months of age about 50% of large diameter sensory axons are lost, for which no explanation is available yet. The loss of large diameter sensory axons directly causes reduced mechanical sensitivity and in combination with altered muscle spindle function causes reduced motor coordination. By 6 months of age disease pathogenesis in our mouse model develops similar phenotypic alterations as human patients affected by the disease. Interestingly, in humans, muscle spindle alterations and sensory axon loss have not been investigated. This current model of disease pathogenesis indicates that muscle spindle and sensory axon alterations are important areas to target for early pathogenesis detection and therapeutic treatment development for CMT2E.

5.4. Neurofilament medium C-terminus phosphorylation restricts Schwann cell elongation.

Damage to the peripheral nervous system can result from conditions like diseases, injury, or toxicity (Gledhill et al., 1973; Gupta et al., 2012; Saporta et al., 2009; Vizoso and Young, 1948; Waxman and Brill, 1978; Weiss and Hiscoe, 1948). Such conditions can lead to loss of myelin or loss of both myelin and axon, all of which directly affect nerve function. Following a nerve injury there is a recovery period that allows for axon re-growth and re-innervation and remyelination. Both myelin sheath thickness and axonal diameter, important determinants of nerve conduction velocity, eventually recover back to pre-injury levels (Fricker et al., 2013; Hoffman et al., 1984). However, internode length, which is also important for maximal conduction velocity, does not recover to pre-injury levels (Vizoso and Young, 1948). Although it has been known for over 70 years that internode length remains dramatically reduced after recovery from injury (Vizoso and Young, 1948; Weiss and Hiscoe, 1948), the mechanism controlling Schwann cell elongation has not been described.

It is well known that axon diameter positively correlates with internode length, i.e. larger diameter axons have longer internodes, suggesting that Schwann cell elongation during myelination is a coordinated process between the Schwann cells and the axon. Axonal diameter is determined by NF-M C-terminus (Barry et al., 2012; Garcia et al., 2003) upon formation of compact myelin (de Waegh et al., 1992). The prevailing hypothesis was that myelin dependent NF-M C-terminus phosphorylation established axon diameter (de Waegh et al., 1992; Garcia et al., 2003; Yin et al., 1998). However,

preventing NF-M KSP phosphorylation did not affect axonal diameter (Garcia et al., 2009) making the role of neurofilament phosphorylation during myelination unclear.

Analysis of neurofilament expression and phosphorylation during demyelination and remyelination demonstrate that NF-M remains phosphorylated after demyelination and during remyelination. Moreover, internode length after remyelination is reduced by ~75%. Preventing phosphorylation of NF-M C-terminus (NF-M^{ΔTail}) during remyelination resulted in a significant 30% increase in internodal length. These results suggested a possible correlation between axonal NF-M phosphorylation and reduced Schwann cell elongation during the establishment of internode length. To confirm this correlation, we generated a novel line of genetically modified mice that mimic constitutive phosphorylation of NF-M C-terminus (NF-M^{S→E}). Internode length analyzes in NF-M^{S→E} mice revealed significantly reduced internodal lengths as early as 15 days of age, which are maintained through adulthood. Reduced internode lengths resulted in significant reductions in motor nerve conduction velocity and impaired motor performance in NF-M^{S→E} mice. Therefore, my results provide a clear function for NF-M C-terminus phosphorylation, establishing internode length. Furthermore, these results in predict that Schwann cell elongation will be reduced when elongation occurs in the presence of phosphorylated neurofilaments.

Previous studies on NF-M C-terminus phosphorylation in myelinated axons demonstrated a clear dependence of NF-M C-terminus phosphorylation on formation of compact myelin such that myelinated axonal areas (internodes) have increased NF-M phosphorylation levels and non-myelinated areas (nodes of Ranvier) have low NF-M phosphorylation levels (de Waegh et al., 1992; Sanchez et al., 2000). Moreover, it has

been known for over 140 years that internode length positively correlates with axonal diameter (Key and Retzius, 1875). Mimicking premature NF-M phosphorylation reduced Schwann cell elongation with no alterations in axon diameter. Given that normally NF-M phosphorylation is dependent upon myelination, mimicking premature NF-M phosphorylation alters the spatial-temporal dynamics of NF-M phosphorylation and leads to formation of shorter internodes. It is possible that establishing internode lengths is similar to defining edges during embryo development. This mechanism would involve communication from cells on both sides of the developing border (Batlle and Wilkinson, 2012). Thus, premature NF-M phosphorylation in the axon would signal the Schwann cells to stop elongating before axons reach their normal diameters. These data demonstrate that NF-M C-terminus phosphorylation is part of the mechanism that establishes the positive correlation between axonal diameter and internode length.

Expression of NF-M^{S→E} resulted in significantly reduced motor internode length and altered motor nerve function. However, sensory nerve structure or function was unaffected. Previous studies, in which modifications to neurofilament proteins lead to significant alterations to motor axon structures, have shown that sensory axons are minimally affected (Rao et al., 2003; Rao et al., 2002b) suggesting that motor and sensory axon development depend on different molecular mechanisms. Further analyses are required to investigate the disparity between motor and sensory axon development.

5.5. Proposed mechanism of reduced Schwann cell elongation by NF-M phosphorylation.

Our current findings demonstrate that the phosphorylation of NF-M C-terminus plays an important role in the establishment of internode lengths during myelination of motor axons. Current evidence indicates that during normal development axonal neurofilaments are in an unphosphorylated state and remain unphosphorylated until the formation of compact myelin by Schwann cells (Normal Myelination, Fig. 5.2). Mimicking the expression of NF-M (NF-M^{S→E}) creates a scenario where NF-M is phosphorylated before Schwann cells associate with axons and begin the myelination process. Since NF-M is prematurely phosphorylated during myelination, Schwann cells do not elongate to their normal lengths and form shorter internode lengths (NF-MS→E Development, Fig 5.3). Furthermore, our data indicate that remyelination following an injury would be done under similar conditions as in normal myelination in the NF-M^{S→E} model. During remyelination axonal neurofilaments are already highly phosphorylated before Schwann cells associate with the naked axons and begin remyelinating. Thus, the presence of phosphorylated neurofilaments reduces Schwann cell elongation and results in shorter internode lengths during remyelination (Normal Remyelination, Fig.5.2). These data so far indicate that if NF-M phosphorylation is prevented during myelination, this could result in longer internode lengths after remyelination. Thus, experimentally dephosphorylating neurofilaments following a demyelinating condition and maintaining them dephosphorylated during the phosphorylation process, would allow normal Schwann cell elongation and result in normal internode lengths (Experimental Remyelination, Fig. 5.2).

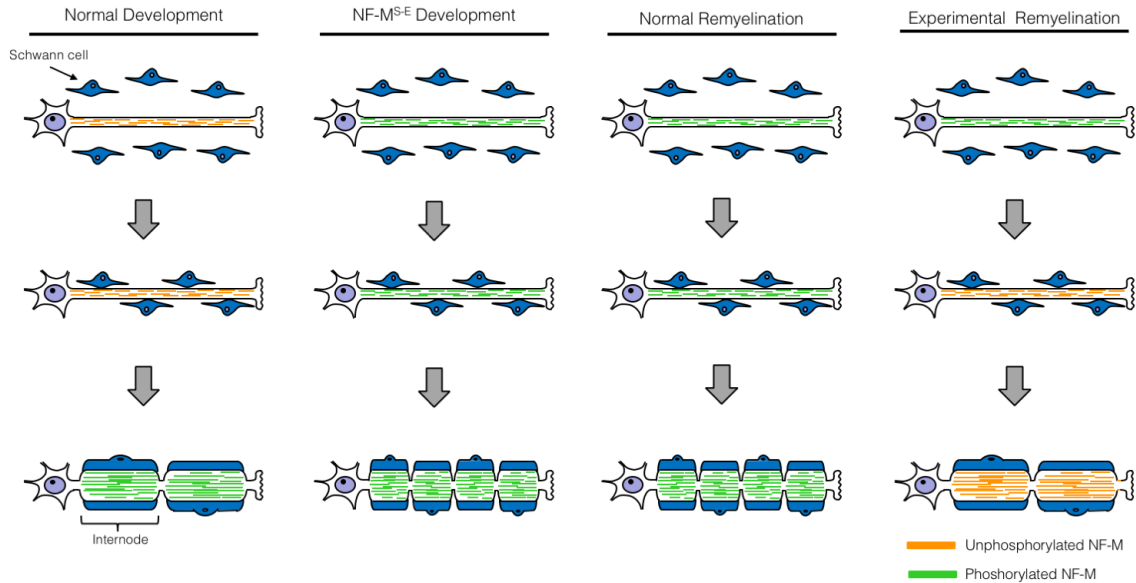


Fig. 5.2. Neurofilament medium phosphorylation prevents Schwann cell elongation during myelination. During normal myelination NF-M becomes phosphorylated after Schwann cells associate and elongate along axons allowing for the formation of normal internode lengths (Normal Myelination). Premature NF-M phosphorylation during normal development restricts Schwann cell elongation during myelination and results in abnormally short internode lengths (NF-M^{S→E} Development). Normal remyelination presents a similar scenario as NF-M^{S→E} myelination, where NF-M is in a phosphorylated state before the onset of myelination. Thus remyelination results in abnormally short internode lengths (Normal Remyelination). The data so far indicates that if NF-M phosphorylation is prevented during the process of remyelination, this would allow the normal elongation of Schwann cells and result in normal internodal lengths.

Although our data offer new insights into the mechanisms that control Schwann cell elongation during myelination, further analyses are needed to find the mechanism by which NF-M phosphorylation controls Schwann cell elongation. Currently, only one signaling mechanism has been described that involves an axonal protein influencing the behavior or development of Schwann cells. This is the neuregulin-1 type III signaling mechanism that controls the thickness of the myelin sheath (Michailov et al., 2004; Nave and Salzer, 2006; Taveggia et al., 2005). Perhaps, the phosphorylation of NF-M acts through a similar signaling mechanism as neuregulin-I type III by activating downstream signaling pathways. Formation of the node of Ranvier is marked by the clustering of Na_v^+ channels at the leading edge of the elongating Schwann cell (Feinberg et al., 2010). Gliomedin is a secreted molecule from the Schwann cells during myelination (Eshed et al., 2005). This molecule is released by the Schwann cell microvilli at the leading edge of the elongating Schwann cell during myelination (Eshed et al., 2005). Upon secretion by the elongating Schwann cell, gliomedin binds to neural cell adhesion molecule (NrcAM) on the Schwann cell microvilli and axonal neurofascin-186 (Eshed et al., 2005). This interaction induces the clustering of Na_v^+ channels (Eshed et al., 2005; Feinberg et al., 2010; Salzer et al., 2008). Gliomedin is only released by myelinating Schwann cells and it is necessary for the clustering of Na_v^+ channels (Eshed et al., 2005). The mechanisms that lead to the synthesis and release of gliomedin during myelination are not yet known. Perhaps the a mechanism by which phosphorylation of NF-M leads to shorter internode lengths, involves activating trans membrane signaling cascades across the axon-Schwann cell membranes, which leads to secretion of molecules like gliomedin, which are

necessary for the formation of node of Ranvier. However, further investigation to define the signaling mechanism is needed.

5.6. Final conclusions

Overall the findings of my research have important implications into development of potential therapeutic interventions to enhance recovery from demyelinating diseases of from nerve injuries. Reduced internodal lengths are observed in demyelinating diseases like CMT (Court et al., 2004; Saporta et al., 2009; Vizoso and Young, 1948), and multiple sclerosis (Lassmann et al., 1981; Prineas and Connell, 1979), which cause major alterations to nerve function (Court et al., 2004; Lassmann et al., 1981; Prineas and Connell, 1979; Saporta et al., 2009; Vizoso and Young, 1948). Moreover, after recovery from a nerve injury, internodal length is reduced relative to uninjured nerves (Gupta et al., 2012; Hildebrand et al., 1987; Vizoso and Young, 1948; Weiss and Hiscoe, 1948). Therefore, effective and full recovery from myelin loss includes the recovery of normal internode lengths. My results suggest that preventing NF-M C-terminus phosphorylation during de recovery period following demyelination will enhance Schwann cell elongation, thus resulting in significant recovery of internode lengths. Potential targets for intervention could be protein phosphatase 1 (Strack et al., 1997) and protein phosphatase 2A (Saito et al., 1995; Strack et al., 1997) as these phosphatases have been co-purified with neurofilament proteins and have been shown to dephosphorylate neurofilament proteins (Saito et al., 1995; Strack et al., 1997). Developing strategies for local delivery of small molecules that activate PP1 or PP2A could reduce neurofilament

phosphorylation levels in demyelinated axonal segments allowing for more efficient Schwann cell elongation and longer internodes during remyelination.

In summary, my dissertation has provided new insights into the understanding of CMT 2E disease pathogenesis. Sensory system functional and structural analyses demonstrate specific alterations in muscle spindle morphology, which are detectable prior to the onset of overt CMT phenotype. Given that CMT patients present with similar symptoms after the onset of neuropathy, my work identifies early proprioceptive sensory system alterations as a unifying hypothesis of disease pathogenesis in CMT. Moreover, my dissertation has provided insights into the functional consequences of a peripheral nerve injury superimposed on an underlying peripheral neuropathy like CMT.

Furthermore, my dissertation provides a molecular basis for an empirical observation that was first made over 70 years ago and provides new insights into the mechanism that regulates Schwann cell elongation during myelination. Thus providing a potential target for therapeutic intervention to promote full recovery from nerve injury or demyelinating diseases.

REFERENCES

- Abe, A., C. Numakura, K. Saito, H. Koide, N. Oka, A. Honma, Y. Kishikawa, and K. Hayasaka. 2009. Neurofilament light chain polypeptide gene mutations in Charcot-Marie-Tooth disease: nonsense mutation probably causes a recessive phenotype. *J Hum Genet.* 54:94-97.
- Achilli, F., V. Bros-Facer, H.P. Williams, G.T. Banks, M. AlQatari, R. Chia, V. Tucci, M. Groves, C.D. Nickols, K.L. Seburn, R. Kendall, M.Z. Cader, K. Talbot, J. van Minnen, R.W. Burgess, S. Brandner, J.E. Martin, M. Koltzenburg, L. Greensmith, P.M. Nolan, and E.M. Fisher. 2009. An ENU-induced mutation in mouse glycyl-tRNA synthetase (GARS) causes peripheral sensory and motor phenotypes creating a model of Charcot-Marie-Tooth type 2D peripheral neuropathy. *Disease models & mechanisms.* 2:359-373.
- Adebola, A.A., T. Di Castri, C.Z. He, L.A. Salvatierra, J. Zhao, K. Brown, C.S. Lin, H.J. Worman, and R.K. Liem. 2015. Neurofilament Light Polypeptide Gene N98S Mutation in Mice Leads to Neurofilament Network Abnormalities and a Charcot-Marie-Tooth Type 2E Phenotype. *Human molecular genetics.* 24:2163 - 2174.
- Akay, T. 2014. Long-term measurement of muscle denervation and locomotor behavior in individual wild-type and ALS model mice. *J Neurophysiol.* 111:694-703.
- Angeby-Moller, K., O.G. Berge, and F.P. Hamers. 2008. Using the CatWalk method to assess weight-bearing and pain behaviour in walking rats with ankle joint monoarthritis induced by carrageenan: effects of morphine and rofecoxib. *J Neurosci Methods.* 174:1-9.
- Arroyo, E.J., E.E. Sirkowski, R. Chitale, and S.S. Scherer. 2004. Acute demyelination disrupts the molecular organization of peripheral nervous system nodes. *J Comp Neurol.* 479:424-434.
- Augusto, V., C.R. Padovani, and G.E. Rocha Campos. 2004. Skeletal muscle fiber types in C57BL6J mice. *Braz J Morphol Sci.* 21:89 - 94.
- Barry, D.M., C. Carpenter, C. Yager, B. Golik, K.J. Barry, H. Shen, O. Mikse, L.S. Eggert, D.J. Schulz, and M.L. Garcia. 2010. Variation of the neurofilament medium KSP repeat sub-domain across mammalian species: implications for altering axonal structure. *The Journal of experimental biology.* 213:128-136.
- Barry, D.M., S. Millecamps, J.P. Julien, and M.L. Garcia. 2007. New movements in neurofilament transport, turnover and disease. *Experimental cell research.* 313:2110-2120.
- Barry, D.M., W. Stevenson, B.G. Bober, P.J. Wiese, J.M. Dale, G.S. Barry, N.S. Byers, J.D. Strope, R. Chang, D.J. Schulz, S. Shah, N.A. Calcutt, Y. Gebremichael, and

- M.L. Garcia. 2012. Expansion of neurofilament medium C terminus increases axonal diameter independent of increases in conduction velocity or myelin thickness. *J Neurosci.* 32:6209-6219.
- Battle, E., and D.G. Wilkinson. 2012. Molecular mechanisms of cell segregation and boundary formation in development and tumorigenesis. *Cold Spring Harbor perspectives in biology.* 4:a008227.
- Berciano, J., A. Garcia, K. Peeters, E. Gallardo, E. De Vriendt, A.L. Pelayo-Negro, J. Infante, and A. Jordanova. 2015. NEFL E396K mutation is associated with a novel dominant intermediate Charcot-Marie-Tooth disease phenotype. *J Neurol.* 262:1289-1300.
- Bhat, M. 2003. Molecular organization of axo-glia junctions. *Current opinion in neurobiology.* 13:552-559.
- Bird, T.D. 1993a. Charcot-Marie-Tooth Neuropathy Type 1. *In GeneReviews.* R.A. Pagon, T.D. Bird, C.R. Dolan, and K. Stephens, editors. Seattle, WA : University of Washington, Seattle (WA).
- Bird, T.D. 1993b. Charcot-Marie-Tooth Neuropathy Type 2. *In GeneReviews.* R.A. Pagon, T.D. Bird, C.R. Dolan, and K. Stephens, editors. Seattle, WA : University of Washington, Seattle (WA).
- Bird, T.D. 2016. Charcot-Marie-Tooth Neuropathy Type 2. *GeneReview Molecular Genetics: Less commonly involved genes.*
- Boiko, T., M.N. Rasband, S.R. Levinson, J.H. Caldwell, G. Mandel, J.S. Trimmer, and G. Matthews. 2001. Compact myelin dictates the differential targeting of two sodium channel isoforms in the same axon. *Neuron.* 30:91-104.
- Boillee, S., K. Yamanaka, C.S. Lobsiger, N.G. Copeland, N.A. Jenkins, G. Kassiotis, G. Kollias, and D.W. Cleveland. 2006. Onset and progression in inherited ALS determined by motor neurons and microglia. *Science.* 312:1389-1392.
- Bondan, E.F., P.R. Custodio, M.A. Lallo, H.D.L. Bentubo, and D.L. Graca. 2009. Ethidium bromide-induced demyelination in the sciatic nerve of diabetic rats. *Arg Neuropsiquiatr.* 67:1066 -1070.
- Bondan, E.F., and F. Monteiro Martins Mde. 2013. Cyclosporine improves remyelination in diabetic rats submitted to a gliotoxic demyelinating model in the brainstem. *Microscopy research and technique.* 76:714-722.
- Bongers, K.S., D.K. Fox, S.M. Ebert, S.D. Kunkel, M.C. Dyle, S.A. Bullard, J.M. Dierdorff, and C.M. Adams. 2013. Skeletal muscle denervation causes skeletal muscle atrophy through a pathway that involves both Gadd45a and HDAC4. *AJP: Endocrinology and Metabolism.* 305:E907-E915.

- Bouhy, D., and V. Timmerman. 2013. Animal models and therapeutic prospects for Charcot-Marie-Tooth disease. *Ann Neurol.* 74:391-396.
- Bozkurt, A., R. Deumens, J. Scheffel, D.M. O'Dey, J. Weis, E.A. Joosten, T. Fuhrmann, G.A. Brook, and N. Pallua. 2008. CatWalk gait analysis in assessment of functional recovery after sciatic nerve injury. *J Neurosci Methods.* 173:91-98.
- Brill, M.H., S.G. Waxman, J.W. Moore, and R.W. Joyner. 1977. Conduction velocity and spike configuration in myelinated fibers: computed dependence on internode distance. *Journal of Neurology, Neurosurgery & Psychiatry.* 40:769 - 774.
- Brill, V., R. Ellison, M. Ngo, B. Bergstrom, D. Raynard, and H. Gin. 1998. Electrophysiological monitoring in clinical trials. *Muscle Nerve.* 21:1368 - 1373.
- Britsch, S., D.E. Goerich, D. Riethmacher, R.I. Peirano, M. Rossner, K.A. Nave, C. Birchmeier, and M. Wegner. 2001. The transcription factor Sox10 is a key regulator of peripheral glial development. *Genes Dev.* 15:66-78.
- Brownlees, J., S. Ackerley, A.J. Grierson, N.J. Jacobsen, K. Shea, B.H. Anderton, P.N. Leigh, C.E. Shaw, and C.C. Miller. 2002. Charcot-Marie-Tooth disease neurofilament mutations disrupt neurofilament assembly and axonal transport. *Hum Mol Genet.* 11:2837-2844.
- Bunge, R.P., M.B. Bunge, and M. Bates. 1989. Movements of the Schwann Cell Nucleus Implicate Progression of the Inner (Axon-related) Schwann Cell Process During Myelination. *Journal of Cell Biology.* 109:273 - 284.
- Burke, R.E., P.L. Strick, K. Kanda, C.C. Kim, and B. Walmsley. 1977. Anatomy of medial gastrocnemius and soleus motor nuclei in cat spinal cord. *J Neurophysiol.* 40:667-680.
- Butinar, D., A. Starr, J. Zidar, P. Koutsou, and K. Christodoulou. 2008. Auditory nerve is affected in one of two different point mutations of the neurofilament light gene☆. *Clinical Neurophysiology.* 119:367-375.
- Cajal, S.R.y. 1928. Degeneration and regeneration of the nervous system. *Oxford Univeristy Press, London.*
- Calcutt, N.A. 2004. Modeling diabetic sensory neuropathy in rats. *Methods in molecular medicine.* 99:55-65.
- Carden, M.J., J.Q. Trojanowski, W.W. Schlaepfer, and V.M.-Y. Lee. 1987. Two-Stage expression of neurofilament polypeptides during rat neurogenesis with early establishment of adult phosphorylation patterns. *Journal of Neuroscience.* 7:3489-3504.
- Carter, R.J., L.A. Lione, T. Humby, L. Mangiarini, A. Mahal, G.P. Bates, S.B. Dunnett, and A.J. Morton. 1999. Characterization of progressive motor deficits in mice

transgenic for the human huntington's disease mutation. *The Journal of Neuroscience* 19:3248 - 3257.

- Casellini, C.M., and A.I. Vinik. 2007. Clinical manifestations and current treatment options for diabetic neuropathies. *Endocrinology Practice*. 13:550 - 566.
- Charcot, J.M., and P. Marie. 1886. Sur une forme particuliere d'atrophie musculaire progressive souvent familiale debutant par les pieds et les jambes et atteignant plus tard les mains. *Rev. Med. Paris*. 6:97-138.
- Chaudhry, V., M. Chaudhry, T.O. Crawford, E. Simmons-O'Brien, and J. Griffin. 2003. Toxic neuropathy in patients with pre-existing neuropathy. *Neurology*. 60:337 - 340.
- Chen, S., C. Rio, R.R. Ji, P. Dikkes, R.E. Coggeshall, C.J. Woolf, and G. Corfas. 2003. Disruption of ErbB receptor signaling in adult non-myelinating Schwann cells causes progressive sensory loss. *Nat Neurosci*. 6:1186-1193.
- Chen, Y.J., F.C. Cheng, M. Sheu, H.L. Su, C.J. Chen, J. Sheehan, and H.C. Pan. 2014. Detection of subtle neurological alterations by the Catwalk XT gait analysis system. *Journal of NeuroEngineering and Rehabilitation*. 11.
- Choi, B.O., M.S. Lee, S.H. Shin, J.H. Hwang, K.G. Choi, W.K. Kim, I.N. Sunwoo, N.K. Kim, and K.W. Chung. 2004. Mutational analysis of PMP22, MPZ, GJB1, EGR2 and NEFL in Korean Charcot-Marie-Tooth neuropathy patients. *Human mutation*. 24:185-186.
- Clark, B.C. 2009. In vivo alterations in skeletal muscle form and function after disuse atrophy. *Med Sci Sports Exerc*. 41:1869-1875.
- Clement, A.M., M.D. Nguyen, E.A. Roberts, M.L. Garcia, S. Boillee, M. Rule, A.P. McMahon, W. Doucette, D. Siwek, R.J. Ferrante, R.H. Brown, Jr., J.P. Julien, L.S. Goldstein, and D.W. Cleveland. 2003. Wild-type nonneuronal cells extend survival of SOD1 mutant motor neurons in ALS mice. *Science*. 302:113-117.
- Cleveland, D.W. 1996. Neuronal Growth and Death: Order and Disorder in the Axoplasm. *Cell*. 84:663 - 666.
- Cochard, P., and D. Paulin. 1984. Initial expression of neurofilaments and vimentin in the central and peripheral nervous system of the mouse embryo *in vivo*. *Journal of Neuroscience*. 4:2080-2094.
- Cole, J.S., A. Messing, J.Q. Trojanowski, and V.M. Lee. 1994. Modulation of axon diameter and neurofilaments by hypomyelinating Schwann cells in transgenic mice. *J Neurosci*. 14:6956-6966.

- Court, F.A., D.L. Sherman, T. Pratt, E.M. Garry, R.R. Ribchester, D.F. Cottrell, S.M. Fleetwood-Walker, and P.J. Brophy. 2004. Restricted growth of Schwann cells lacking Cajal bands slows conduction in myelinated nerves. *Nature*. 432:191-195.
- Craner, M.J., J. Newcombe, J.A. Black, C. Hartle, M.L. Cuzner, and S.G. Waxman. 2004. Molecular changes in neurons in multiple sclerosis: altered axonal expression of Nav1.2 and Nav1.6 sodium channels and Na⁺/Ca²⁺ exchanger. *Proc Natl Acad Sci U S A*. 101:8168-8173.
- d'Ydewalle, C., J. Krishnan, D.M. Chiheb, P. Van Damme, J. Irobi, A.P. Kozikowski, P. Vanden Berghe, V. Timmerman, W. Robberecht, and L. Van Den Bosch. 2011. HDAC6 inhibitors reverse axonal loss in a mouse model of mutant HSPB1-induced Charcot-Marie-Tooth disease. *Nat Med*. 17:968-974.
- Dale, J.M., and M.L. Garcia. 2012. Neurofilament Phosphorylation during Development and Disease: Which Came First, the Phosphorylation or the Accumulation? *Journal of amino acids*. 2012:382107.
- Dale, J.M., E. Villalon, S.G. Shannon, D.M. Barry, R.M. Markey, V.B. Garcia, and M.L. Garcia. 2012. Expressing hNF-LE397K results in abnormal gaiting in a transgenic model of CMT2E. *Genes, brain, and behavior*. 11:360-365.
- De Jonghe, P., and A.K. Jordanova. 1993. Charcot-Marie-Tooth Neuropathy Type 2E/1F. *In GeneReviews*. R.A. Pagon, T.D. Bird, C.R. Dolan, and K. Stephens, editors, Seattle (WA).
- De Jonghe, P., I. Mersivanova, E. Nelis, J. Del Favero, J.J. Martin, C. Van Broeckhoven, O. Evgrafov, and V. Timmerman. 2001. Further evidence that neurofilament light chain gene mutations can cause Charcot-Marie-Tooth disease type 2E. *Ann Neurol*. 49:245-249.
- de Waegh, S.M., V.M.-Y. Lee, and S.T. Brady. 1992. Local modulation of neurofilament phosphorylation, axonal caliber, and slow axonal transport by myelinating schwann cells. *Cell*. 68:451-463.
- Dequen, F., M. Filali, R.C. Lariviere, R. Perrot, S. Hisanaga, and J.P. Julien. 2010. Reversal of neuropathy phenotypes in conditional mouse model of Charcot-Marie-Tooth disease type 2E. *Human molecular genetics*. 19:2616-2629.
- Devor, M., and R. Govrin-Lippmann. 1979. Maturation of axonal sprouts after nerve crush. *Exp Neurol*. 64:260-270.
- Donaldson, H.H., and G.W. Hoke. 1905. On the areas of the axis cylinder and medullary sheath as seen in cross sections of the spinal nerves of vertebrates. *Journal of Comparative Neurology*. 15:1 -16.

- Dong, Z., A. Sinanan, D. Parkinson, E. Parmantier, R. Mirsky, and K.R. Jessen. 1999. Schwann Cell Development in Embryonic Mouse Nerves. *Journal of Neuroscience*. 56:334-348.
- Dugandzija-Novakovic, S., A.G. Koszowski, S.R. Levinson, and P. Shrager. 1995. Clustering of Na⁺ channels and node of Ranvier formation in remyelinating axons. *J Neurosci*. 15:492-503.
- Elder, G.A., V.L. Friedrich, Jr., P. Bosco, C. Kang, A. Gourov, P.H. Tu, V.M. Lee, and R.A. Lazzarini. 1998a. Absence of the mid-sized neurofilament subunit decreases axonal calibers, levels of light neurofilament (NF-L), and neurofilament content. *Journal of Cell Biology*. 141:727-739.
- Elder, G.A., V.L. Friedrich, Jr., C. Kang, P. Bosco, A. Gourov, P.-H. Tu, B. Zhang, V.M.-Y. Lee, and R.A. Lazzarini. 1998b. Requirement of Heavy Neurofilament Subunit in the Development of Axons with Large Calibers. *Journal of Cell Biology*. 143:195 - 205.
- Elsohemy, A., R. Butler, J.R. Bain, and M. Fahnstock. 2009. Sensory protection of rat muscle spindles following peripheral nerve injury and reinnervation. *Plast Reconstr Surg*. 124:1860-1868.
- Emery, A.E. 1991. Population frequencies of inherited neuromuscular diseases--a world survey. *Neuromuscular disorders : NMD*. 1:19-29.
- Eshed, Y., K. Feinberg, D.J. Carey, and E. Peles. 2007. Secreted gliomedin is a perinodal matrix component of peripheral nerves. *J Cell Biol*. 177:551-562.
- Eshed, Y., K. Feinberg, S. Poliak, H. Sabanay, O. Sarig-Nadir, I. Spiegel, J.R. Bermingham, Jr., and E. Peles. 2005. Gliomedin mediates Schwann cell-axon interaction and the molecular assembly of the nodes of Ranvier. *Neuron*. 47:215-229.
- Eyer, J., and A. Peterson. 1994. Neurofilament-deficient axons and perikaryal aggregates in viable transgenic mice expressing a neurofilament-beta-galactosidase fusion protein. *Neuron*. 12:389-405.
- Fabrizi, G.M., T. Cavallaro, C. Angiari, L. Bertolasi, I. Cabrini, M. Ferrarini, and N. Rizzuto. 2004. Giant axon and neurofilament accumulation in Charcot-Marie-Tooth disease type 2E. *Neurology*. 62:1429-1431.
- Fabrizi, G.M., T. Cavallaro, C. Angiari, I. Cabrini, F. Taioli, G. Malerba, L. Bertolasi, and N. Rizzuto. 2007. Charcot-Marie-Tooth disease type 2E, a disorder of the cytoskeleton. *Brain*. 130:394-403.
- Feinberg, K., Y. Eshed-Eisenbach, S. Frechter, V. Amor, D. Salomon, H. Sabanay, J.L. Dupree, M. Grumet, P.J. Brophy, P. Shrager, and E. Peles. 2010. A glial signal

consisting of gliomedin and NrCAM clusters axonal Na⁺ channels during the formation of nodes of Ranvier. *Neuron*. 65:490-502.

- Fernandez-Valle, C., R.P. Bunge, and M.B. Bunge. 1995. Schwann cells degrade myelin and proliferate in the absence of macrophages: evidence from in vitro studies of Wallerian degeneration. *Journal of neurocytology*. 24:667-679.
- Filali, M., F. Dequen, R. Lalonde, and J.P. Julien. 2011. Sensorimotor and cognitive function of a NEFL(P22S) mutant model of Charcot-Marie-Tooth disease type 2E. *Behav Brain Res*. 219:175-180.
- Fricker, F.R., A. Antunes-Martins, J. Galino, R. Paramsothy, F. La Russa, J. Perkins, R. Goldberg, J. Brelstaff, N. Zhu, S.B. McMahon, C. Orengo, A.N. Garratt, C. Birchmeier, and D.L. Bennett. 2013. Axonal neuregulin 1 is a rate limiting but not essential factor for nerve remyelination. *Brain*. 136:2279-2297.
- Fridman, V., B. Bundy, M.M. Reilly, D. Pareyson, C. Bacon, J. Burns, J. Day, S. Feely, R.S. Finkel, T. Grider, C.A. Kirk, D.N. Herrmann, M. Laura, J. Li, T. Lloyd, C.J. Sumner, F. Muntoni, G. Piscoquito, S. Ramchandren, R. Shy, C.E. Siskind, S.W. Yum, I. Moroni, E. Pagliano, S. Zuchner, S.S. Scherer, M.E. Shy, and C. Inherited Neuropathies. 2015. CMT subtypes and disease burden in patients enrolled in the Inherited Neuropathies Consortium natural history study: a cross-sectional analysis. *Journal of neurology, neurosurgery, and psychiatry*. 86:873-878.
- Friede, R.L., and T. Samorajski. 1970. Axon caliber related to neurofilaments and microtubules in sciatic nerve fibers of rats and mice. *Anat Rec*. 167:379-387.
- Friese, A., J.A. Kaltschmidt, D.R. Ladle, M. Sigrist, T.M. Jessell, and S. Arber. 2009. Gamma and alpha motor neurons distinguished by expression of transcription factor *Err3*. *Proc Natl Acad Sci U S A*. 106:13588-13593.
- Fu, S.Y., and T. Gordon. 1997. The cellular and molecular basis of peripheral nerve regeneration. *Molecular neurobiology*. 14:67-116.
- Fuchs, E., and D.W. Cleveland. 1998. A Structural Scaffolding of Intermediate Filaments in Health and Disease. *Science*. 279:514-519.
- Fuchs, E., and C. Weber. 1994. Intermediate filaments: Structure, dynamics, function, and disease. *Annu Rev Biochem*. 63:345-382.
- Gabriel, A.F., M.A. Marcus, W.M. Honig, G.H. Walenkamp, and E.A. Joosten. 2007. The CatWalk method: a detailed analysis of behavioral changes after acute inflammatory pain in the rat. *J Neurosci Methods*. 163:9-16.
- Gabriel, A.F., M.A. Marcus, G.H. Walenkamp, and E.A. Joosten. 2009. The CatWalk method: assessment of mechanical allodynia in experimental chronic pain. *Behav Brain Res*. 198:477-480.

- Ganesalingam, J., J. An, R. Bowser, P.M. Andersen, and C.E. Shaw. 2012. pNfH is a promising biomarker for ALS. *Amyotrophic Lateral Sclerosis and Frontotemporal Degeneration*. 14:146-149.
- Ganesalingam, J., J. An, C.E. Shaw, G. Shaw, D. Lacomis, and R. Bowser. 2011. Combination of neurofilament heavy chain and complement C3 as CSF biomarkers for ALS. *J Neurochem*. 117:528-537.
- Garcia, M.L., C.S. Lobsiger, S.B. Shah, T.J. Deerinck, J. Crum, D. Young, C.M. Ward, T.O. Crawford, T. Gotow, Y. Uchiyama, M.H. Ellisman, N.A. Calcutt, and D.W. Cleveland. 2003. NF-M is an essential target for the myelin-directed "outside-in" signaling cascade that mediates radial axonal growth. *The Journal of Cell Biology*. 163:1011-1020.
- Garcia, M.L., M.V. Rao, J. Fujimoto, V.B. Garcia, S.B. Shah, J. Crum, T. Gotow, Y. Uchiyama, M. Ellisman, N.A. Calcutt, and D.W. Cleveland. 2009. Phosphorylation of highly conserved neurofilament medium KSP repeats is not required for myelin-dependent radial axonal growth. *J Neurosci*. 29:1277-1284.
- Gentile, L., F. Taioli, G.M. Fabrizi, M. Russo, C. Stancanelli, and A. Mazzeo. 2013. Considerable post-partum worsening in a patient with CMT2E. *Neurological sciences : official journal of the Italian Neurological Society and of the Italian Society of Clinical Neurophysiology*. 34:1813-1814.
- Georgiou, D.M., J. Zidar, M. Korosec, L.T. Middleton, T. Kyriakides, and K. Christodoulou. 2002. A novel NF-L mutation Pro22Ser is associated with CMT2 in a large Slovenian family. *Neurogenetics*. 4:93-96.
- Gilbert, D.S. 1975. Axoplasm architecture and physical properties as seen in the myxicola giant axon. *J. Physiol*. 253:257 - 301.
- Gill, S.R., P.C. Wong, M.J. Monteiro, and D.W. Cleveland. 1990. Assembly properties of dominant and recessive mutations in the small mouse neurofilament (NF-L) subunit. *J Cell Biol*. 111:2005-2019.
- Gillespie, C.S., D.L. Sherman, S.M. Fleetwood-Walker, D.F. Cottrell, S. Tait, E.M. Garry, V.C. Wallace, J. Ure, I.R. Griffiths, A. Smith, and P.J. Brophy. 2000. Peripheral demyelination and neuropathic pain behavior in periaxin-deficient mice. *Neuron*. 26:523-531.
- Gilman, S. 2002. Joint position sense and vibration sense: anatomical organisation and assessment. *Journal of neurology, neurosurgery, and psychiatry*. 73:473-477.
- Gledhill, R.F., B.M. Harrison, and W.I. McDonald. 1973. Pattern of remyelination in the CNS. *Nature*. 244:443 - 444.
- Gleich, O., and S. Wilson. 1993. The diameters of guinea pig auditory nerve fibres: distribution and correlation with spontaneous rate. *Hear Res*. 71:69-79.

- Goldman, L., and J.S. Albus. 1968. Computation of impulse conduction in myelinated fibers; theoretical basis of the velocity-diameter relation. *Biophys J.* 8:596-607.
- Gordon, T., and R.B. Stein. 1982a. Reorganization of motor-unit properties in reinnervated muscles of the cat. *J Neurophysiol.* 48:1175 - 1190.
- Gordon, T., and R.B. Stein. 1982b. Time course and extent of recovery in reinnervated motor units of cat triceps surae muscles. *J. Physiol.* 323:307 - 323.
- Gupta, R., N. Nassiri, A. Hazel, M. Bathen, and T. Mozaffar. 2012. Chronic nerve compression alters Schwann cell myelin architecture in a murine model. *Muscle Nerve.* 45:231-241.
- Hagedorn, L., U. Suter, and L. Sommer. 1999. P0 and PMP22 mark a multipotent neural crest-derived cell type that displays community effects in response to TGF-beta family factors. *Development.* 126:3781-3794.
- Hamers, F.P., A.J. Lankhorst, T.J.V. Laar, W.B. Veldhuis, and W.H. Gispen. 2001. Automated Quantitative Gait Analysis During Overground Locomotion in the Rat: Its Application to Spinal Cord Contusion and Transection Injuries. *J Neurotrauma.* 18:187-209.
- Hardy, W.L. 1971. Computed Dependence of Conduction Speed in Myelinated Axons on Geometric Parameters. *Biophys. Society Abstracts.* 11:238a.
- Hargreaves, K., R. Dubner, F. Brown, C. Flores, and J. Joris. 1988. A new and sensitive method for measuring thermal nociception in cutaneous hyperalgesia. *Pain.* 32:77-88.
- Harris, J., C. Ayyub, and G. Shaw. 1991. A molecular dissection of the carboxyterminal tails of the major neurofilament subunits NF-M and NF-H. *J Neurosci Res.* 30:47-62.
- Heins, S., P.C. Wong, S. Muller, K. Goldie, D.W. Cleveland, and U. Aebi. 1993. The rod domain of NF-L determines neurofilament architecture, whereas the end domains specify filament assembly and network formation. *J Cell Biol.* 123:1517-1533.
- Hildebrand, C., E. Holler, M. Woenkhaus, G. Quarch, A. Reichle, B. Schalke, and R. Andreessen. 2000. Acute deterioration of Charcot-Marie-Tooth disease IA (CMT IA) following 2mm of vincristine chemotherapy. *Annals of Oncology.* 11:743 - 747.
- Hildebrand, C., J.D. Kocsis, S. Berglund, and S.G. Waxman. 1985. Myelin sheath remodelling in regenerated rat sciatic nerve. *Brain Res.* 358:163-170.
- Hildebrand, C., G.Y. Mustafa, C. Bowe, and J.D. Kocsis. 1987. Nodal spacing along regenerated axons following a crush lesion of the developing rat sciatic nerve. *Developmental Brain Research.* 32:147 - 154.

- Hirano, A., I. Nakano, L.T. Kurland, D.W. Mulder, P.W. Holley, and G. Saccomanno. 1984. Fine structural study of neurofibrillary changes in a family with amyotrophic lateral sclerosis. *Journal of Neuropathology and Experimental Neurology*. 43:471 - 480.
- Hirokawa, N., M.A. Glicksman, and M.B. Willard. 1984. Organization of mammalian neurofilament polypeptides within the neuronal cytoskeleton. *J Cell Biol*. 98:1523-1536.
- Hodes, R. 1953. Linear relationship between fiber diameter and velocity of conduction in giant axon of squid. *J Neurophysiology*. 16:145 - 154.
- Hodgkin, A.L., and A.F. Huxley. 1945. Resting and action potentials in single nerve fibers. *J. Physiol*. 104:176-195.
- Hoffman, P.N., J. Griffin, and D.J. Price. 1984. Control of axonal caliber by neurofilament transport. *Journal of Cell Biology*. 99:705 - 714.
- Hsieh, S.T., G.J. Kidd, T.O. Crawford, Z. Xu, W.M. Lin, B.D. Trapp, D.W. Cleveland, and J.W. Griffin. 1994. Regional modulation of neurofilament organization by myelination in normal axons. *J Neurosci*. 14:6392-6401.
- Hunt, C.C., and S.W. Kuffler. 1951. Further study of efferent small-nerve fibers to mammalian muscle spindles; multiple spindle innervation and activity during contraction. *J Physiol*. 113:283-297.
- Hursh, J.B. 1939. Conduction velocity and diameter of nerve fibers. *American J. Phys.*:131-139.
- Huxley, A.F., and R. Stampfli. 1949. Evidence for saltatory conduction in peripheral myelinated nerve fibers. *J Physiol*. 108:315-339.
- Jackson, J.R., T.J. Kirby, C.S. Fry, R.L. Cooper, J.J. McCarthy, C.A. Peterson, and E.E. Dupont-Versteegden. 2015. Reduced voluntary running performance is associated with impaired coordination as a result of muscle satellite cell depletion in adult mice. *Skeletal Muscle*. 5.
- Jacobs, J.M. 1988. On internodal length. *J. Anat*. 157:153 - 162.
- Jacomy, H., Q. Zhu, S. Couillard-Despres, J.M. Beaulieu, and J.P. Julien. 1999. Disruption of type IV intermediate filament network in mice lacking the neurofilament medium and heavy subunits. *J Neurochem*. 73:972-984.
- Jager, S.B., G. Ronchi, C.B. Vaegter, and S. Geuna. 2014. The mouse median nerve experimental model in regenerative research. *BioMed research international*. 2014:701682.

- Jessen, K.R., and R. Mirsky. 2005. The origin and development of glial cells in peripheral nerves. *Nat Rev Neurosci.* 6:671-682.
- Jessen, K.R., L. Morgan, H.J.S. Stewart, and R. Mirsky. 1990. Three markers of adult non-myelin-forming Schwann cells, 217c(Ran-1), A5E3 and GFAP: development and regulation by neuron-Schwann cell interactions. *Development.* 109:91-103.
- Jolival, C.G., L.M. Mizisin, A. Nelson, J.M. Cunha, K.M. Ramos, D. Bonke, and N.A. Calcutt. 2009. B vitamins alleviate indices of neuropathic pain in diabetic rats. *Eur J Pharmacol.* 612:41-47.
- Jones, M.R., E. Villalon, and M.L. Garcia. 2016. Genetic Manipulation of Neurofilament Protein Phosphorylation. *Methods Enzymol.* 568:461-476.
- Jordanova, A. 2003. Mutations in the neurofilament light chain gene (NEFL) cause early onset severe Charcot-Marie-Tooth disease. *Brain.* 126:590-597.
- Joyner, A.L. 1994. Gene Targeting. A Practical Approach. *Die Nahrung.* 38.
- Julien, J.P., and W.E. Mushynski. 1982. Multiple phosphorylation sites in mammalian neurofilament polypeptides. *J Biol Chem.* 257:10467-10470.
- Julien, J.P., and W.E. Mushynski. 1983. The distribution of phosphorylation sites among identified proteolytic fragments of mammalian neurofilaments. *J Biol Chem.* 258:4019-4025.
- Kandel, E.R., J.H. Schwartz, and T.M. Jessell. 2000. Principles of Neural Science.
- Kawamura, Y., H. Okazaki, P.C. O'Brien, and P.J. Dych. 1977. Lumbar motoneurons of man: I) number and diameter histogram of alpha and gamma axons of ventral root. *J Neuropathol Exp Neurol.* 36:853-860.
- Key, A., and G. Retzius. 1875. Studien in der Anatomie des Nervensystems und des Bindegewebe. *Samson and Wallin, Stockholm.* 2:228.
- Kloos, A.D., L.C. Fisher, M.R. Detloff, D.L. Hassenzahl, and D.M. Basso. 2005. Stepwise motor and all-or-none sensory recovery is associated with nonlinear sparing after incremental spinal cord injury in rats. *Exp Neurol.* 191:251-265.
- Koles, Z.J., and M. Rasminski. 1972. A computer simulation of conduction in demyelinated nerve fibers. *J Physiol.* 227:351-364.
- Kriz, J., Q. Zhu, J.P. Julien, and A.L. Padjen. 2000. Electrophysiological properties of axons in mice lacking neurofilament subunit genes: disparity between conduction velocity and axon diameter in absence of NF-H. *Brain Res.* 885:32-44.
- Lascelles, R.G., and P.K. Thomas. 1966. Changes due to age in internodal length in the sural nerve in man. *Journal of Neurology, Neurosurgery & Psychiatry.* 29:40-44.

- Lassmann, H., H. Budka, and G. Schnaberth. 1981. Inflammatory demyelinating polyradiculitis in a patient with multiple sclerosis. *Arch Neurol.* 38:99 - 102.
- Lee, M., A. Brennan, A. Blanchard, G. Zoidl, Z. Dong, A. Taberero, C. Zoidl, M.A. Dent, K.R. Jessen, and R. Mirsky. 1997. P0 is constitutively expressed in the rat neural crest and embryonic nerves and is negatively and positively regulated by axons to generate non-myelin-forming and myelin-forming Schwann cells, respectively. *Mol Cell Neurosci.* 8:336-350.
- Lee, M.K., Z. Xu, P.C. Wong, and D.W. Cleveland. 1993. Neurofilaments are obligate heteropolymers in vivo. *J. Cell Biology.* 122:1337-1350.
- Lee, S., and T.B. Shea. 2014. The high molecular weight neurofilament subunit plays an essential role in axonal outgrowth and stabilization. *Biology open.* 3:974-981.
- Lee, S.M., D. Sha, A.A. Mohammed, S. Asress, J.D. Glass, L.S. Chin, and L. Li. 2013. Motor and sensory neuropathy due to myelin infolding and paranodal damage in a transgenic mouse model of Charcot-Marie-Tooth disease type 1C. *Hum Mol Genet.* 22:1755-1770.
- Lepicard, E.M., P. Venault, J. Negroni, F. Perez-Diaz, C. Joubert, M. Nosten-Bertrand, A. Berthoz, and G. Chapouthier. 2003. Posture and balance responses to a sensory challenge are related to anxiety in mice. *Psychiatry Research.* 118:273-284.
- Leung, C.L., N. Nagan, T.H. Graham, and R.K. Liem. 2006. A novel duplication/insertion mutation of NEFL in a patient with Charcot-Marie-Tooth disease. *American journal of medical genetics. Part A.* 140:1021-1025.
- Ling, K.K., R.M. Gibbs, Z. Feng, and C.P. Ko. 2012. Severe neuromuscular denervation of clinically relevant muscles in a mouse model of spinal muscular atrophy. *Hum Mol Genet.* 21:185-195.
- Lobsiger, C.S., S. Boillee, and D.W. Cleveland. 2007. Toxicity from different SOD1 mutants dysregulates the complement system and the neuronal regenerative response in ALS motor neurons. *Proc Natl Acad Sci U S A.* 104:7319-7326.
- Martino, M.A., E. Miller, and E.C. Grendys, Jr. 2005. The administration of chemotherapy in a patient with Charcot-Marie-Tooth and ovarian cancer. *Gynecologic oncology.* 97:710-712.
- Medhurst, S.J., K. Walker, M. Bowes, B.L. Kidd, M. Glatt, M. Muller, M. Hattenberger, J. Vaxelaire, T. O'Reilly, G. Wotherspoon, J. Winter, J. Green, and L. Urban. 2002. A rat model of bone cancer pain. *Pain.* 96:129-140.
- Mersiyanova, I.V., A.V. Perepelov, A.V. Polyakov, V.F. Sitnikov, E.L. Dadali, R.B. Oparin, A.N. Petrin, and O.V. Evgrafov. 2000. A new variant of Charcot-Marie-Tooth disease type 2 is probably the result of a mutation in the neurofilament-light gene. *American journal of human genetics.* 67:37-46.

- Michailov, G.V., M.W. Sereda, B.G. Brinkmann, T.M. Fischer, B. Haug, C. Birchmeier, L. Role, C. Lai, M.H. Schwab, and K.A. Nave. 2004. Axonal neuregulin-1 regulates myelin sheath thickness. *Science*. 304:700-703.
- Miltenberger-Miltenyi, G., A.R. Janecke, J.V. Wanschitz, V. Timmerman, C. Windpassinger, M. Auer-Grumbach, and W.N. Loscher. 2007. Clinical and electrophysiological features in Charcot-Marie-Tooth disease with mutations in the NEFL gene. *Arch Neurol*. 64:966-970.
- Min, S.S., J.S. Han, Y.I. Kim, H.S. Na, Y.W. Yoon, S.K. Hong, and H.C. Han. 2001. A novel method for convenient assessment of arthritic pain in voluntarily walking rats. *Neurosci Lett*. 308:95 - 98.
- Mirsky, R., C. Dubois, L. Morgan, and K.R. Jessen. 1990. 04 and A007-sulfatide antibodies bind to embryonic Schwann cells prior to the appearance of galactocerebroside; regulation of antigen by axon-Schwann cell signals and cyclic AMP. *Development*. 109:105-116.
- Mirsky, R., A. Woodhoo, D. Parkinson, P. Arthur-Farraj, A. Bhaskaran, and K.R. Jessen. 2008. Novel signals controlling embryonic Schwann cell development, myelination and dedifferentiation. *J Peripher Nerv Syst*. 13:122 - 135.
- Moore, J.W., R.W. Joyner, M.H. Brill, S.D. Waxman, and M. Najjar-Joa. 1978. Simulations of conduction in uniform myelinated fibers.
- Muller, K.A., J.M. Ryals, E.L. Feldman, and D.E. Wright. 2008. Abnormal muscle spindle innervation and large-fiber neuropathy in diabetic mice. *Diabetes*. 57:1693-1701.
- Murray, L.M., L.H. Comley, D. Thomson, N. Parkinson, K. Talbot, and T.H. Gillingwater. 2008. Selective vulnerability of motor neurons and dissociation of pre- and post-synaptic pathology at the neuromuscular junction in mouse models of spinal muscular atrophy. *Hum Mol Genet*. 17:949-962.
- Nakagawa, T., J. Chen, Z. Zhang, Y. Kanai, and N. Hirokawa. 1995. Two distinct functions of the carboxyl-terminal tail domain of NF-M upon neurofilament assembly: cross-bridge formation and longitudinal elongation of filaments. *J Cell Biol*. 129:411-429.
- Nave, K.-A., and J.L. Salzer. 2006. Axonal regulation of myelination by neuregulin 1. *Current opinion in neurobiology*. 16:492-500.
- Ohara, O., Y. Gahara, T. Miyake, H. Teraoka, and T. Kitamura. 1993. Neurofilament deficiency in quail caused by nonsense mutation in neurofilament-L gene. *J. Cell Biology*. 121:387-395.
- Pachter, J.S., and R.K. Liem. 1984. The differential appearance of neurofilament triplet polypeptides in the developing rat optic nerve. *Dev Biol*. 103:200-210.

- Pareyson, D., and C. Marchesi. 2009. Diagnosis, natural history, and management of Charcot-Marie-Tooth disease. *Lancet Neurol.* 8:654-667.
- Pareyson, D., V. Scaiola, and M. Laurà. 2006. Clinical and electrophysiological aspects of Charcot-Marie-Tooth disease. *Neuromolecular Med.* 8:3-22.
- Patzko, A., and M.E. Shy. 2011. Update on Charcot-Marie-Tooth disease. *Current neurology and neuroscience reports.* 11:78-88.
- Perez-Olle, R., S.T. Jones, and R.K. Liem. 2004. Phenotypic analysis of neurofilament light gene mutations linked to Charcot-Marie-Tooth disease in cell culture models. *Human molecular genetics.* 13:2207-2220.
- Perez-Olle, R., C.L. Leung, and R.K. Liem. 2002. Effects of Charcot-Marie-Tooth-linked mutations of the neurofilament light subunit on intermediate filament formation. *J Cell Sci.* 115:4937-4946.
- Perez-Olle, R., M.A. Lopez-Toledano, D. Goryunov, N. Cabrera-Poch, L. Stefanis, K. Brown, and R.K. Liem. 2005. Mutations in the neurofilament light gene linked to Charcot-Marie-Tooth disease cause defects in transport. *J Neurochem.* 93:861-874.
- Perkin, O., P. McGuigan, D. Thompson, and K. Stokes. 2015. A reduced activity model: a relevant tool for the study of ageing muscle. *Biogerontology.* 17:435-447.
- Perrot, R., R. Berges, A. Bocquet, and J. Eyer. 2008. Review of the multiple aspects of neurofilament functions, and their possible contribution to neurodegeneration. *Molecular neurobiology.* 38:27-65.
- Perry, V.H., J.W. Tsao, S. Fearn, and M.C. Brown. 1995. Radiation-induced reductions in macrophage recruitment have only slight effects on myelin degeneration in sectioned peripheral nerves of mice. *Eur J Neurosci.* 7:271-280.
- Prineas, J.W., and F. Connell. 1979. Remyelination in multiple sclerosis. *Ann Neurol.* 5:22-31.
- Qi, Y., J.K. Wang, M. McMillian, and D.M. Chikaraishi. 1997. Characterization of a CNS cell line, CAD, in which morphological differentiation is initiated by serum deprivation. *J Neurosci.* 17:1217-1225.
- Rammensee, S., P.A. Janmey, and A.R. Bausch. 2007. Mechanical and structural properties of in vitro neurofilament hydrogels. *European biophysics journal : EBJ.* 36:661-668.
- Ranvier, L. 1872. Des étranglements annulaires et des segments interannulaires chez les Raies et les Torpilles. *Compte rendu de l'Académie des sciences.* 75:1129 - 1132.

- Rao, M.V., J. Campbell, A. Yuan, A. Kumar, T. Gotow, Y. Uchiyama, and R.A. Nixon. 2003. The neurofilament middle molecular mass subunit carboxyl-terminal tail domains is essential for the radial growth and cytoskeletal architecture of axons but not for regulating neurofilament transport rate. *The Journal of cell biology*. 163:1021-1031.
- Rao, M.V., L.J. Engle, P.S. Mohan, A. Yuan, D. Qiu, A. Cataldo, L. Hassinger, S. Jacobsen, V.M. Lee, A. Andreadis, J.P. Julien, P.C. Bridgman, and R.A. Nixon. 2002a. Myosin Va binding to neurofilaments is essential for correct myosin Va distribution and transport and neurofilament density. *The Journal of Cell Biology*. 159:279-290.
- Rao, M.V., M.L. Garcia, Y. Miyazaki, T. Gotow, A. Yuan, S. Mattina, C.M. Ward, N.A. Calcutt, Y. Uchiyama, R.A. Nixon, and D.W. Cleveland. 2002b. Gene replacement in mice reveals that the heavily phosphorylated tail of neurofilament heavy subunit does not affect axonal caliber or the transit of cargoes in slow axonal transport. *The Journal of Cell Biology*. 158:681-693.
- Rao, M.V., M.K. Houseweart, T.L. Williamson, T.O. Crawford, J. Folmer, and D.W. Cleveland. 1998. Neurofilament-dependent radial growth of motor axons and axonal organization of neurofilaments does not require the neurofilament heavy subunit (NF-H) or its phosphorylation. *The Journal of Cell Biology*. 143:171-181.
- Rasminski, M., and T.A. Sears. 1972. Internodal conduction in undissected demyelinated nerve fibers. *J Physiol*. 227:323-350.
- Reichert, F., A. Saada, and S. Rotshenker. 1994. Peripheral nerve injury induces Schwann cells to express two macrophage phenotypes: phagocytosis and the galactose-specific lectin MAC-2. *J Neurosci*. 14:3231-3245.
- Riet-Correa, G., C.G. Fernandes, L.A.V. Pereira, and D.L. Graca. 2002. Ethidium bromide-induced demyelination of the sciatic nerve of adult Wistar rats. *Braz J Med Biol Res*. 35:99 -104.
- Ronchi, G., S. Raimondo, A.S. Varejao, P. Tos, I. Perroteau, and S. Geuna. 2010. Standardized crush injury of the mouse median nerve. *J Neurosci Methods*. 188:71-75.
- Rushton, W.A.H. 1951. A theory of the effects of fibre size in medullated nerve. *J Physiol*. 115:101-122.
- Saito, T., H. Shima, Y. Osawa, M. Nagao, B.A. Hemmings, T. Kishimoto, and S. Hisanaga. 1995. Neurofilament-associated protein phosphatase 2A: its possible role in preserving neurofilaments in filamentous states. *Biochemistry*. 34:7376-7384.

- Sakaguchi, T., M. Okada, T. Kitamura, and K. Kawasaki. 1993. Reduced diameter and conduction velocity of myelinated fibers in the sciatic nerve of a neurofilament-deficient mutant quail. *Neurosci Lett.* 153:65-68.
- Salzer, J.L. 2003. Polarized domains of myelinated axons. *Neuron.* 40:297-318.
- Salzer, J.L., P.J. Brophy, and E. Peles. 2008. Molecular domains of myelinated axons in the peripheral nervous system. *Glia.* 56:1532-1540.
- Sanchez, I., L. Hassinger, R.K. Sihag, D.W. Cleveland, P. Mohan, and R.A. Nixon. 2000. Local control of neurofilament accumulation during radial growth of myelinating axons in vivo: Selective role of site-specific phosphorylation. *J Cell Biol.* 151:1013 - 1024.
- Sanders, F.K., and D. Whitteridge. 1946. Conduction Velocity and Myelin Thickness in Regenerating Nerve Fibers. *J. Physiol.* 105:162-174.
- Saporta, A.S., S.L. Sottile, L.J. Miller, S.M. Feely, C.E. Siskind, and M.E. Shy. 2011. Charcot-Marie-Tooth disease subtypes and genetic testing strategies. *Ann Neurol.* 69:22-33.
- Saporta, M.A., I. Katona, R.A. Lewis, S. Masse, M.E. Shy, and J. Li. 2009. Shortened internodal length of dermal myelinated nerve fibres in Charcot-Marie-Tooth disease type 1A. *Brain.* 132:3263-3273.
- Schafer, D.P., A.W. Custer, P. Shrager, and M.N. Rasband. 2006. Early events in node of Ranvier formation during myelination and remyelination in the PNS. *Neuron Glia Biol.* 2:69-79.
- Sereda, M., I. Griffiths, A. Puhlhofer, H. Stewart, M.J. Rossner, F. Zimmerman, J.P. Magyar, A. Schneider, E. Hund, H.M. Meinck, U. Suter, and K.A. Nave. 1996. A transgenic rat model of Charcot-Marie-Tooth disease. *Neuron.* 16:1049-1060.
- Shaw, G., and K. Weber. 1982. Differential expression of neurofilament triplet proteins in brain development. *Nature.* 298:277-279.
- Shen, H., D.M. Barry, J.M. Dale, V.B. Garcia, N.A. Calcutt, and M.L. Garcia. 2011. Muscle pathology without severe nerve pathology in a new mouse model of Charcot-Marie-Tooth disease type 2E. *Human molecular genetics.* 20:2535 - 2548.
- Shen, H., D.M. Barry, and M.L. Garcia. 2010. Distal to proximal development of peripheral nerves requires the expression of neurofilament heavy. *Neuroscience.* 170:16-21.
- Sherman, D.L., and P.J. Brophy. 2005. Mechanisms of axon ensheathment and myelin growth. *Nat Rev Neurosci.* 6:683-690.

- Sherman, D.L., L.M. Wu, M. Grove, C.S. Gillespie, and P.J. Brophy. 2012. Drp2 and periaxin form Cajal bands with dystroglycan but have distinct roles in Schwann cell growth. *J Neurosci.* 32:9419-9428.
- Shin, J.S., K.W. Chung, S.Y. Cho, J. Yun, S.J. Hwang, S.H. Kang, E.M. Cho, S.M. Kim, and B.O. Choi. 2008. NEFL Pro22Arg mutation in Charcot-Marie-Tooth disease type 1. *J Hum Genet.* 53:936-940.
- Shy, M.E., and A. Patzko. 2011. Axonal Charcot-Marie-Tooth disease. *Current opinion in neurology.* 24:475-483.
- Simpson, A.H., T.H. Gillingwater, H. Anderson, D. Cottrell, D.L. Sherman, R.R. Ribchester, and P.J. Brophy. 2013. Effect of limb lengthening on internodal length and conduction velocity of peripheral nerve. *J Neurosci.* 33:4536-4539.
- Skre, H. 1974. Genetic and clinical aspects of Charcot-Marie-Tooth's disease. *Clin Genet.* 6:98-118.
- Smith, C.M., E. Cooksey, and I.D. Duncan. 2013. Myelin loss does not lead to axonal degeneration in a long-lived model of chronic demyelination. *J Neurosci.* 33:2718-2727.
- Soukup, T., G. Zachařová, and V. Smerdu. 2002. Fibre type composition of soleus and extensor digitorum longus muscles in normal female inbred Lewis rats. *Acta Histochemica.* 104:399-405.
- Sta, M., N.L. Cappaert, D. Ramekers, F. Baas, and W.J. Wadman. 2014. The functional and morphological characteristics of sciatic nerve degeneration and regeneration after crush injury in rats. *J Neurosci Methods.* 222:189-198.
- Stanley, J.L., R.J. Lincoln, T.A. Brown, L.M. McDonald, G.R. Dawson, and D.S. Reynolds. 2005. The mouse beam walking assay offers improved sensitivity over the mouse rotarod in determining motor coordination deficits induced by benzodiazepines. *J Psychopharmacol.* 19:221-227.
- Strack, S., R.S. Westphal, R.J. Colbran, F.F. Ebner, and B.E. Wadzinski. 1997. Protein serine/threonine phosphatase 1 and 2A associate with and dephosphorylate neurofilaments. *Brain Res Mol Brain Res.* 49:15-28.
- Szigeti, K., and J.R. Lupski. 2009. Charcot-Marie-Tooth disease. *Eur J Hum Genet.* 17:703-710.
- Tabo, E., J.H. Eisele, Jr., and E. Carstens. 1998. Force of limb withdrawals elicited by graded noxious heat compared with other behavioral measures of carrageenan-induced hyperalgesia and allodynia. *J Neurosci Methods.* 81:139-149.
- Taveggia, C., G. Zanazzi, A. Petrylak, H. Yano, J. Rosenbluth, S. Einheber, X. Xu, R.M. Esper, J.A. Loeb, P. Shrager, M.V. Chao, D.L. Falls, L. Role, and J.L. Salzer.

2005. Neuregulin-1 type III determines the ensheathment fate of axons. *Neuron*. 47:681-694.
- Taylor, M.D., R. Vancura, C.L. Patterson, J.M. Williams, J.T. Riekhof, and D.E. Wright. 2001. Postnatal regulation of limb proprioception by muscle-derived neurotrophin-3. *J Comp Neurol*. 432:244 - 258.
- Tooth, H.H. 1886. The peroneal type of progressive muscular atrophy.
- Tourtellotte, W.G., and J. Milbrandt. 1998. Sensory ataxia and muscle spindle agenesis in mice lacking the transcription factor Egr3. *Nat Genet*. 20:87-91.
- Vabnick, I., S.D. Novakovic, S.R. Levinson, M. Schachner, and P. Shrager. 1996. The clustering of axonal sodium channels during development of the peripheral nervous system. *J Neurosci*. 16:4914-4922.
- Vechio, J.D., L.I. Bruijn, Z. Xu, R.H. Brown, Jr., and D.W. Cleveland. 1996. Sequence variants in human neurofilament proteins: absence of linkage to familial amyotrophic lateral sclerosis. *Ann Neurol*. 40:603-610.
- Villalon, E., J.M. Dale, M. Jones, H. Shen, and M.L. Garcia. 2015. Exacerbation of Charcot-Marie-Tooth type 2E neuropathy following traumatic nerve injury. *Brain Res*. 1627:143-153.
- Vizoso, A.D. 1950. The relationship between internodal length and growth in human nerves. *J. Anat*. 84:342 - 353.
- Vizoso, A.D., and J.Z. Young. 1948. Internode length and fibre diameter in developing and regenerating nerves. *J. Anat*. 82:191-195.
- Vrinten, D.H., and F.F. Hamers. 2003. 'CatWalk' automated quantitative gait analysis as a novel method to assess mechanical allodynia in the rat; a comparison with von Frey testing. *Pain*. 102:203-209.
- W., B., and R.L. Friede. 1985. A new approach toward analyzing peripheral nerve fiber populations. II. Foreshortening of regenerated internodes corresponding to reduced sheath thickness. *J Neuropathol Exp Neurol*. 44:73 - 84.
- Waller, A. 1850. Experiments on the Section of the Glossopharyngeal and Hypoglossal Nerves of the Frog, and Observations of the Alterations Produced Thereby in the Structure of Their Primitive Fibres. *Phil. Trans. R. Soc. Lond. B*. 140:423-429.
- Waxman, S.G. 1980. Determinants of conduction velocity in myelinated nerve fibers. *Muscle Nerve*. 3:141-150.
- Waxman, S.G., and M.H. Brill. 1978. Conduction through demyelinated plaques in multiple sclerosis: computer simulations of facilitation by short internodes. *J. Neurol Neurosurg Psychiatry*. 41:408 - 416.

- Waxman, S.G., M.J. Craner, and J.A. Black. 2004. Na⁺ channel expression along axons in multiple sclerosis and its models. *Trends in pharmacological sciences*. 25:584-591.
- Webster, H. 1971. The geometry of the peripheral myelin sheaths during their formation and growth in rat sciatic nerves. *Journal of Cell Biology*. 48:348 - 367.
- Weimer, L.H., and D. Podwall. 2006. Medication-induced exacerbation of neuropathy in Charcot Marie Tooth disease. *J Neurol Sci*. 242:47-54.
- Weiss, P., and H.B. Hiscoe. 1948. Experiments on the mechanism of nerve growth. *Journal of Experimental Zoology*. 107:315 - 395.
- Wood, M.D., S.W. Kemp, C. Weber, G.H. Borschel, and T. Gordon. 2011. Outcome measures of peripheral nerve regeneration. *Annals of anatomy = Anatomischer Anzeiger : official organ of the Anatomische Gesellschaft*. 193:321-333.
- Woodruff, R.H., and R.J. Franklin. 1999. Demyelination and remyelination of the caudal cerebellar peduncle of adult rats following stereotaxic injections of lysolecithin, ethidium bromide, and complement/anti-galactocerebroside: a comparative study. *Glia*. 25:216-228.
- Wu, L.M., A. Williams, A. Delaney, D.L. Sherman, and P.J. Brophy. 2012. Increasing internodal distance in myelinated nerves accelerates nerve conduction to a flat maximum. *Current biology : CB*. 22:1957-1961.
- Xu, Z., J.R. Marszalek, M.K. Lee, P.C. Wong, J. Folmer, T.O. Crawford, S.T. Hsieh, J.W. Griffin, and D.W. Cleveland. 1996. Subunit composition of neurofilaments specifies axonal diameter. *J. Cell Biology*. 133:1061-1069.
- Yagihashi, S., S. Yamagishi, and R. Wada. 2007. Pathology and pathogenetic mechanisms of diabetic neuropathy: correlation with clinical signs and symptoms. *Diabetes Res Clin Pract*. 77 Suppl 1:S184-189.
- Yamasaki, H., C. Itakura, and M. Mizutani. 1991a. Hereditary hypotrophic axonopathy with neurofilament deficiency in a mutant strain of the Japanese quail. *Acta Neuropathol*. 82:427-434.
- Yamasaki, H., C. Itakura, and M. Mizutani. 1991b. Hereditary hypotrophic axonopathy with neurofilament deficiency in a mutant strain of the Japanese quail. *Acta Neuropathol*. 82:427-434.
- Yanagawa, Y., T. Kobayashi, M. Ohnishi, T. Kobayashi, S. Tamura, T. Tsuzuki, M. Sanbo, T. Yagi, F. Tashiro, and J. Miyazaki. 1999. Enrichment and efficient screening of ES cells containing a targeted mutation: the use of DT-A gene with the polyadenylation signal as a negative selection maker. *Transgenic research*. 8:215-221.

- Yeomans, D.C., V. Pirec, and H.K. Proudfit. 1996. Nociceptive responses to high and low rates of noxious cutaneous heating are mediated by different nociceptors in the rat: behavioral evidence. *Pain*. 68:133-140.
- Yeomans, D.C., and H.K. Proudfit. 1996. Nociceptive responses to high and low rates of noxious cutaneous heating are mediated by different nociceptors in the rat: electrophysiological evidence. *Pain*. 68:141-150.
- Yin, X., T.O. Crawford, J.W. Griffin, P. Tu, V.M. Lee, C. Li, J. Roder, and B.D. Trapp. 1998. Myelin-associated glycoprotein is a myelin signal that modulates the caliber of myelinated axons. *Journal of Neuroscience*. 18:1953-1962.
- Yoshihara, T., M. Yamamoto, N. Hattori, K. Misu, K. Mori, H. Koike, and G. Sobue. 2002. Identification of novel sequence variants in the neurofilament-light gene in a Japanese population: analysis of Charcot-Marie-Tooth disease patients and normal individuals. *J Peripher Nerv Syst*. 7:221-224.
- Yuan, A., M.V. Rao, T. Sasaki, Y. Chen, A. Kumar, Veeranna, R.K. Liem, J. Eyer, A.C. Peterson, J.P. Julien, and R.A. Nixon. 2006. Alpha-internexin is structurally and functionally associated with the neurofilament triplet proteins in the mature CNS. *J Neurosci*. 26:10006-10019.
- Yuan, A., T. Sasaki, A. Kumar, C.M. Peterhoff, M.V. Rao, R.K. Liem, J.P. Julien, and R.A. Nixon. 2012. Peripherin is a subunit of peripheral nerve neurofilaments: implications for differential vulnerability of CNS and peripheral nervous system axons. *J Neurosci*. 32:8501-8508.
- Yum, S.W., J. Zhang, K. Mo, J. Li, and S.S. Scherer. 2009. A novel recessive Nefl mutation causes a severe, early-onset axonal neuropathy. *Ann Neurol*. 66:759-770.
- Zhu, Q., S. Couillard-Despres, and J.P. Julien. 1997. Delayed maturation of regenerating myelinated axons in mouse lacking neurofilaments. *Exp Neurol*:299-316.
- Zhu, Q., M. Lindenbaum, F. Levavasseur, H. Jacomy, and J.P. Julien. 1998. Disruption of the NF-H gene increases axonal microtubule content and velocity of neurofilament transport: relief of axonopathy resulting from the toxin beta,beta'-iminodipropionitrile. *J Cell Biol*. 143:183-193.
- Züchner, S., M. Vorgerd, E. Sindern, and J.M. Schröder. 2004. The novel neurofilament light (NEFL) mutation Glu397Lys is associated with a clinically and morphologically heterogeneous type of Charcot-Marie-Tooth neuropathy. *Neuromuscular Disorders*. 14:147-157.

VITA

My name is Eric Villalón Landeros. I was born in June 23rd 1986 in the small community of about 800 people called, El Terrero, in the state of Guanajuato, Mexico. At the age of 5, I started my primary school education (elementary school) in the local school called Francisco I. Madero. In 1999, I graduated from Sixth grade and went on to obtain my secondary education (Junior High) in a nearby town public school called Escuela Secundaria Tecnica N_o 22 (technical secondary school). In 2001, I graduated from secondary school and after attending one semester at a preparatory school, my father decided to move my family and me to the U.S. to live with him. In February of 2002, I arrived to Santa Paula, Ca., and began attending the local high school. Since I did not speak any English I was enrolled in ESL classes. I adjusted and learned the language quickly. By the second semester I was enrolled in a beginners English class. I moved quickly through high school and in completed 10th, 11th and 12th grades in one semester each. In the spring of 2003, I graduated Santa Paula High School and continued my education at Ventura Community College.

I was the first member of my family to reach this level of education, as most of my family barely completed 6th grade. To some members of my family my decision to attend college came as a surprise, as I was told that college was for rich people only and that I was better off working on the fields to earn money. I am forever grateful for my parent's support and encouragement on my ambition for furthering my education.

At Ventura Community College, I continued to learn English, while taking lower division science classes in order to meet the requirements to transfer to a four-year university. While in community college, I participated in two summer research programs at the University of California, Santa Barbara, where I confirmed my interests in scientific research. In the summer of 2007, I transferred to the University of California, Davis, where I majored in Neurobiology, Physiology and Behavior (NPB) and minored in Latin. Adjusting to this school was difficult and as a consequence, I had to spend most of my time focusing on doing well in my classes during my first two years at UC Davis. During my third and last year at this school, I began volunteering at a plant biology laboratory, where I was exposed to molecular biology research in plants. In the spring semester of 2010, I graduated from UC Davis and seeking more in depth research exposure I applied to the University of Missouri-Columbia PREP program (MU PREP). I was accepted to the program and in the summer of 2010, I moved to Columbia, MO to begin my PREP program. The spring semester of 2011, I joined Dr. Garcia's lab where I spent the rest of my PREP program and continued to get experience in molecular and cellular neuroscience. In the fall of 2012, after completing the PREP program, I was accepted to the MU Biological Sciences graduate program, and was awarded an IMSD training grant and a Gus T. Ridgel fellowship. At the end of my second year in the program, I was awarded a T32 training grant position for my last two years. In the summer of 2016, I began my Postdoctoral training in Dr. Chris Lorson's lab.

This milestone in my career has made me the first member of my entire family, and the first person from my town in Mexico to reach this level of education. I am proud

of the work I have done and hope I can continue to inspire new scholars to further their education.

~ Cuando te toca, te toca. Cuando no te toca, ni aunque te pongas ~

(When it is for you, it will be yours regardless. When it is not for you, it won't be, even if you try hard for it)

- Dr. EViL.